Titre: Title:	Approaching Typical Metallic Conductivities in Polymer Nanocomposites for Lightning Strike Protection
Auteur: Author:	Xavier Cauchy
Date:	2018
Type:	Mémoire ou thèse / Dissertation or Thesis
Référence: Citation:	Cauchy, X. (2018). Approaching Typical Metallic Conductivities in Polymer Nanocomposites for Lightning Strike Protection [Thèse de doctorat, École Polytechnique de Montréal]. PolyPublie. https://publications.polymtl.ca/3308/

UNIVERSITÉ DE MONTRÉAL

APPROACHING TYPICAL METALLIC CONDUCTIVITIES IN POLYMER NANOCOMPOSITES FOR LIGHTNING STRIKE PROTECTION

XAVIER CAUCHY

DÉPARTEMENT DE GÉNIE MÉCANIQUE

ÉCOLE POLYTECHNIQUE DE MONTRÉAL

THÈSE PRÉSENTÉE EN VUE DE L'OBTENTION

DU DIPLÔME DE PHILOSOPHIAE DOCTOR

(GÉNIE MÉCANIQUE)

JUIN 2018

UNIVERSITÉ DE MONTRÉAL

ÉCOLE POLYTECHNIQUE DE MONTRÉAL

Cette thèse intitulée :

APPROACHING TYPICAL METALLIC CONDUCTIVITIES IN POLYMER NANOCOMPOSITES FOR LIGHTNING STRIKE PROTECTION

présentée par : CAUCHY Xavier

en vue de l'obtention du diplôme de : Philosophiae Doctor

a été dûment acceptée par le jury d'examen constitué de :

M. LÉVESQUE Martin, Ph. D., président

M. THERRIAULT Daniel, Ph. D., membre et directeur de recherche

Mme KLEMBERG-SAPIEHA Jolanta-Ewa, Ph. D., membre et codirectrice de recherche

M. TAVARES Jason R, Ph. D., membre

M. MARTEL Richard, Ph. D., membre externe

DEDICATION

To you, Reason.

À Caroline, pour un soutien indéfectible,

À Adrien et Edmond, pour leurs rires et sourires,

À ma mère, pour la rigueur et le goût du travail bien fait,

À mon père, pour l'amour du débat,

À mes amis, pour les évasions,

À ma fratrie, pour les défis.

ACKNOWLEDGEMENTS

I want to express my sincere gratitude to Prof. Daniel Therriault, my director, and prof. Jolanta-Ewa Klemberg-Sapieha, my co-director, for the priceless opportunity of pursuing a doctoral degree under their supervision. Their support and the discussions we had fueled me throughout this work.

Many thanks also to all industrial members of the project: Mario Simard from Bombardier Aerospace, Judith Roberge and Michel Dion from Bell Helicopter and Larry Hebert from 3M. Many thanks to the organizations themselves for their participation in the project.

Thanks also to all my friends and colleagues from the Laboratory for Multi-Scale Mechanics (LM^2) for the fruitful discussions and for the sheer joy of their companionship during these days of hard work: Anne-Marie Lanouette, Maxime Arguin, Nicolas Guérin, Renaud Passieux, Sampada Bodke, Rouhollah Farahani, Benjamin Le Dafniet, Qinghua Wu, Chao Xu, Kambiz Chizari.

A special thanks to Rajesh Ponnada, Hongqiu Wei and Martin Gagné for helping me with tasks related to the project.

Finally, I want to thank my friends and family for supporting me in times of need. A very special thanks to Caroline for her love and for yet another reason for lacking sleep: our two magnificent boys.

RÉSUMÉ

Parmi les objectifs de performance à atteindre lors de la conception d'un nouvel aéronef, la réduction de la masse de l'appareil est au premier rang, ladite masse ayant une influence directe sur les coûts variables de l'opération de l'aéronef. À cette fin, l'industrie a graduellement introduit les matériaux composites dans les composantes structurelles, desquelles le fuselage est peut-être la plus importante. La conversion du fuselage de l'aluminium aux matériaux composites n'est pas sans générer son lot de problèmes satellites. Notamment, la diminution de la conductivité électrique de la surface de l'appareil rend celui-ci vulnérable aux effets néfastes de la foudre.

En réaction à cette vulnérabilité, des grillages métalliques continus ont été ajoutés à la surface externe des panneaux composant le fuselage. Cet ajout augmentant considérablement la masse de l'ensemble sans contribuer à la rigidité, une demande pour des solutions alternatives fut créée.

L'ajout graduel de charges conductrices à une matrice isolante donne lieu à une augmentation subite de la conductivité du composite et à une transition de l'état isolant à celui de conducteur à une concentration donnée, appelée le seuil de percolation. La recherche sur les composites de nanotubes de carbone a permis de mettre en évidence un seuil de percolation extrêmement bas pour les particules de haut rapport d'aspect. En réaction, de multiples études se sont succédé qui cherchèrent à repousser les limites de la conductivité électrique de tels matériaux. Malheureusement, leur performance est limitée par une importante résistance de contact à l'interface entre les particules au sein du composite.

Pour qu'un composite ait une conductivité électrique assez élevée pour canaliser l'énergie de la foudre, les charges utilisées devront être caractérisées simultanément par une faible résistance de contact, par une haute conductivité intrinsèque et par une propension à former un réseau connecté dans la matrice.

Une stratégie répondant à ces exigences consiste à forcer la percolation d'un réseau de charges métalliques par leur auto-organisation dans le composite. Dans cette optique, nous avons exploré la combinaison d'une dispersion aqueuse de colloïdes d'époxy et d'un précurseur liquide de l'argent, aussi à base aqueuse. Lors de l'évaporation des solvants, de l'argent atomique précipite préférentiellement dans la phase aqueuse qui forme une topologie connectée dans le volume du matériau. La stratégie permet d'atteindre un seuil de percolation extrêmement bas à 0.27 vol.%, alors que les charges d'argent parviennent typiquement à la percolation à une valeur autour de 20

vol.%. La conductivité atteinte est de 5400 S/cm pour une concentration de 12.3 vol.%, seulement un ordre de grandeur plus bas que si tout le métal participait au réseau. Malheureusement, des problèmes d'adaptation de la méthode aux matériaux standards des fabricants ont motivé une réorientation des efforts de recherche.

La deuxième stratégie poursuivie consiste à combiner les qualités des charges métalliques et des particules carbonées à haut rapport d'aspect en une charge hybride cœur-coquille composée de nanofibres de carbone enduites d'argent. La méthode est une version modifiée du procédé de Tollens pour la fabrication de miroirs adaptée à la métallisation de nanoparticules en suspension. Les étapes de la fonctionnalisation, de la sensibilisation et de la métallisation ont fait l'objet d'optimisations individuelles et des conditions préférentielles ont été identifiées pour chaque étape. Une couverture uniforme de toutes les particules a été réalisée, et la conductivité spécifique de dépôts de particules a été mesurée à 1.8×10^3 S·cm^2/g, soit environ un ordre de grandeur sous celle de l'argent pur.

Les travaux ont ensuite visé à adapter la technologie aux procédés existants en incorporant les charges développées à la surface d'un panneau de composite carbone-époxy standard de l'industrie aérospatiale. Les particules furent d'abord dispersées dans un solvant aqueux, puis filtrées au travers d'une membrane poreuse dans un procédé inspiré des méthodes de fabrication de papier. Le « papier » résultant de cette opération fut ensuite laminé sur un film d'époxy « B-staged » avant d'être infusé et collé simultanément à la surface du panneau de carbone-époxy en utilisant une méthode analogue à l'infusion assistée par vide. La conductivité de la couche ainsi obtenue fut mesurée à 2.5×10^5 S/m. Cette valeur est analogue à celle des meilleurs adhésifs conducteurs à base d'argent, mais avec un taux de charge dix fois moindre. Les panneaux furent soumis à des tests d'émulation de la foudre correspondant à la limite supérieure des 35% des évènements les moins sévères avec succès.

Une solution complète de protection contre la foudre fut développée, de la synthèse de nanocharges sur mesure à l'inclusion de la solution à la surface de panneaux de carbone-époxy standards. Au-delà de l'application initiale, les nanocharges développées comportent des avantages potentiels pour des applications telles que les adhésifs conducteurs afin de minimiser le poids du produit, les coûts de matières premières ainsi que les performances en cyclage thermique. Le champ émergent

de la fabrication additive pourrait aussi bénéficier de la flexibilité accrue qu’apporte cette nouvelle solution.

ABSTRACT

Among all performance targets a new aircraft design seeks to achieve, reduction in weight is of primary importance since it has a direct influence on the energy costs. In pursuing this target, an increasing proportion of composite materials has been introduced into modern aircrafts' structures. Perhaps the most important structural component, the fuselage has not been spared by change. Every change requires adjustment, and thus the problem of lightning strikes to aircraft has resurfaced as the conductive aluminum skin was replaced by a lower conductivity carbon fiber/polymer composite counterpart.

Bonding a continuous metallic mesh to the surface of the skin has solved the problem, only to see the quest for mass minimization resume as this additional metal along with its adhesive and matrix contributes to the weight without benefits on the structural front. A better technology is sought.

Upon gradually incorporating conductive fillers in a non-conductive matrix, the material undergoes a sudden change from an insulator to a conductor at a concentration called the percolation threshold which differs for every matrix-filler combination and filler dispersion state. Research on carbon nanotubes composites has highlighted the ability of high aspect ratio fillers to reach percolation at a very low concentration. However, issues with contact resistance between individual particles inhibit the maximum performance such composites can historically reach.

If a polymer composite is to fulfill the requirements of lightning strike protection, the filler used should display simultaneously a high conductivity, a low contact resistance and a propensity to form connected networks through the matrix.

One strategy to obtain such a combination of properties is to force the percolation of metallic fillers through self-organization upon forming the composite. We explored such an avenue by combining an aqueous colloidal epoxy dispersion with a water-based silver precursor ink. Upon solvent evaporation, elemental silver precipitates preferentially in the continuous aqueous phase, effectively segregating the conductive phase in a connected topology and thus promoting the conductivity of the composite. A very low percolation threshold was achieved, at only 0.27 vol.%, whereas typical silver fillers percolation occurs around 20 vol. %. The conductivity achieved at 12.3 vol.% Ag is of 5400 S/cm, which is only one order of magnitude lower than if all silver participated fully to the network. Compatibility issues with the existing matrix systems however encouraged us to pursue another direction.

The second strategy investigated was to combine the qualities of metallic fillers and high aspect ratio carbonaceous particles in a hybrid core-shell silver-coated carbon nanofiber filler. We adapted the historical Tollens' process for mirror silvering to a suspension of carbon nanofibers through optimization of every step: functionalization, sensitization and silvering. Preferred bath compositions for both the sensitization and silvering steps were identified. The resulting bulk nanoparticles displayed a specific conductivity of 1.8×10^3 $S \cdot cm^2/g$, which is roughly one order of magnitude lower than that of pure silver.

We then proceeded to devise a method for the incorporation of the developed filler particles to standard aerospace carbon fiber reinforced epoxy panels. The particles were put into dispersion before being filtered through a porous membrane in a process inspired from the papermaking body of knowledge. The nanoparticles were then transferred to a standard B-staged epoxy film commonly used as a surfacing film for composite fuselage panels. Next, the particles film was simultaneously bonded and infused by vacuum-assisted resin infusion on the surface of standard aerospace carbon fiber-epoxy provided by our industrial partners. The conductive layer thus obtained displayed a 2.5×10^5 S/m value for conductivity, which is on par with class-leading silver-filled adhesives, but at a filler volume fraction a full order of magnitude lower. The panels were subjected to emulated lightning equivalent to the lesser 35% of the most severe lightning environment to which aircrafts are subjected with demonstrated protective effects.

A complete solution for lightning strike protection was developed, from the tailored synthesis of nanofillers to the inclusion in CFRP panels and lightning strike emulation. Apart from the initial targeted application for lightning strike protection, the developed nanoparticles have potential benefits for conductive adhesives in material costs, weight and thermal cycling resistance. The emerging field of additive manufacturing also stands to benefit from the added flexibility the technology developed provides.

TABLE OF CONTENTS

LIST OF TABLES

LIST OF FIGURES

LIST OF SYMBOLS AND ABBREVIATIONS

BMI ..... BisMaleImide

CNF ..... Carbon NanoFiber.

CNT ..... Carbon NanoTube.

CFRP ..... Carbon Fiber Reinforced Polymer.

E_c ..... Critical breakdown electric field

GO/rGO ..... Graphene Oxide/reduced Graphene Oxide

IPL ..... Intense Pulsed Light

ITO ..... Indium Tin Oxide

LSP ..... Lightning Strike Protection.

LWD ..... Long Way of the Diamond.

PAA ..... Poly(Acrylic Acid).

PEN ..... PolyEthylene Naphtalate

PMMA ..... Poly(Methyl MethAcrylate)

PSFS-SEC ..... Phase Selective Filler Synthesis Silver-Epoxy Composite.

PVDF ..... PolyVinyliDene Fluoride

PVP ..... PolyVinylPyrrolidone.

SEM ..... Scanning Electron Microscope.

SWD ..... Short Way of the Diamond.

TEM ..... Transmission Electron Microscope.

XPS ..... X-ray Photoelectron Spectroscopy.

LIST OF APPENDICES

CHAPTER 1 INTRODUCTION

Managing the immense energy conveyed by a lightning strike has always been a subject of concern for aircraft design. Although being struck by lightning is often seen as an unpredictable and very rare event, such is not the case with aircrafts as theory, experiments and available data point out that the very presence of a craft in the electric field generated in the vicinity of a thunderstorm creates a concentration of the field that initiates the electrical breakdown of the atmosphere and therefore initiates the lightning discharge [1, 2]. Accordingly, each commercial aircraft has a probability of being struck by lightning of approximately once every year [1].

In early wooden aircraft, the effects of lightning strikes were often catastrophic as the nonconductive materials used in the structure were unable to handle such large amounts of electrical energy. Catastrophic failures largely declined with the advent of metallic aircrafts [3] since current would flow freely through the fuselage. The problem has however resurfaced with the increasing utilization of polymer matrix composites in aircraft structures.

The industry had to palliate the low conductivity of polymer composites by resorting to metallic meshes that are bonded to the aircraft skin. This solution is a compromise: while adding conductivity, it also adds non-structural weight which impairs the strength to weight ratio that initially justified the added complexity of using composite materials. Moreover, these meshes add to the complexity of the manufacturing process and are difficult to repair. A better solution is sought.

Recent advances in micro and nanomaterials and microfabrication have paved the way for research efforts in tailoring the properties of composite materials to meet specific targets. Composites with self-healing abilities [4], enhanced out-of-plane properties [5], energy storage [6] and electrical conductivity [7]. Among these, the latter is of prime interest to the problem at hand. Electrical conductivity is imparted to polymeric composites by establishing a connected network of conductive fillers within the matrix. Carbon nanotubes are often the preferred nanofillers to accomplish this task [7]. However, the reader will be presented with other alternatives in Section 2.5 as potential replacement technologies for lightning strike protection (LSP) are discussed.

The proposed approach to this research was to investigate different fillers in resin systems compatible with aerospace requirements and to perform an initial assessment of the performance

upon which a filler would be chosen to investigate further. Optimisation work was then undertaken on this chosen research avenue. Next, the technology was adapted to aerospace standard carbon fibre reinforced polymer (CFRP) to provide a conductive coating, and the technology was tested in an emulated lightning environment. The research took place within the CRIAQ framework in a multi-disciplinary partnership with McGill University, UQAM and École Polytechnique de Montréal. The industrial partners were Bombardier Aerospace, Bell Helicopter Textron and 3M. The research avenues of the different teams were: graphene and its composites (UQAM), cold spray coatings (McGill), conductive nanocomposites (École Polytechnique de Montréal) and lightning emulation and materials testing (École Polytechnique de Montréal). This research fulfils the “conductive nanocomposites" part of the project.

Before a solution could be put to test through lightning strike emulation, initial assessment of the different solutions had to be performed. Therefore, although the performance of a solution is multi-factorial, a key measurable quantity had to be identified. We chose to examine the specific conductivity of the material as the main figure of merit as it expresses the ability of a material to transport charges per unit mass, two competing issues fundamental to the problem at hand.

The thesis is organized around articles submitted or published in peer-reviewed literature. The articles are presented in a logical order: the first paper in Chapter 4 presents early efforts to develop a coating with conductive fillers synthesised in-situ in a segregated, forced percolation network. The technology yielded excellent specific conductivity values but was not pursued because of manufacturing-related issues. The work was nonetheless published in peer-reviewed conference proceedings and is presented herein. It is our opinion that more work on this technology might be of value.

Following the early efforts, the focus of the research shifted to hybrid nanoparticles. The steps to achieve the hybrid silver coating-carbon core high aspect ratio nanofillers were investigated in-depth and reported in terms of the specific conductivity in the second article, published in a ACS Applied Materials and Interfaces, which the reader will find in Chapter 5.

Following the development of the nanofillers, the research energy shifted to the application of the technology for lightning strike protection of aircrafts. The third article presents the developed solution for the incorporation of the technology in CFRP panels in a robust manner, and with methods compatible with the existing materials and processes. Emulated lightning strikes were

performed on the panels produced and the results are reported. The paper, presented in Chapter 6, is currently under evaluation by a peer-reviewed journal.

CHAPTER 2 CRITICAL LITERATURE REVIEW

This chapter describes the current state of knowledge concerning the phenomenon of lightning strikes to aircrafts. The first part is a review of the physical manifestations of lightning with emphasis on the particularities of aircraft-related incidents. The reader will find in the second part a description of current lightning strike protection systems along with a review of the research published both on new technologies for lightning strike protection systems and on potential technologies for future systems.

2.1 Lightning strikes to aircraft

A typical commercial plane will be subjected to a lightning strike once in every 1000 to 10,000 hours of flight [8] with an average around 3000 hours, or one strike pear service year [1]. Hence, preventing the detrimental effects of lightning on the structure and avionics of the aircraft is of primary importance for the users' safety. These effects are classified between direct, defined as those which are observed at the lightning attachment points, and indirect effects, mainly caused by the stray currents and voltages induced by the electromagnetic fields generated during a lightning strike [2]. Typically, indirect effects will affect the onboard electronics and direct effects will cause puncturing of radomes, and melting of metal skins [2]. Composite structures are more vulnerable to direct effects because of their lower conductivity: Delamination as well as blistering, resin evaporation, fiber shortening and ply lifting are examples of the direct effects of lightning on these materials [9-12]. Sections 2.1.1, 2.1.2 and 2.1.3 provide an overview of the chain of events, from the inception of the lightning channel to the effects of the strike.

2.1.1 Strike mechanism

Aircraft-related lightning events can be divided between two categories: aircraft-intercepted discharge and aircraft-initiated discharge [1, 2, 13]. Figure 2.1 shows both mechanisms: In the upper half, an aircraft happens to be in the vicinity of a developing lightning channel. The second half shows a lightning channel developing from the aircraft itself and propagating in opposite directions. It has been shown in the 1980's that the latter accounts for about 90% of total strikes, [1, 2] which explains the surprisingly high frequency of lightning strike events. The widely accepted explanation for the initiation of the lightning channel by the very presence of the aircraft

is called the “bidirectional leader” theory [2]. This theory stipulates that the dielectric breakdown of gases surrounding the aircraft initially occurs at two points on the aircraft’s surface and subsequently propagates according to the ambient electric field direction.

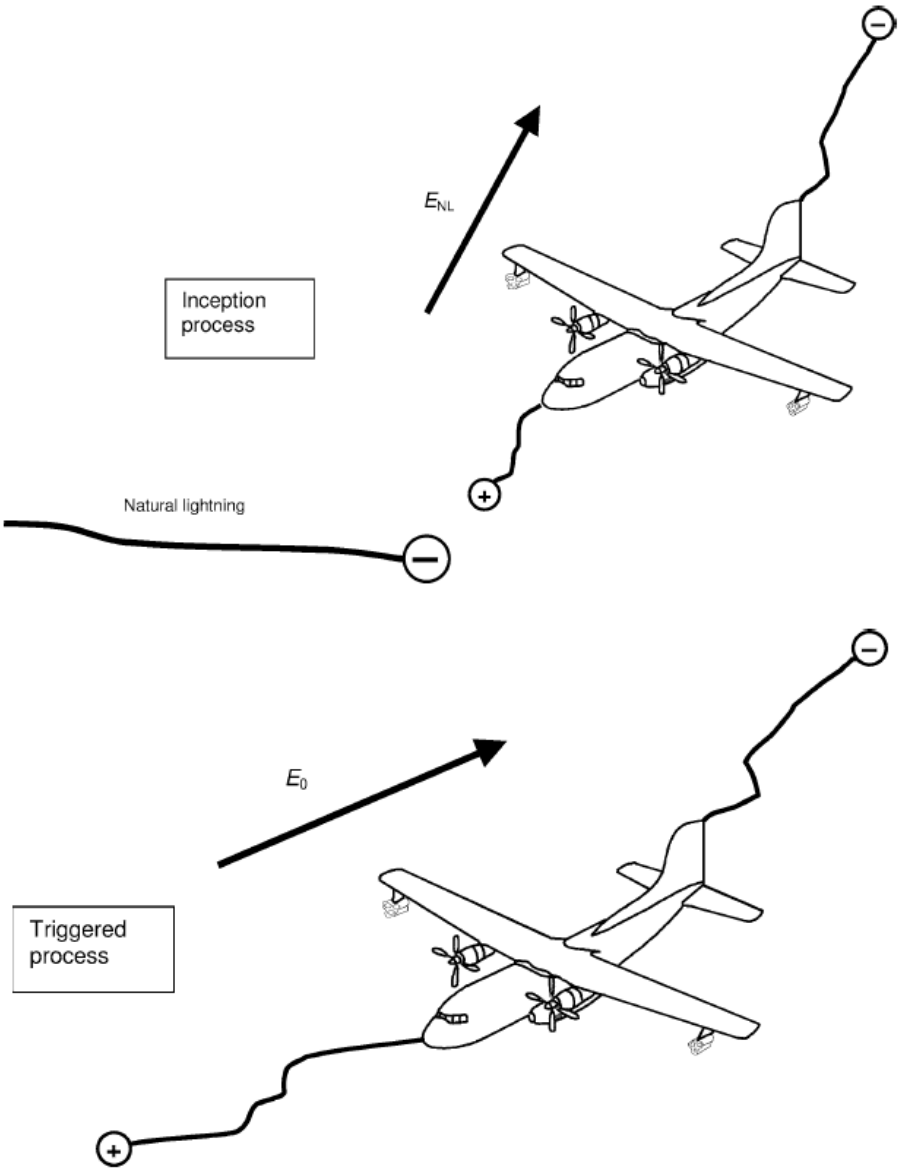

Figure 2.1: Intercepted (above) vs triggered (below) processes for lightning strike to aircraft. Also shown in the figure is the lightning propagation according to the bidirectional leader theory. Reproduced from [1]

While an ambient electric field of the order of 50 kV/m as measured at the time of a lightning discharge is insufficient for breakdown [2, 13], Petrov *et al.* showed that a local increase in electric

field arises from polarization effects in the aircraft body: The field inside a conductor is always null because any field will act on charges until they reorganize in such a way that the field is exactly canceled. In pointed objects, this translates to a very high charge concentration at the extremities which adds to the existing field outside the conductor. This effect is responsible for providing the extra field strength necessary for breakdown [13]. Consistent with this theory, sharp extremities such as the radome and wing tips are the most frequent lightning attachment points [14]. Figure 2.2 shows a lightning strike to an aircraft on takeoff. A careful observer will notice faint elongated structures besides the main lightning channel that seem to originate from the aircraft and dissolve into the air. These structures are in fact lightning strikes in development, called *secondary leaders*. Since the leaders are seen to be expanding from the aircraft in both directions, the image is a very strong confirmation of the bidirectional leader theory as an intercepted lightning strike would have shown a leader expanding away from the aircraft in a single direction. Here again, the leaders are seen originating from points of high curvature on the plane, namely the radome and the wingtip, thus further supporting the theory.

The current waveform as measured on airplanes consist of two phases: the initiation phase and the sweeping phase [15]. The lightning channels are developed during the initiation phase, with a steady current of tens to hundreds of amperes (A) [2, 15]. Bursts of current that reach tens of kA are superimposed on the continuous component. The whole initiation phase takes place in a few milliseconds while bursts exhibit a duration of the order of the μs [2]. The time between bursts ranges from microseconds to milliseconds [2, 15].

Figure 2.2: Aircraft-initiated lightning strike on takeoff. Leaders expanding away from plane can be clearly seen [16]

The sweeping phase owes its name to the lightning channel sweeping the aircraft's surface. While lightning channels are stationary on the event timescale and in the frame of reference of the earth, in frame of reference of the aircraft they are not [17]. Figure 2.3 illustrates the sweeping process in the aircraft reference frame. The ionized lightning channel suffers shear in the air flow boundary layer. Far from the aircraft's surface the flow speed is V_{inf}, equal to the relative speed of the plane to the viscous media, while immediately on the surface the relative flow speed is 0. The plasma channel thus undergoes stretching. Combining this effect with the natural fluctuation of the plasma leader around its path causes certain points in the channel to approach the plane's surface. When

the electric field between a point in the lightning channel and the aircraft's surface reaches the critical breakdown value (E_c), a new channel is formed that is attached to a new, rearward position on the aircraft [1, 18]. Current intensity and duration are more important during the sweeping phase with bursts reaching a few tens of kA over a constant component of tens of A [2, 15]. The bursts are called *return strokes* and occur when the lightning channel closes the circuit between charged regions.

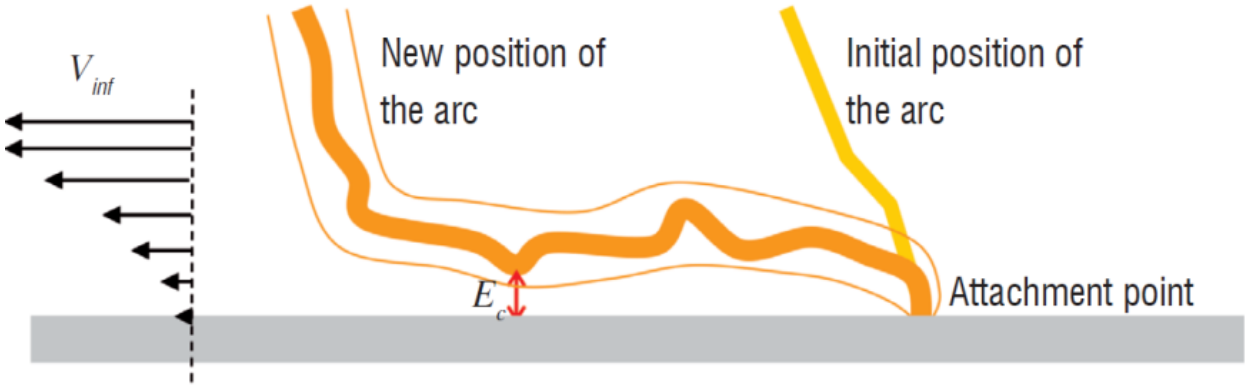

Figure 2.3: Illustration of the lightning channel reattachment process. E_c is the critical breakdown electric field and V_{inf} is the relative speed of the plane to the viscous media [18]

Figure 2.4 represents a typical case of lightning strike to aircraft. The intensity is scalable to represent more severe cases. The initiation phase can be seen with sharp bursts of current, followed by the sweeping phase with intense pulses of current. These pulses can occur even after the constant current component has extinguished.

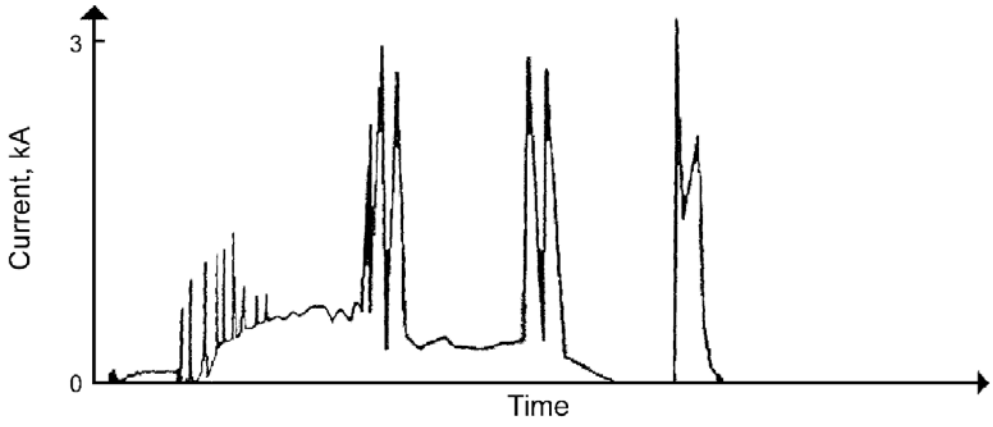

Figure 2.4: Schematic of a natural current waveform during a lightning strike [2]

The aircraft-related data presented in the literature mainly originates from intra-cloud flashes which occur between regions of different polarity within the same cloud. While being more frequent, these flashes are less severe than cloud-to-ground flashes. The peak current as measured at ground level during cloud to ground strikes is presented in Table 2.1 [19] along with the integral of the current squared over time (action integral), which provides a measure of the energy dissipated in the struck medium.

Table 2.1: Peak currents and action integrals for cloud-to-ground flashes [19]

Flash type	Peak current, highest 50% threshold (kA)	Peak current, highest 5% threshold (kA)	Action integral, highest 5% threshold (A^2s)
Negative	30	80	5.5×10^5
Positive	35	250	1.5×10^7

A negative flash carries negative charge from the cloud to the ground while a positive one removes negative charge from the ground. Negative flashes account for 90% of cloud-to-ground flashes [19]. Although the occurrence of an aircraft being struck by a positive strike is scarce, they must be taken into considerations when designing protection systems.

2.1.2 Direct effects of lightning strikes on carbon composite structures

These effects directly arise from the attachment of lightning channels and subsequent propagation of the lightning current in the material. Many factors contribute to the overall damage resulting from a lightning strike [18]. Thermal effects include the heat flux from the lightning plasma channel as well as joule heating from the current propagation. Mechanical effects arise from the lightning channel explosion shockwave, from overpressure induced by magnetic forces acting on the plasma channel, from magnetic pressure arising from the current flowing in the structure and from stresses induced by the rapid thermal expansion of the material [18].

For carbon structures, another form of damage arises from the electrical breakdown of the insulating matrix between adjacent plies [18]. Figure 2.5 provides an image of the typical damage inflicted to unprotected carbon fiber reinforced plastic (CFRP) panels. The damage observed on unprotected panels includes fiber shortening and resin vaporization at the arc attachment point,

lifting of the ply on a strip shaped geometry in the direction of the fiber and resin blistering around the attachment point [10, 12].

Feraboli et al. [12] performed lightning strike emulations on both unnotched and filled-hole (a coupon with a hole filled by a metallic fastener) composite coupons. The electric arc attached to the fastener in the filled-hole samples. At a peak current level of 30 kA and higher, the fastener appears to have been hammered in the body of the specimen, supporting the idea that mechanical damage arises from the shockwave.

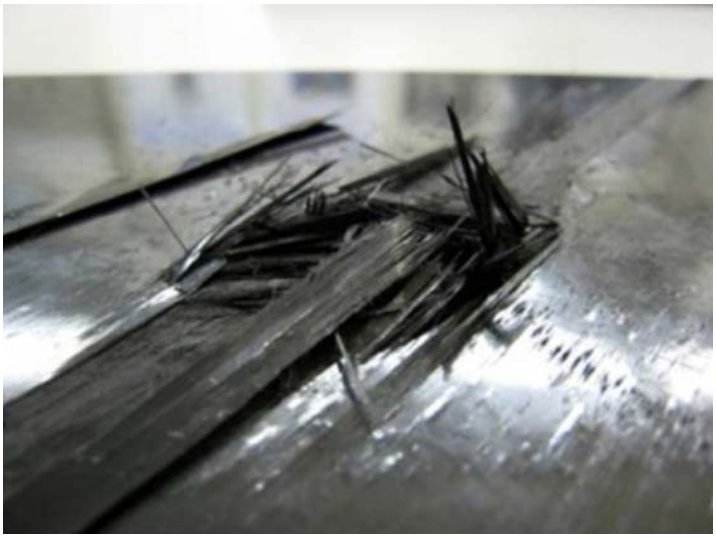

Figure 2.5: Typical lightning strike emulation damage to unprotected CFRP panel [10]. Fiber shortening is observed at the attachment point as well as lifted plies in the fiber direction. Resin blistering and swelling is also observed

Hirano et al. [10] noted a correlation between damage type and emulated lightning parameters, namely peak current, total charge transferred and action integral. Their findings reveal that peak current has more effect on fiber damage area and damage depth while transferred charge affects resin deterioration area. The action integral, on the other hand, is correlated to the delamination area.

2.1.3 Indirect effects of lightning strikes

Aircraft components that are not directly struck by lightning can also be affected by the event. The strong currents traveling in the aircraft's structure and the rapid change in current intensity generate strong magnetic fields, and more importantly, a sharp variation in the magnetic flux [3]. The

fuselage must therefore act as a faraday cage to prevent these intense flux variations from inducing currents in the aircraft's electronic system.

Moreover, the voltage drop across the path of the electric current may damage any circuit that is grounded or connected to the airframe. This effect, negligible on aluminum frames, is to be considered on their more resistive carbon composite counterparts [3]. The use of metallic meshes as LSP is sometimes insufficient to insure proper protection of sensitive equipment against lightning indirect effects [20].

Although the careful consideration of indirect effects is important in designing the aircraft, the scope of our work is to consider direct effects only as both problems require very different skillsets and design solutions.

2.2 Standards

The SAE International (formerly Society of Automotive Engineers) standardization organization has issued a series of standards regarding lightning strike protection. The standards are divided between lightning environment and waveform, aircraft lightning zoning and test methods. To preserve the concision and focus of the work, the details of the test methods will herein be omitted.

2.2.1 Aircraft lightning zoning [17]

Figure 2.6 gives an example of aircraft lightning zoning. The different zones described in the standard represent areas where a certain type of lightning current, with associated severity, is likely to occur. They are divided into 3 broad categories:

- Zone 1: Initiation, attachment and first return strokes are likely to occur.
- Zone 2: First return strokes unlikely to occur but following strokes highly probable. This is the area where the lightning channel is likely to reattach during swept strokes.
- Zone 3: Lightning attachment is unlikely to occur, but the current is likely to spread through this area.

Zones 1 and 2 are further divided into categories A and B. Category A represents zones where the lightning channel is unlikely to remain through the whole event (hang on). Zone B is likely to experiment hang on since swept leaders have nowhere else to go. Zone 1 has the additional category

C which is an extension of zone 1A where leader attachment is likely at altitudes where return strokes are less severe. Typically, extremities will be Zone 1 with forward positions being 1A and trailing edges 1B. The fuselage will be Zone 2B and the body of the wings Zone 3.

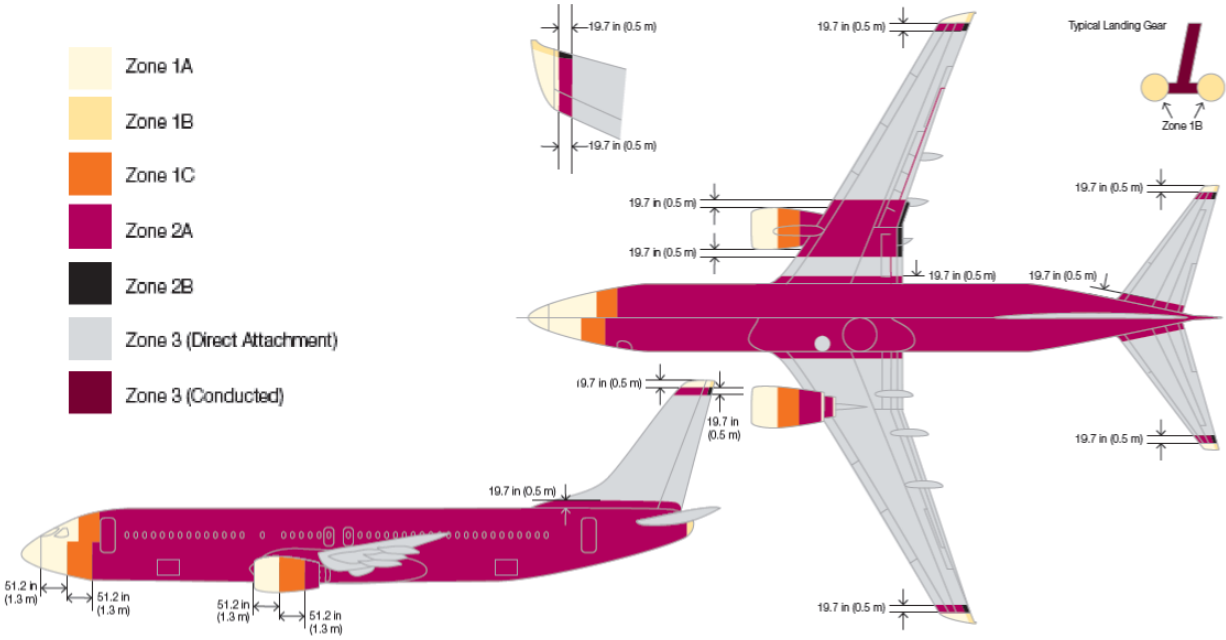

Figure 2.6: Lightning strike zoning per ARP5414 [17]. Adapted from [21]

2.2.2 Standardized waveforms and lightning environment [19]

The waveforms described in standard ARP5412 do not attempt to accurately reproduce naturally occurring lightning but rather aim at providing idealized waveforms displaying the key parameters of lightning flashes. Different current or voltage waveforms are prescribed for different test situations and for different zones of the aircraft. As an example, the current waveform for direct effect testing is depicted in Figure 2.7. Component A in Figure 2.7 is the most severe component of the strike phenomenon. It is attributable to the first return stroke and applies to Zone 1 where such an event is likely to occur. Components B and C represents intermediate current and continuous current following the first return stroke, respectively. Component D represent a subsequent return stroke of lesser amplitude. Zone 2 areas are required only to survive application of B, C and D components. Critical factors for component A are peak current and action integral of values 200 kA and 2×10^6 A^2s, respectively.

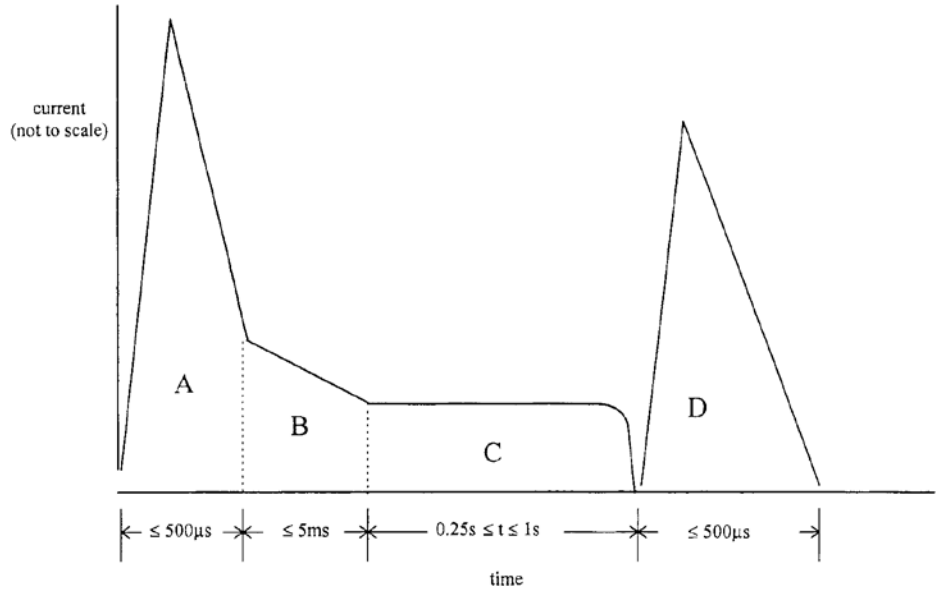

Figure 2.7: Standardized current test waveform per [19]. Component A represents the first return stroke and applies only to Zone 1 areas

2.3 Lightning strike protection technology

We provide an overview of existing technologies for LSP in section 2.3. For a quick lookup, the reader can refer to the summary of different LSP technologies' performances provided in Appendix A.

2.3.1 Metal meshes

The aerospace industry's common practice for protection of composite structures is the addition of a metallic mesh at the surface of the panel. The metals of choice are aluminum or copper, with respective conductivities of 3.77×10^7 and 5.96×10^7 S/m. While lighter than copper, aluminum has a high galvanic potential difference with graphite and therefore needs to be further isolated from the structure by adding a protective layer which adds weight to the aircraft [22]. Copper eliminates the threat of galvanic corrosion at the expense of adding weight. Metal meshes can be either woven or expanded.

Figure 2.8 illustrates the fabrication processes and parameters of expanded metal meshes. These meshes start as a metal foil that is slit with a dye in an alternating pattern (Figure 2.8a) and expanded to form diamond-shaped openings [22-24]. The extent of the expansion controls the size of the long way of the diamond (LWD) and short way of the diamond (SWD) measurements which will influence the conductivity in the two principal directions of the mesh.

Woven meshes are woven from metal strands in a simple plain weave. Woven meshes are subject to loosening of the strands which introduces additional contact resistance at the wire junctions. Also, the extra thickness at the wire intersections alter the surface finish [23, 24]. For integration on the composite surface, metal meshes are often sold integrated in a B-staged surfacing film and used against the tool surface as a prepreg in the composite layout (Figure 2.8d).

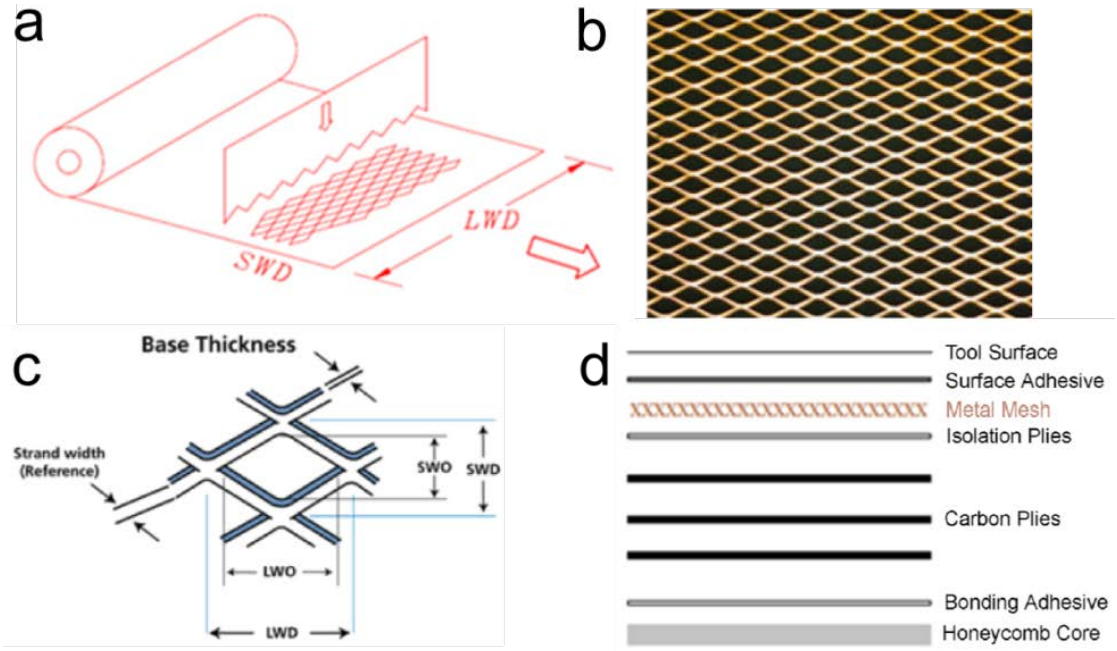

Figure 2.8: Expanded metal meshes. a) Fabrication method where a die cuts openings in a metal foil. The foil is then expanded in the direction indicated by the arrow [8]. b) Picture of an expanded copper mesh [25]. c) Fabrication parameters, SWD: short way of the diamond. LWD: long way of the diamond [25]. d) Typical stacking of layers on a composite panel [8]

Figure 2.9 shows the characteristics of prepreg systems incorporating metal meshes from two different manufacturers [26, 27]. Parameters of interest are the respective mass of the conductive mesh and of the resin, which lead to the calculation of the specific conductivity, defined as the sheet conductivity per unit mass. Typical sheet conductivities are of the order of 1×10^{-3} ohms per square (Ω/□), as calculated by taking the resistivity of an uniform metallic foil of areal weight equivalent to that of the mesh. The aluminum solutions provide a distinct advantage because of the much lower density of the metal, even when taking into account an additional 80 gsm insulation layer to protect the carbon plies against galvanic corrosion [26]. The solutions provided by Henkel on the other hand have a comparatively low amount of resin which helps in keeping the weight penalty low. It can also be argued that eliminating the need for a protective layer simplifies the manufacturing process and thus helps reduce costs.

The macroscopic interweaving of metallic and polymeric materials in metal meshes prepregs induce a localized mismatch between coefficients of thermal expansion, which in turn causes microcracking which can lead to corrosion of the mesh and a loss of conductivity. This effect was

shown to be more important with Al than with Cu, and the effect of the insulation fiberglass layer was also shown to be detrimental [28].

Repairs to the metal meshes can be problematic. Each lightning strike requires that the aircraft's skin be repaired. First, the damaged structural portion of the existing panel has to be removed and replaced according to state of art repair methods [29]. Damaged plies have to be fully cured before the actual LSP system repair, considered a separate operation [30], can start. The intact LSP system then must be exposed so that the patch can be carefully aligned and connected to the exposed strands. It is critical that the connectedness of the repaired metal mesh be verified with a milliohm meter [30]. When lightning strikes a poorly repaired panel, the damage observed is catastrophic, in some cases even worse than for unprotected panels [9].

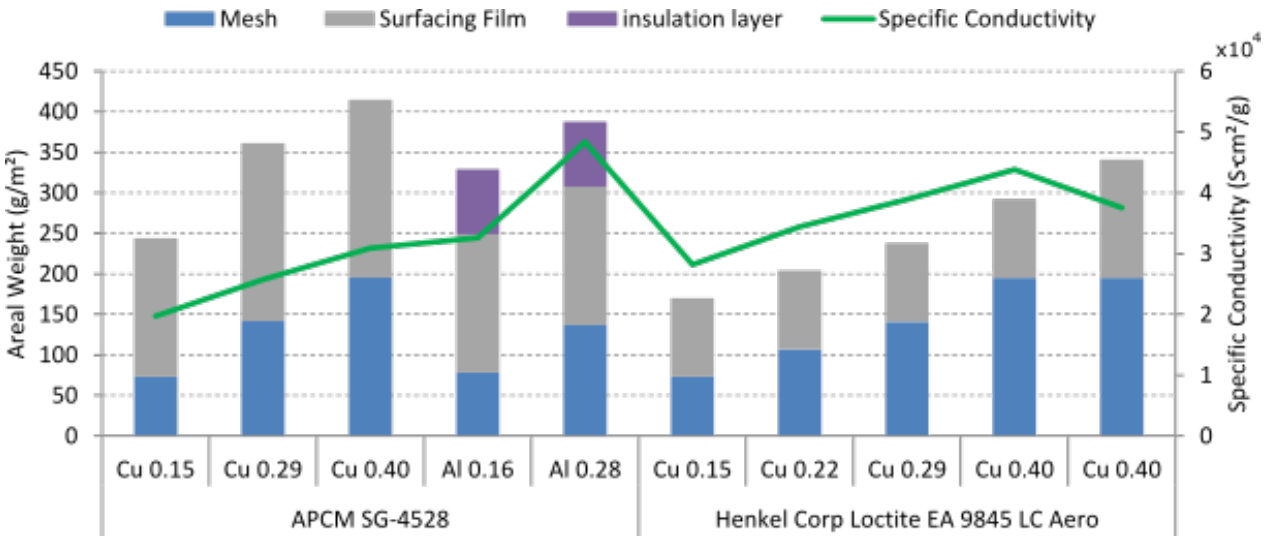

Figure 2.9: Areal weight of different commercial expanded metal mesh LSP prepregs along with the corresponding calculated specific conductivity [26, 27]

2.3.2 Alternative commercial solutions.

Hexcel commercializes an E-glass structural fabric that has been aluminized to provide sufficient conductivity for Zone 1 applications, according to the manufacturer [31]. The company lists a nominal resistivity of "5-10 Ω/ft^2" [*sic.*]. Considering the intention was to specify sheet resistance, the specific conductivity obtained is 6.94-3.47 S·cm^2/g with resin weight left out of the calculation.

Lord Corp. developed a product, available as spray-on coating or as a film, based on the segregation of metallic particles during curing [32]. The metallic fillers with dimensions in the range of a few

tens of microns are coated with a non-polar material whereas the matrix comprises polar moieties. Upon curing a kinetically driven process occurs in which the filler particles migrate and aggregate to form a conductive network. Silver flakes are the preferred filler particles for their ability to sinter at low temperatures and their high conductivity [32]. Although not mentioned in the text, it is reasonable to suppose that the elongated shape of silver flakes also contributes in establishing the conductive network. Considering data given in [33] and a matrix density of 1.2 g/cm^3, the calculated specific conductivity is ~9.1×10^3 S·cm^2/g.

Conductive Composites proposes CVD Ni coated carbon and aramid fibers as well as Ni nanostrands to enhance conductivity in composites, which they claim have been proven suitable for LSP [34]. Their proprietary process allows a continuous fabrication of the fabrics. The heaviest available fabric is also the most effective with a sheet resistivity of 0.015 Ω/□, for a specific conductivity of ~1×10^4 S·cm^2/g, albeit without factoring in the resin impregnation. An interesting fact about this technology is that it has potential to yield truly multifunctional systems as the conductive plies can be structural.

2.4 On the influence of layup on LSP performance

In aluminum fuselages, the bulk of the structural material participates in the conduction of lightning energy. Conversely, composite systems are made of different layers of material. This raises the question as to what stack up sequence should be promoted for LSP applications.

Recently, Han *et al.* [35] investigated the severity of the damage caused by emulated lightning strikes on composite coupons protected with carbon nanotube papers bonded to the underlying composite. Bonding was performed either with a conductive carbon nanotube loaded epoxy resin, a conventional insulating neat resin or a highly insulating boron nitride filled resin, respectively serving the roles of conductivity enhancer, conductivity benchmark and insulating barrier. The LSP system used is represented in Figure 2.10. The authors conclude that using an electrically insulating adhesive layer, although it does not allow conduction through the thickness and thus limits the volume were lightning energy is dissipated, yields better protection of the composite samples.

The effect of the dielectric barrier was further studied in numerical simulations by Fu *et al.* [36] who replicated the layup from the Han *et al.* paper, shown in Figure 2.10. They incorporated the electrical breakdown behavior of the adhesive layer in the ABAQUS simulation through user

subroutines. Their results are in excellent agreement with the conclusions from the Chinese group of Han *et al.* as they show that LSP systems incorporating a high dielectric strength layer between the conductive film and the substrate could withstand higher currents than their counterparts with conductive interlayers.

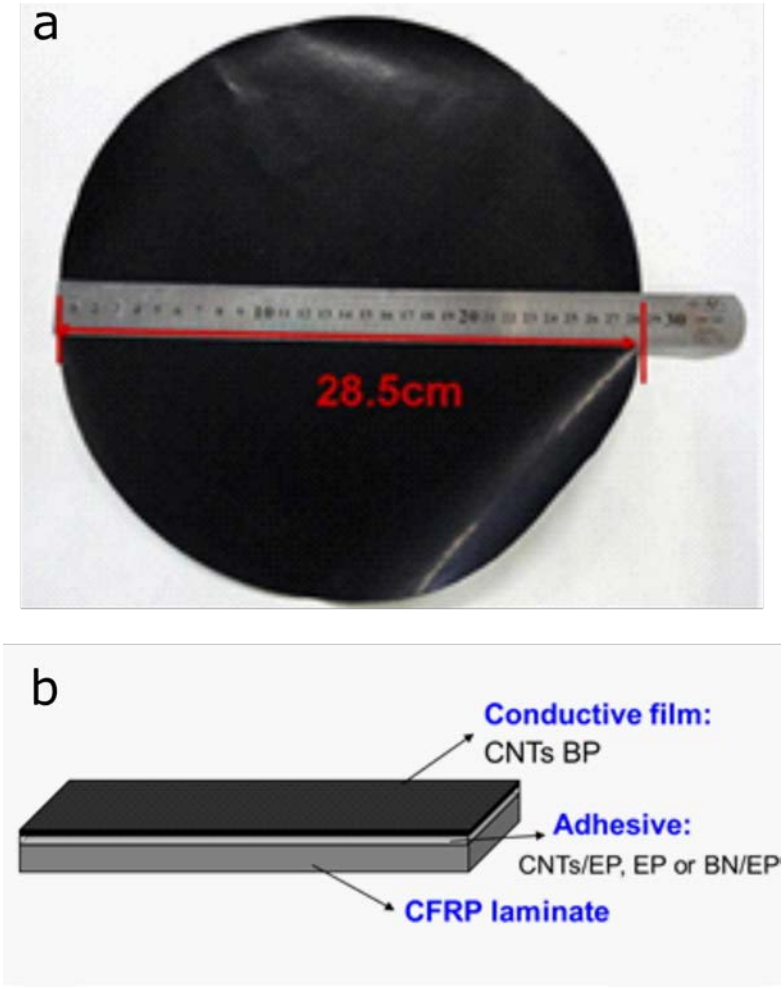

Figure 2.10: Disposition of the different layers in the prospective LSP system investigated by Han et al. a) As-produced buckypaper. b) Layer structure of LSP system. Reproduced from [35]

2.5 Potential materials for lightning strike protection

Metal meshes used for LSP are based on a 100 year-old technology for mesh fabrication that was introduced as a quick solution to a problem that was not fully recognized on the dawn of the composite era in aerospace [22]. The industry is thus awaiting new solutions that would minimize

the weight penalty associated with LSP solutions. Here are presented different avenues that hold potential for LSP applications.

2.5.1 Carbon nanotubes

Carbon nanotubes have perhaps been the center of attention of the most important body of materials science research of the early 21st century for their outstanding electrical and mechanical properties. One could not study conductive composites without taking a glance at what promises this technology holds.

2.5.1.1 Physics and morphology

In their simplest form, carbon nanotubes are rolled-up single sheets of honeycomb-structured sp^2 hybridized carbon atoms capped with fullerenes of typical diameter of 1-2 nm [37]. Figure 2.11 illustrates the honeycomb structure on a planar geometry. Nanotubes can exist in a multi-sheet configuration and are then called Multi-Walled Carbon Nanotubes (MWCNTs) as opposed to Single-Walled Carbon Nanotubes (SWCNTs). SWCNTs can have their honeycomb lattice wrapped in three different families of configurations: zigzag, armchair and chiral. The classification relies on the chiral vector of the nanotube. Figure 2.11 illustrates the basis lattice vectors and the construction of a chiral vector. The basis vectors of the graphene structure (honeycomb planar structure of C atoms) are a set of vectors (a_1, a_2) defined so that every position in the lattice can be reached with a translation by a vector $\vec{v} = m \cdot \overrightarrow{a_1} + n \cdot \overrightarrow{a_2}$. The chiral vector is defined as the translation around the circumference of the tube that brings back to the same lattice point by cylindrical symmetry.

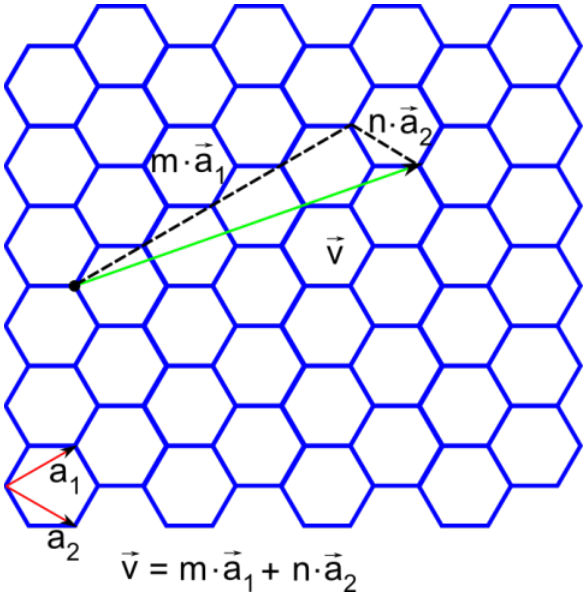

Figure 2.11: Basis vectors of graphene crystal structure. The chiral vector of a SWCNT is expressed as a linear combination of the basis vectors a_1 and a_2

Therefore, each chiral vector can be described by a pair of integers (n, m). Special cases of chirality are the zigzag and armchair configuration. For a zigzag nanotube $n = 0 \vee m = 0$. For the armchair configuration $n = m$. All other combinations are termed "chiral".

Chirality affects the electronic band structures in such a way that some configurations exhibit a band gap at the Fermi energy[1] and thus behave like a semiconductor [37, 38]. The condition for metallicity is simply expressed as [37]:

$$n - m = 3i, \tag{1}$$

where i is an integer. Consequently, approximately only 33% of SWNCT's are metallic. The linear dispersion relation of energy levels at the Fermi energy in graphene structure leads to null effective mass of electrons. The electrons are therefore relativistic particles and ballistic conduction can occur [39-41]. Theory then predicts exceptional electron mobility in carbon nanotubes. High SWCNT current densities up to 10^9 Acm^{-2} have been measured [42]. SWCNT have been

[1] The energy between the highest occupied and the lowest unoccupied levels considering electrons in their ground state.

theoretically calculated to have a resistivity per unit length as low as 4.2 kΩ/μm [43], which yields a conductivity of 1.35×10^6 S/cm, using an average tube diameter of 1.5 nm. The corresponding specific conductivity is therefore at least 5.9×10^5 S·cm^2/g, using the density of graphite.

MWCNTs usually exhibit a metallic behavior in their electrical properties as well as an increase in conductivity with temperature [44]. It was shown that multiple walls participate in current transfer [45] and that multiple channel ballistic conduction was feasible [46]. Stetter measured the resistance of individual multi-wall carbon nanotubes by scanning the potential values along the length of the tubes. This method allowed decoupling of the contribution of different shells to the overall resistivity. Values of the order of 10 kΩ/μm were consistently obtained [47]. Ebbesen *et al.* [48] measured the electrical conductivity on pristine isolated MWCNTs of different diameters. Their results[2] ranged between 2.5×10^2 and 2×10^5 S/cm with an observed current density of 6×10^6 A·cm^2. Care must however be taken with the interpretation of these results since prior to the measurements, the nanotubes were irradiated with 30 keV Ga ions which are known to damage and cut nanotubes [49].

2.5.1.2 Dispersion in solution

To control the distribution of nanotubes in a material, the dispersion of the particles must be achieved prior to the reorganization in the desired configuration. Dispersion of nanotubes into solution represents a challenge, with the only known efficient CNT dispersant being chlorosulfonic acid [50, 51], a hazardous superacid which protonates the surface of CNTs to induce electrostatic repulsion. The weak π–π interaction between adjacent carbon nanotubes coupled with the high aspect ratio of the particles increase the tendency of CNTs to bundle [52]. Chemical dispersion methods include covalent and non-covalent functionalization [53]. Covalent functionalization is obtained by attaching moieties to the tips or sidewalls of nanotubes. The covalent nature of the modification means implies that the functionalization is associated with a change of hybridization from sp^2 to sp^3 and therefore introduces defects in the electronic structure of the CNT [54].

Non-covalent functionalization can be achieved with polymers or surfactants. Polymers wrap around the nanotubes to form a molecular complex. The functional groups of the polymer then

[2] The authors assumed a hollow core of 2 *nm* radius.

become available for the dispersion of CNTs [54]. Surfactants adsorb on the CNT surface in a non-covalent way. The surfactants can encapsulate CNTs in a micelle entirely, create semi-spherical micelles on the surface or adsorb at random sites on the surface [52]. Non-covalent functionalization has the advantage of being non-destructive to the crystal structure. Chemical functionalization must be complemented with mechanical dispersion methods o provide the energy necessary for the initial separation of the tubes [52]. Among these, ultrasonication is the most widely used. It is accomplished by generating ultrasonic waves in the dispersion media through a vibrating tip or through the walls of a vessel. The short-wavelength shockwaves cause nanotubes on the bundle's periphery to dislodge and isolate [54]. Functional groups then prevent the nanotubes from rebundling by providing an electrochemical and physical barrier to the van der Walls close range interactions.

2.5.1.3 Buckypapers

A film of CNTs is called a buckypaper. These structures are often fabricated using vacuum filtration [55-62], a method in which nanotubes are dispersed into solution before being filtered through a microporous membrane. As the solvent is removed, individual CNTs settle in the plane of the filter media in a morphology analogous to that of random chopped fiber mats [59]. After drying, the film can be peeled off the filter. Table 2.2 lists different values for the electrical performance of buckypapers found in literature. The bulk conductivity of carbon nanotubes in buckypapers differs significantly from that of individual nanotubes with reported values ranging from 100 to 6200 S/cm [61, 63].

In their pristine state, buckypapers have poor electrical properties when compared to single CNTs. However, chemical treatments such as oxidation and doping [64] and chemical crosslinking [63] can improve their electrical performance. Remarkably, Chen *et al* reported a 10-fold improvement of buckypaper electrical properties upon HNO_3 treatment and cross-linking with 10,12-pentacosadiyn-1-OL (PCDO). Resistivity was further enhanced by aligning the nanotubes through stretching [63].

Park *et al.* [65] investigated the electromagnetic interference shielding properties of buckypaper laminated composites. Table 2.2 lists the resistivity of the different buckypapers investigated. The results from [63, 65] suggest that long MWCNTs exhibit better bulk conductivity than SWCNTs.

Furthermore, an anti-synergistic effect appears to arise from the mixing of SWCNTs and MWCNTs.

Tenent *et al.* [66] fabricated large area films of SWCNTs by a spray deposition technique. SWCNTs were dispersed in a carboxymethyl cellulose (CMC) solution which was then fed to an ultrasonic spraying nozzle. The dispersion was sprayed on a substrate and allowed to dry before soaking in 4M HNO_3 for removal of CMC. The films produced exhibited a specific conductivity of ~1.2×10^4 $S\cdot cm^2/g$, comparable to that of leading LSP solutions (see Table A.1 in Appendix A).

Han *et al.* whom we have discussed briefly in Section 2.4, tested a LSP system using a layup of CFRP/adhesive/buckypaper wherein the adhesive can be either neat epoxy, conductive CNT-filled epoxy or insulating boron nitride-filled epoxy. Their buckypaper is made by dispersion in water/triton X-100 and subsequent filtration through polyvinylidene fluoride membranes and intensive deionized water flushing to remove the adsorbed surfactant [67]. The surface conductivity of the protected composite coupons was reported to be of 0.83 S/□ for a volume conductivity of 57 S/cm, which lies in the low range of other buckypapers reported values (see Table 2.2). By using a ~200µm BN-filled insulating adhesive layer, the authors showed that simulated lightning strikes with peak currents up to 100 kA could be sustained by the test coupons. This is interesting since the specific conductivity obtained is of ~85 $S\cdot cm^2/g$, a rather modest value when compared to copper meshes that lie in the 10^4 $S\cdot cm^2/g$ range.

Table 2.2: Electrical performance of SWCNT and MWCNT buckypapers

Type	sheet resistance (S/□)	conductivity (S/cm)	thickness (µm)	areal weight g/m2	density (g/cm3)	specific conductivity ($S \cdot cm^2/g$)	Ref.
aligned SWCNTs		333	~10-20				[61]
random SWCNTs		143	~10-20				
random SWCNTs+MWCNTs		100	~25				
random MWCNTs		400	10-20	10-20	1	4×10^2	[63]
aligned MWCNTs		600	10-20	10-20	1	6×10^2	
HNO3 random MWCNTs		1600	10-20	10-20	1	1.6×10^3	
HNO3 aligned MWCNTs		2400	10-20	10-20	1	2.4×10^3	
PCDO x-linked random MWCNTs		2380	10-20	10-20	1	2.4×10^3	
PCDO x-linked aligned MWCNTs		6200	10-20	10-20	1	6.2×10^3	
SWCNTs		200	10-15	21,5	1,72	116	[65]
SWCNTS, large diameter MWCNTs		50	20-25	21,5	0,96	52	
SWCNTS, small diameter MWCNTs		50	20-25	21,5	0,96	52	
Long MWCNTs		400-1000	20-60	21,5	0,54	1.3×10^3	
Long MWCNTs SOCl2 doped		6000	20-25	21,5	0,96	6.3×10^3	
CMC-SWNT, removal of CMC with HNO3	0.01			0,01		1×10^4	[66]
	0.033			0,028		1.19×10^4	
	0.05			0,041		1.22×10^4	
Triton X-100 dispersed, vacuum filtered	0.83	57	70			85	[35]

2.5.1.4 Percolation in polymers

Gradually adding conductive particles to insulating polymers leads to a sudden increase in the electrical conductivity of the composite. The phenomenon is called *electrical percolation* and is

characterized by a *percolation threshold*, a concentration of fillers at which the percolation takes place. Conductivity around the percolation threshold takes the form [7]:

$$\sigma = \sigma_0 \cdot (\Phi - \Phi_c)^t, \quad (2)$$

where σ is the conductivity, σ_0 a proportionality constant, Φ is the concentration of fillers, t is the critical exponent and Φ_c is the percolation threshold. The percolation threshold is affected by the filler's aspect ratio [68], dispersion state in the polymer [7, 68] and particle alignment [69, 70]. Carbon nanotubes can yield very low percolation thresholds because of their very high aspect ratio. It was found that a good dispersion was desirable for a low percolation threshold [68], but a certain degree of re-aggregation of particles into a network can promote conductivity in the composite: a non-uniform distribution with a good dispersion is thus desirable [71, 72]. Alignment of nanotubes can promote percolation up to a certain point after which further alignment degrades the degree of percolation [69, 70]. Conductivities reached in percolated CNT-polymer composites range from 1×10^2 S/cm for 10 wt% $SOCl_2$ treated HIPco (High-Pressure Carbon monoxide) SWCNTs in polymethyl methacrylate (PMMA) matrix to 1×10^{-10} S/cm for 0.2 wt% HIPco SWCNTs in polybutylene terephthalate (PBT) matrix [7]. Conductivity values at percolation threshold are typically very low when compared to those of metallic conductors.

2.5.1.5 CNT fibers

Carbon nanotube fibers can be made by bundling CNTs along their axis and spinning them into a yarn. They are interesting as they provide very high contact area between individual nanotubes which can help in minimizing the contact resistance that plagues nanotubes networks. Li *et al* [73] fabricated fibers by collecting nanotubes directly from an aerogel on a rotating spindle. The maximum conductivity achieved is of 8.3×10^3 S/cm.

Another method for manufacturing CNT fibers consists in collecting nanotubes drawn from nanotube "forests" directly unto a spindle [74, 75]. Figure 2.12 illustrates the process of fiber drawing. Zhang *et al*. obtained a conductivity of 5×10^2 S/cm from MWCNTs [76] while Li *et al.* obtained 5.0×10^2, 6.4×10^2, 6.9×10^2, and 9.1×10^2 S/cm from pristine, annealed at 480 °C in air, HNO_3 treated and Au particles decorated samples respectively.

In 2013, Behabtu *et al.* from the Smalley group of Rice University successfully prepared nanotube fibers by wet-spinning from a 2-6 wt% CNT solution in chlorosulfonic acid [77]. The solution is extruded into a water or acetone coagulant and drawn onto a drum. The fibers exhibited a remarkable conductivity of 2.7×10^4 S/cm and doping with iodine yielded a maximum conductivity of 5.7×10^4 S/cm. Maximum specific conductivity was 4.1×10^4 $S\cdot cm^2/g$.

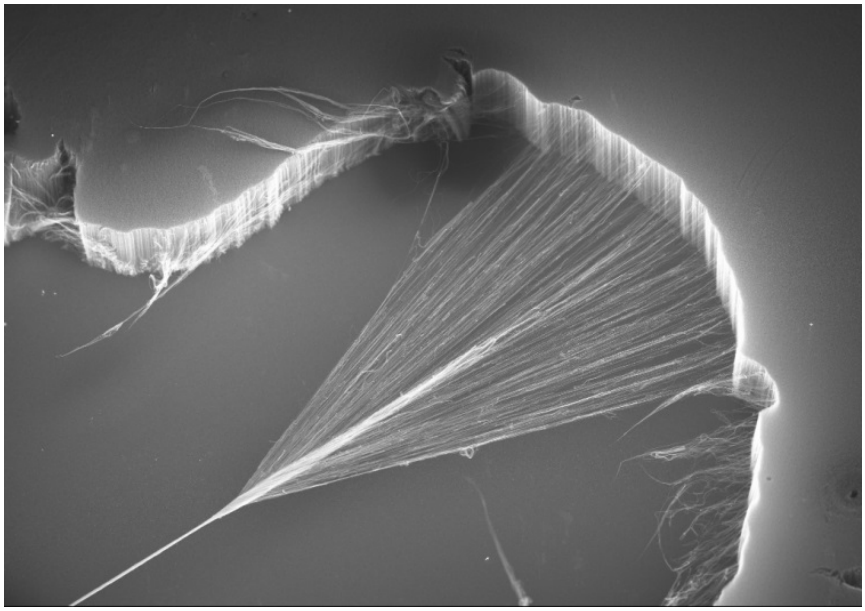

Figure 2.12: Fiber spinning from nanotubes "forest"[74]

2.5.2 Carbon nanofibers

Carbon nanofibers (CNFs) sit between CNTs and conventional carbon fibers with a diameter ranging from 50 to 200 nm and a length of 50-100 µm [72]. They can be found under different configurations, namely, bamboo shape, parallel, and stacked-cup [72]. Figure 2.13 is a high-resolution transmission electron microscope (HR-TEM) image of a CNF sidewall. The inset is a conceptualized representation of the stacked-cup structure observed in the TEM image. Pristine CNFs exhibit a tendency to bundle similar to that of CNTs. However, the canted nature of the graphitic planes suggests a considerably more reactive surface than the basal planes displayed by carbon nanotubes. Interestingly, Hung *et al*. [78] showed that acid functionalization of CNFs in concentrated HNO_3 and H_2SO_4 (1:3 volume ratio) yielded stable dispersions in aqueous media up to ~11 g/L.

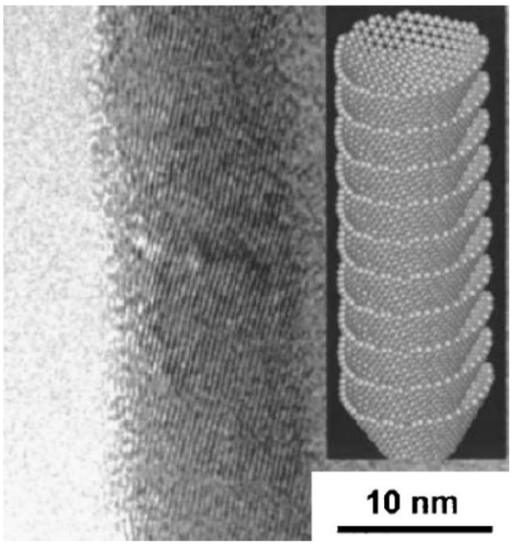

Figure 2.13: HR-TEM image of a CNF sidewall. The inset is a conceptualization of the stacked-cup structure [72]

A considerably smaller body of work is consecrated to CNFs composites than to their CNTs counterparts. Kuriger *et al.*[79] investigated the properties of polypropylene reinforced with vapor-grown nanofibers. Their investigation covered both nanofibers graphitized at 3000 °C and pyrolytically stripped nanofibers, the latter designed for enhanced compatibility with the matrix while the former targets the conductive properties. They compounded the composites with a twin-screw extruder designed to increased nanofibers alignment by inducing shear. They measured at a 23% volume fraction a 10 S/cm maximum conductivity on strand samples. Although these values

are low for high current applications, they did spark interest in electromagnetic interference (EMI) shielding applications. Al-Saleh *et al.* compared the effectiveness of CNTs, CNFs and carbon black as EMI shielding additives [80]. They showed that both percolation threshold and maximum conductivity of ABS/CNFs composites sat between those of their carbon black and CNTs counterparts. The maximum conductivity reached with CNFs was of 0.67 S/cm. The maximum conductivity of CNF/polymer composites is ultimately bounded by the intrinsic conductivity the filler itself. This value is given to be of 2×10^4 S/cm for graphitized vapor grown CNFs [81].

Surprisingly, no work could be found that directly addresses the electrical properties of carbon nanofiber mats. Gou *et al.* in their work on hybrid CNF-Ni nanostrands papers came upon a sample where Ni was rarefied and reported the conductivity of the sample to be of 8.62×10^{-3} S/□ and 5.7×10^{-2} S/□ for the uncompressed and compressed samples, respectively, which yields specific conductivities of 1.46 S·cm^2/g for the former and 9.67 S·cm^2/g for the latter [82]. The proportion of the transport properties attributable to the Ni nanostrands in this sample is however not clear.

2.5.3 Graphene

Two-dimensional crystals were deemed unstable and thus impossible to isolate by some of the most influent minds of the 20th century [83]. Nevertheless, their predictions were proven wrong when Novoselov and Geim first isolated and measured the electronic properties of graphene flakes [84]. This discovery sparked a gold rush in the scientific community with research papers on the topic exploding from ~ 200 in 2004 to more than 14000 in 2013 [85]. While there is evidence of ballistic conduction in graphene, the properties of single flakes remain far from reach in macroscopic applications. The method employed for isolating single graphene flakes (the “scotch tape” method) has a notoriously low yield, so different techniques have been employed to produce graphene in larger quantities. Among these, chemical oxidation by the Hummers’ method and its derivatives can produce large quantities of the material. By adding functional groups mainly under the form of hydroxyl and epoxy groups on the basal plane with carboxylic acids along the edges and defects [86] the graphitic planes exfoliate and become dispersible in water and various other solvents [86, 87]. Graphene under this form is commonly termed graphene oxide (GO). Unfortunately, the oxidation of the graphene flakes introduces defects in the electronic structure and graphene oxide is therefore an electrical insulator. Through a reduction process, it is possible to convert graphene oxide back to a near pristine graphene structure. Reduction can be performed chemically in solution

[88-90], thermally [89] or by exposition to electromagnetic radiation [91-93]. GO or reduced GO (rGO) can then be assembled into sheets by vacuum filtration [94], electrophoresis [95] and drop casting [96]. Once reduced, graphene oxide in a film-like structure recovers some of its conductivity, but struggles to meet the expectations with conductivities reaching at most ~3×10^2 S/cm [90]. Using the density provided by Dikin *et al* [94] for graphene oxide as a best case scenario (1.8 g/cm^3), one obtains a specific conductivity of 1.67×10^2 S·cm^2/g, which is still far below the values obtained with CNTs. Moreover, the most efficient reduction processes involved in restoring electrical conductivity involve immersion in hydroiodic acid or graphitizing in inert atmosphere at 1100 °C, which does not lend well to large scale industrial processes.

Inclusion into polymers necessarily hinders the electrical performance of the graphene electrical network. In this regard, the highest published value of conductivity is of 30 S/cm for a rGO/PVDF composite reduced with hydroiodic acid [97]. Unfortunately the authors do not provide the density of the composites even though they measured it. Since the PVDF used is 1.74 g/cm^3, we can reasonably expect the composite density to hover around 1.8 g/cm^3 for a specific conductivity of the composite of 16.7 S·cm^2/g.

These numbers show that while graphene and graphene oxide have good potential for LSP applications because of the intrinsic conductivity of graphene, the low density of carbon and the 2-dimensional nature of the nanoparticles, a lot of research remains to be done to enable the manufacturing of large-scale coatings retaining the electrical properties of graphene.

2.5.4 Metallic fillers

Metallic fillers exhibit high conductivity but at a high weight penalty. For example, silver has a conductivity of 6.3×10^6 S/cm and a density of 10.49 g/cm^3 while graphite has a density of 2.25 g/cm^3 but a conductivity of 7.27×10^2 S/cm [8]. As metal expanded meshes are perfectly connected, every bit of metal participates to the overall conductivity. However, as was shown in Figure 2.9, the amount of binder necessary to embed theses meshes add substantial weight. Therefore, for metallic particular fillers based LSP solutions to compete with readily-available metal meshes, one must be careful to control the dispersion and the connectivity of the particles in the composite while aiming for very high volume ratios of fillers.

A strategy for improving particle interconnectivity within the composite is to control the dispersion in such a way that particles segregate on a 2D geometry within the bulk polymer. Capozzi *et al*. [98] achieved highly segregated networks of conductive indium tin oxide (ITO) particles within a PMMA matrix by coating the PMMA powder with ITO nanoparticles (see Figure 2.14). The mix was subsequently molded by compression molding at 170 °C. Particles are shown to aggregate on a wireframe-like three-dimensional network on the vertices of the powder grains contact planes.

The commercial system marketed by Lord Corporation and discussed in section 2.3.2 incorporates metallic fillers in a system designed to efficiently control dispersion of the particles within the composite [32, 33]. It represents a good example of an efficient strategy for maximizing the efficiency of metallic fillers.

2.5.4.1 Contact resistance

When metallic particles are put together in an electrical circuit, contact resistance arises. Untereker *et al.* [99] have shown that compactions of metallic particles exhibit conductivities in the vicinity of 1% of that of the bulk solid, regardless of the particle type and particle size. The authors argue that the resistivity of compacted particles is dominated by contact resistance. Only silver particles did show higher conductivity: It was observed that the particles sintered under pressure and thus contact resistance was minimized [99]. The normalized value thus attained is however not reported.

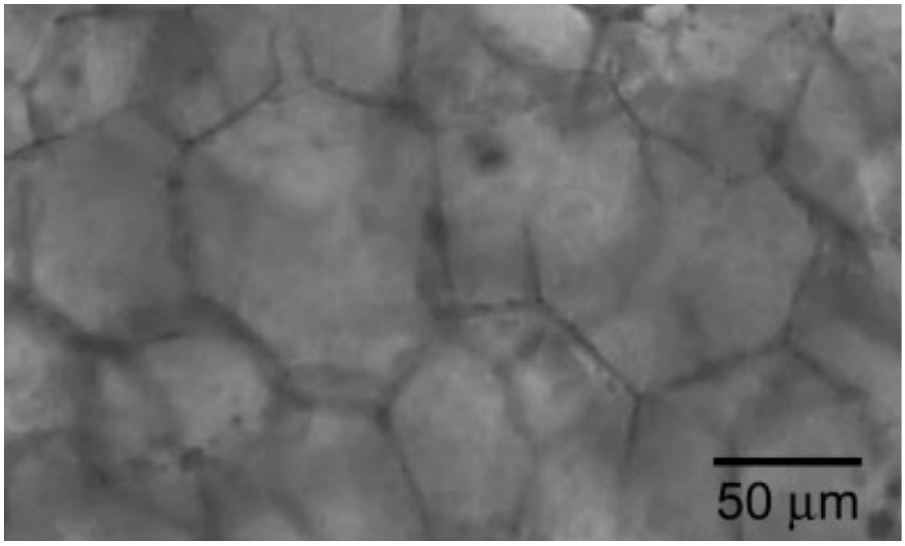

Figure 2.14: Optical micrograph of a 2.91 wt % ITO PMMA composite. Concentration of ITO at the grain edges appear as darker lines on the image [98]

2.5.4.2 Sintering

Sintering is a process in which particles are “welded” together without reaching the bulk melting temperature. The process is driven by the tendency of the system to minimize Gibbs’ free energy. This energy is described by:

$$\delta G_{sys} = \delta \int \gamma_S dA_S + \delta \int \gamma_{SS} dA_{SS} \qquad 3)$$

where γ_S is the unit surface energy and γ_{SS} is the unit interfacial energy [100]. With liquids, the interfacial stress relaxes instantly and the second term in 3333 vanishes. With solids, however, the system evolves until the variation in surface energy is balanced by the increase in interfacial energy. As there can be no evolution of the system without diffusion, the role of temperature in the sintering process is to provide sufficient mobility to the atoms of the particles to be sintered. Sintering of nanoparticles occurs at temperatures significantly lower than the melting temperature (T_m) of the bulk, e.g. around 200 °C for silver (T_m of 960 °C) [101-103]. This behavior is attributable to a significantly higher surface energy in nanoparticles and a lower melting temperature [104, 105].

For example, one of the important consolidation mechanisms in sintering is the movement of atoms by evaporation and condensation. The Kelvin equation for the vapour pressure reads:

$$p = p_0 \exp\left(\frac{\gamma V_M}{RT}\frac{2}{r}\right) \qquad (4)$$

Accordingly, atoms on a positive curvature tend to evaporate and condense into areas of negative curvature. This translates to movement of atoms from the surface of the particles into the neck formation region, as illustrated in Figure 2.15. When particles become very small, the radius in equation 4 tends to zero and the mechanism is accelerated accordingly.

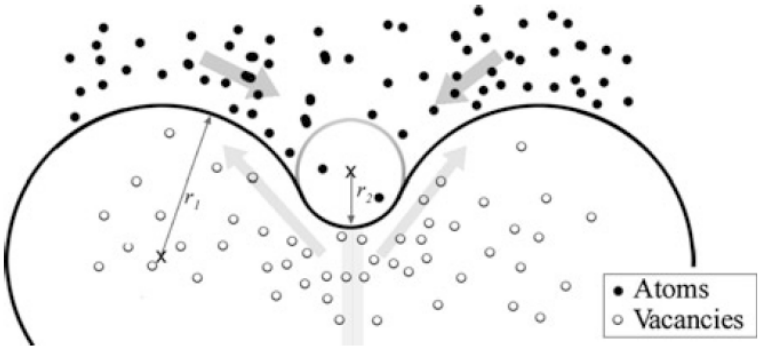

Figure 2.15: Migration of atoms through evaporation/condensation during sintering. Reproduced from [100]

Figure 2.16 shows the theoretical evolution of the melting temperature of copper nanoparticles with the particle size using values provided in [106]. Using the values provided in [107] and the theory outlined in [104] one can project the melting temperature curve for silver nanoparticles, also represented in Figure 2.16

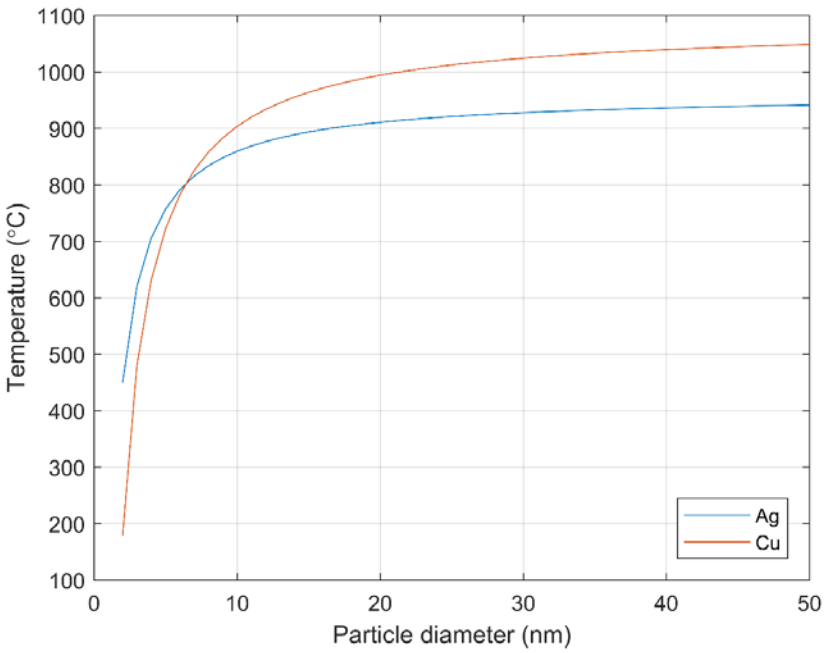

Figure 2.16: Melting temperature of Cu and Ag nanoparticles as a function of their diameter

At low temperatures, there is not sufficient energy for fusing the particles, the transport of matter through evaporation and condensation is negligible and the sintering mechanism is dominated by surface diffusion. The diffusion flux in classical sintering theory is given by:

$$j = \frac{2D}{\delta\Omega}\sinh\left(-\frac{\delta}{2kT}\nabla\mu\right) \simeq -\frac{D}{\Omega kT}\nabla\mu \tag{5}$$

Where D is the diffusion coefficient, δ and Ω are the atomic spacing and atomic volume, μ is the chemical potential and kT is the usual product of the Boltzmann constant and temperature. The chemical potential associated with the free surface reads:

$$\mu = -\Omega\gamma_s\kappa \tag{6}$$

where κ is the curvature of the free surface. Figure 2.17 shows the geometry of the surface of the particles during the sintering mechanism. The curvature can be described by:

$$\kappa_{(r=a)} = \frac{4R}{a^2} - \frac{1}{a} \tag{7}$$

Initially, the radius of the neck is very small and we can thus write:

$$\nabla\mu = \frac{\Delta\mu}{\Delta r} \simeq \frac{\mu_{r=a} - \mu_{r=0}}{a/2} = \frac{2\gamma_s(4R-a)\Omega}{a^3} \tag{8}$$

And we can rearrange to outline the *normalized half neck size*, a/R:

$$\nabla\mu = 2\gamma_s(4 - a/R)\frac{\Omega}{(a/R)^3}\frac{1}{R^2} \tag{9}$$

which is inversely proportional to the square of the particle radius. The driving force for surface diffusion in nanoparticles can therefore be very important and meaningful values of j in equation 5 can be attained at lower temperatures, thus triggering the sintering mechanism. A detailed discussion on the topic can be found in [100].

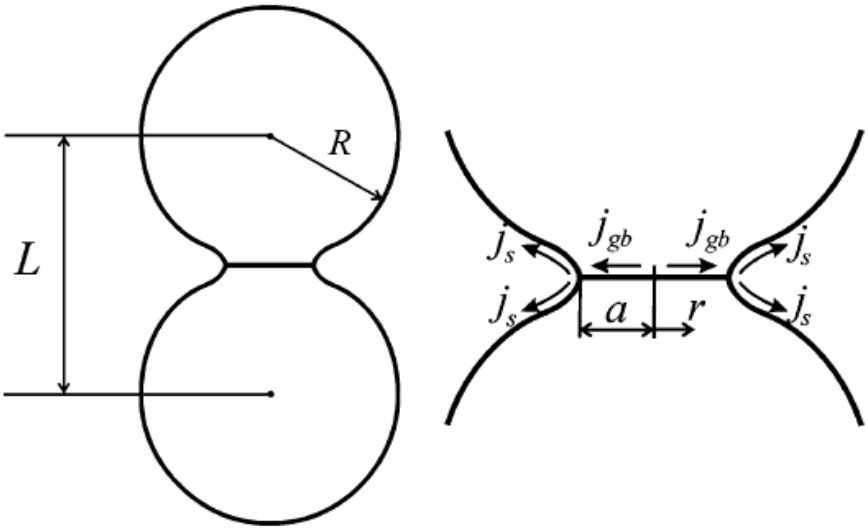

Figure 2.17: Neck formation at the junction of two particles

The low-temperature sintering behavior of metallic nanoparticles allows in-situ formation of conductive networks on heat-sensitive substrates. Perelaer *et al.* [108] achieved the sintering of ink-jet printed silver features on a polyethylene naphtalate (PEN) substrate using microwave energy. The change in the particle layer is illustrated in Figure 2.18. Although microwave energy is reflected from bulk conductors, it was shown that small particles absorb energy and can be heated locally [108, 109].

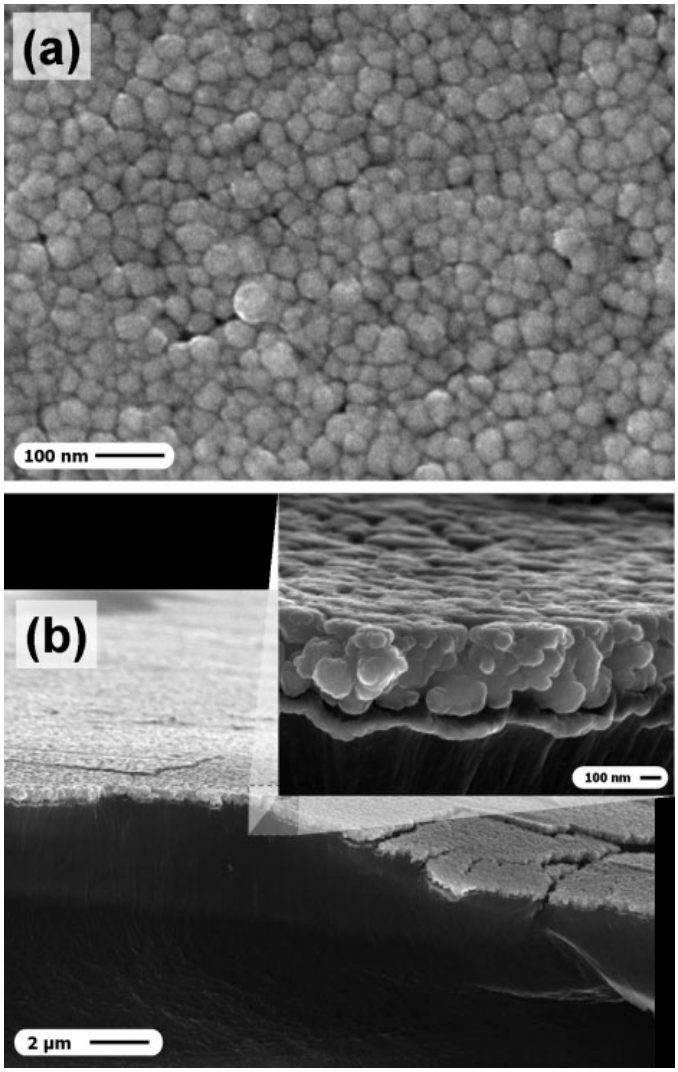

Figure 2.18: SEM micrography of silver nanoparticles sintering by microwave radiation. a) the unsintered particle layer before microwave irradiation. b) the resulting product after microwave radiation exposure. Reproduced from [108]

It has been shown that exposing CuO_2 coated Cu nanoparticles capped with polyvinylpyrrolidone (PVP) to intense pulsed light irradiation results in sintering of a copper network [106, 110]. It is thought that the copper oxide layer is reduced by chemical species resulting from the photodegradation of the PVP layer. Energy from the IPL pulse heats the copper particles and sintering occurs [110]. Garnett *et al.* achieved a similar result with silver nanowires exposed to 30 W/cm^2 broadband visible light [111]. The plasmonic excitations generate heat locally at the junctions between individual nanowires. This heat supply allows for “nano-welding” which is self

limiting as heat generation stops when a junction is achieved. The phenomenon is illustrated in Figure 2.19.

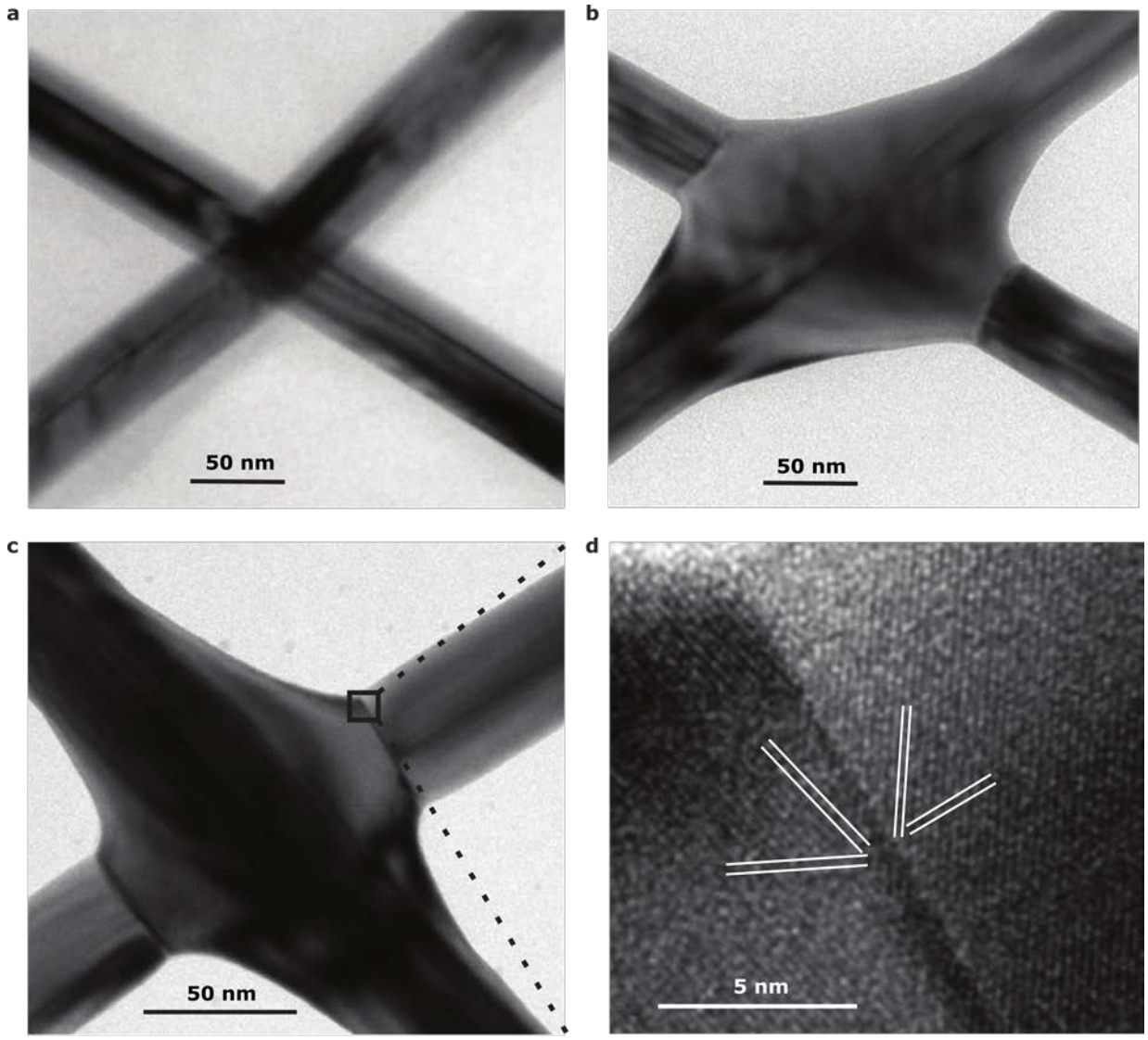

Figure 2.19: Plasmonic welding of Ag nanowires. a) TEM image of a nanowire junction prior to IPL exposition. b, c) TEM images of junctions after IPL exposition. d) High resolution TEM image of the junction depicted in c) outlining the change in crystal orientation at the junction. Reproduced from [111]

2.5.4.3 In-situ particle synthesis

As the dispersion and manipulation of conductive fillers proves to be one of the main challenges in functional nanocomposite fabrication, the in-situ synthesis of fillers might be of interest to the

community. Walker and Lewis [112] developed a particle-less silver ink with a viscosity comparable to that of water. Based on a modified Tollen's reaction, the ink reduces to elemental silver and silver acetate upon evaporation. Further heating to 90°C degrades silver acetate and yields pure silver. The authors used the very low viscosity particle-less ink to print patterns with ultra-fine nozzles of diameter 100 nm. The conductivity obtained with features annealed to 90°C revealed to be identical to that of bulk silver.

2.5.5 Hybrid fillers

Attempts have been made to take advantage of the carbon materials' lightness and of the metallic fillers' low contact resistance. Chakravarthi *et al.* realized Ni decoration of SWCNTs in an attempt to develop a new LSP technology [113]. The nanotubes were subjected to Ni electroless plating and dispersed using amine dispersants. The solution was sprayed unto standard carbon fiber plies and a bismaleimide (BMI) matrix was used.to infuse the hybrid mat. A decrease of 6 orders of magnitude in the sheet resistance was achieved in comparison with samples using pristine CNTs which the authors attribute in part to a better dispersion of the Ni-decorated nanotubes.

However, the surface resistance of samples with Ni-coated SWCNTs was of $2\text{-}4\times10^{2}$ Ω/□, which remains very far from the 1×10^{-3} Ω/□ typical target value for LSP. Wu *et al.* claimed to have achieved coating of MWCNTs with silver using Tollens' reaction [114]. Images of the pristine and treated CNTs they obtained are presented in Figure 2.20. Although the authors claim a uniform coating of the CNTs, the composites manufactured with the fillers only yielded an increase in conductivity of one order of magnitude. The TEM images that the authors produced to support the claim that the MWCNTs are uniformly coated are not sufficient proof in our opinion. An analysis of the image reveals that the mean diameter of the Ag-coated nanotubes as measured on 10 different areas is of 10.3 nm, far from the claimed 30 nm. The pristine nanotubes image is out of focus, and measurements made on what could reasonably be associated with a nanotube yield a mean diameter of 19.5 nm. This image therefore does not support the claims of the authors. The XRD patterns provided could very well be attributable to large Ag clusters synthesized as a reaction by-product

Using a different approach Gou *et al.* investigated the effect of the addition of Ni nanostrands to carbon nanofibers papers manufactured by a vacuum filtration process [82]. Their best sample yielded a conductivity of 3.4×10^{2} S/cm for a specific conductivity of 6.24×10^{2} S·cm^{2}/g. One of the samples yielded a much lower conductivity of 2.2 S/cm, which the authors attribute to a poor

distribution of the Ni nanostrands within the paper. Hence, a decrease of two orders of magnitude in the resistivity of the papers can be attributed to the presence of metallic nanostrands.

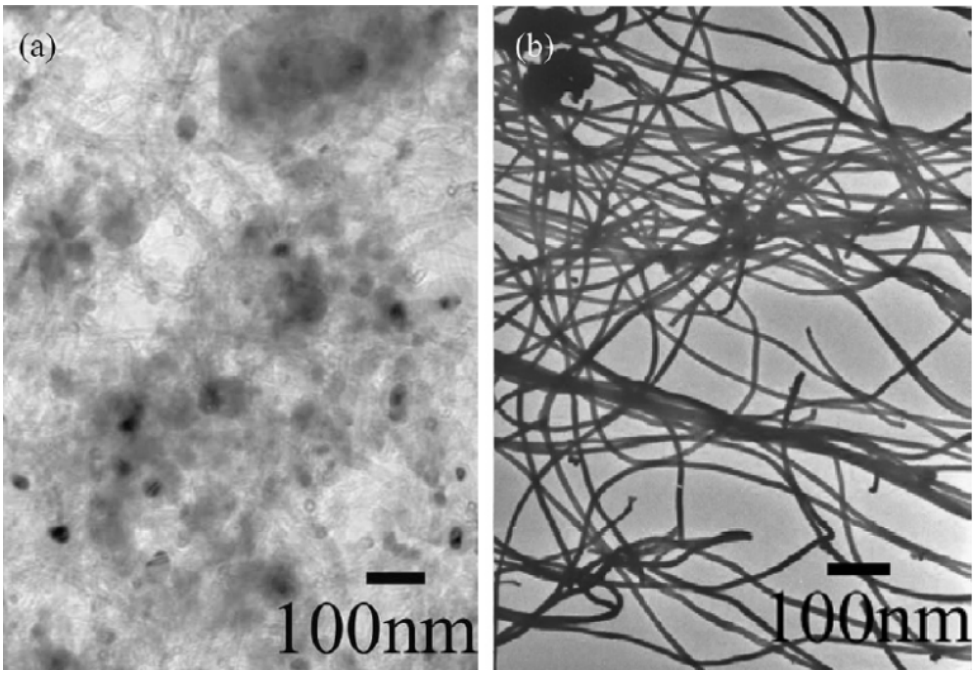

Figure 2.20: TEM images of a) pristine and b) silver coated CNTs obtained by Tollen's process. The poor focus in a) and the decrease in diameter after deposition do not allow to conclude that the MWCNTs are indeed uniformly coated with silver

2.5.6 Summary

Since lightning strikes to aircrafts are often initiated by the presence of the aircraft itself, they are much more common than they would have been if the interception of the lightning channel was the dominant mechanism. They are therefore a matter of primary importance.

The advent of composite materials in aerospace creates a new paradigm where the conductivity of the structural materials is not high enough to divert and transport the lightning energy away from the aircraft. So far, this problem has been addressed with metallic meshes bonded to the skin of the aircraft. This solution adds unwanted weight to the composite, diminishing its comparative advantage and complicates the manufacturing process. These hurdles proportionally diminish the economic incentive to use energy efficient materials in aircraft design.

We laid out seven distinct strategies for the design of a new LSP system which can be found summarized in Table 2.3. From this data, it appears that carbon nanotubes in the condensed form

(e.g. buckypapers, fibers) and hybrid fillers are the most promising candidates to achieve LSP in a new generation system.

These two strategies have a common characteristic: they both minimize the effect of the contact resistance between particles in the percolated network. Dense carbon nanotubes network multiply the contact points to dilute the contact resistance while intrinsic hybrid materials introduce a metallic element to ease conduction between particles.

According to this observation, an efficient strategy to develop a highly conductive polymeric composite should foremost target the contact resistance of fillers. Chapter 3 lays out the strategy that was chosen in this research to achieve this goal.

Table 2.3: Summary of prospective strategies for next generation LSP systems

Filler type	Material morphology	Maximum conductivity (S/cm)	Maximum specific conductivity ($S \cdot cm^2/g$)	Ref.
Carbon nanotubes	buckypapers	6.2×10^3	1.22×10^4	[63, 66]
	Percolated polymers	1×10^2	$\sim1\times10^{2*}$	[7]
	fibers	5.7×10^4	4.1×10^4	[77]
Carbon nanofibers	Percolated polymers	10	~11*	[79]
	buckypapers	2.22	9.67	[82]
graphene	buckypaper	3×10^2	1.67×10^2*	[90]
	Percolated polymer	30	16.7*	[115]
Metallic fillers	Chemically driven percolation, sintered	5×10^4	9.1×10^3*	[32, 33]
Hybrid fillers	intrinsic	-	1×10^4*	[34]
	mixed	3.41×10^2	6.24×10^2	[82]

*these values were approximated from density data of pure constituents.

CHAPTER 3 RESEARCH OBJECTIVES AND COHERENCE OF ARTICLES

3.1 Research objectives

The main objective of the work performed is to develop alternative materials for lightning strike protection of composites. More specifically, the research efforts described herein aim to improve the conductivity limits of nanocomposite materials by tailoring nanofillers specifically for this purpose and preparing samples through industry acceptable manufacturing methods. The findings that arise from this work will have implications, aside from LSP applications, in multifunctional applications of polymer nanocomposites. Highly conductive adhesives for heat sensitive electronics, 3-D printable electronics, conductive inks and pastes are a few examples of fields that might benefit from this research.

3.1.1 Specific objectives

I. **Identify and test different nanofiller/polymer combinations and assess their potential as components of next-generation LSP systems.** Review the existing literature to identify a strategy to promote a high electrical conductivity within polymeric nanocomposites. Identify three strategies. Prepare samples according to each strategy and measure their specific conductivity. Identify the most promising strategy.

II. **Study the identified material strategy. Perform optimization work.** Identify key parameters of the preparation of the identified nanofiller/resin combination. Investigate the effect of these parameters on the electrical performance of the nanocomposite. Improve the performance of the system

III. **Adapt the technology to be applied to CFRP panels. Subject the system to emulated lightning strikes.** Develop a method for the application of the technology on pre-existing CFRP panels. Adapt the technology to insure a uniform coating on flat panels and uniform dispersion of the nanofillers within the composite. Apply the developed coating to square CFRP panels of 30 cm side dimensions provided by the industrial partners. Investigate the effects of emulated lightning strikes on the panels.

3.2 Presentation of the articles and articulation within the research objectives

Chapter 4 is the result of early experimentation with various strategies, as identified in objective I. The paper entitled “Highly conductive heterogeneous epoxy-silver composites by phase selective in-situ filler synthesis” is a peer-reviewed conference proceedings paper which was published in the Proceedings of the *29th Annual Technical Conference of the American Society for Composites* (ISBN: 978-1-63439-415-4). The paper presents experimentation with in-situ synthesis of metallic fillers within the matrix and dynamically percolated by phase segregation. Mr. Cauchy designed and performed the experiments, performed characterization and analyzed the data. He also drafted the paper under the supervision of Prof. Therriault and Prof. Klemberg-Sapieha.

Chapter 5 lays out the work performed in relation to objective II. It presents the first journal article entitled “Synthesis of highly conductive, uniformly silver coated carbon nanofibers by electroless deposition.”. This paper was published in the journal *ACS Applied Materials and Interfaces* (DOI: 10.1021/acsami.7b06526). This journal was chosen for its strong chemistry component and its focus on interfacial phenomena. The journal also has a broad readership and a high impact on applications of fundamental research. It was therefore seen as an ideal media for our work. The paper provides in-depth information about the synthesis process of the filler identified through the exploratory work of objective I, a hybrid carbon-core silver coated high aspect ratio particle. It shows that it is possible to obtain a uniform silver coating on carbon nanofibers rather than discontinuous decoration. Doing so, it lays out the range of parameters for each step of the process, namely functionalization, sensitization and deposition, which result in a high quality coating on the nanofibers. The material obtained exhibits a specific conductivity roughly one order of magnitude lower than that of pure silver, which indicates that very efficient transport mechanisms take place within the material and at the particles junctions. Mr Cauchy designed all experiments and prepared all samples. All characterization was performed by Mr. Cauchy with the exception of XPS measurements and curve fitting which were realized by Josianne Lefebvre, research associate at the Engineering Physics department of École Polytechnique de Montréal. The paper was written by Mr Cauchy under the supervision of Prof. Therriault and Prof. Klemberg-Sapieha.

Chapter 6 presents the second journal article entitled “Hybrid Carbon-Silver Nanofillers for Composite Coatings with Near Metallic Electrical Conductivity” submitted to *Small* for the

multidisciplinary nature of the journal and its claimed focus on materials, science, engineering and chemistry at the nano- and microscale. The paper shows the work done in the scope of the third specific objective. It reports the inclusion of the nanofillers developed according to specific objective 2 into CFRP panels using standard aerospace CFRP panels and B-staged epoxy films. The material obtained exhibits a volume resistivity of 2.5×10^{3} S/cm at a record low loading of 6.3%, 10 times lower than the loading required to reach the same conductivity using conventional silver fillers. The measured specific conductivity was of 3.8×10^{3}, which is comparable to the performance of the commercial system proposed by Lord Corp. (see metallic filler, Table 2.3). A test panel was subjected to an emulated lightning strike and showed no damage compared to the control bare CFRP panel. All samples and all sample characterization experiments were realized by Mr.Cauchy. The lightning strike emulation was performed By Dr. Rajesh Ponnada in the laboratory of the department of electrical engineering of École Polytechnique de Montréal. The paper was written by Mr Cauchy under the supervision of Prof. Therriault and Prof. Klemberg-Sapieha and lightning strike emulation data was provided by Dr. Rajesh Ponnada

.

CHAPTER 4 ARTICLE 1: HIGHLY CONDUCTIVE HETEROGENEOUS EPOXY-SILVER COMPOSITES BY PHASE SELECTIVE IN-SITU FILLER SYNTHESIS

Xavier Cauchy, Jolanta-Ewa Klemberg-Sapieha and Daniel Therriault*

Laboratory for Multi-Scale Mechanics, École Polytechnique de Montréal, P.O. Box 6079, Station Downtown, Montreal (QC), H3C 3A7, Canada

Proceedings of the 29th Annual Technical Conference of the American Society for Composites 2014, May 2014.

4.1 Abstract

For the last decades, much effort was focused towards adding new functionalities to polymers and polymeric resin composite materials. In particular, the electrical conductivity of polymers is a matter of importance. For insulating polymers, current carrying capabilities are usually achieved by adding conductive fillers to the polymeric matrix.

The onset of the electrical conductivity happens at the percolation threshold, a statistical value for the critical filler loading that allows for a network formation. With metallic micro or nano-sized fillers, this threshold is typically high, as much as 25-30 vol.% for spherical particles. Lowering this threshold is desirable for ease of manufacturing, weight and cost considerations. We herein explore a new percolation reduction strategy based on in-situ phase selective synthesis of silver particles within a single phase of a biphasic epoxy system. Upon curing, the aqueous phase which hosted the silver precursor evaporates and silver precipitates in a continuous network between epoxy solids aggregates.

The phase selective filler synthesis silver-epoxy composite (PSFS-SEC) samples and base materials were characterized with optical and electronic microscopy, and the electrical conductivity was determined using a standard four points method. The equation of percolation was fitted to the experimental data, yielding a threshold as low as 0.27 vol.%. At the highest loading investigated of 12.32 vol.%, the resistivity was of 2×10^{-4} Ω·cm which is only 15 times higher than the ideal resistivity of a perfectly connected silver network in insulating media. The technology requires a high processing temperature of 210 °C and a layer-by-layer coating process, which currently limit

its applications. It is thought that a better understanding of the curing dynamics and addition of further components may enhance the material's ease of fabrication. PSFS-SECs are promising for highly conductive coatings and adhesives applications.

4.2 Introduction

The addition of electrically conductive fillers in polymeric composites is a promising method for many applications such as the electromagnetic interference (EMI) protection [116, 117], low temperature alternative to soldering in electronics packaging [118], bonding of space antenna structures [119] and lightning strike protection systems [32, 33, 113]. To achieve a transition from the insulating state to the conductive state, a conduction network has to be established through the material. The onset of this network is a statistical process that happens at a characteristic filler volume fraction for a given polymer/filler pair under identical processing conditions called the percolation threshold [70]. A low percolation threshold has been observed in polymers filled with high aspect ratio particles such as carbon nanotubes [7, 71, 120] and metallic nanowires [121]. Unfortunately, while individual carbon nanotubes have high current carrying capabilities, their composites typically reach maximum conductivities 4 to 13 orders of magnitude lower than that of metals [7] which limit their applications to charge dissipating and EMI protection purposes. Metallic nanowires on the other hand retain their charge transport capabilities [121] and achieve low percolation thresholds, but are prohibitively expensive for widespread usage.

Most fillers used in high conductivity polymeric composites are flake or spherical shaped with low aspect ratios. Such adhesives typically display percolation thresholds between 11-13 vol% for flakes [122, 123] to 25-33.5 vol.% [122, 124] for spherical powders. Since noble metals are chemically stable, they are preferred for low resistivity applications [124]. Those metals are expensive, so a decrease in the volume ratio at percolation threshold would be desirable. At the same time, noble metals such as gold and silver are heavy and the added weight is detrimental to some applications such as aerospace components. Moreover, such high volume ratios cause the viscosity of the uncured composite to go up, which in turn causes manufacturing and handling limitations.

The problem of lowering the percolation threshold has attracted considerable attention since the rise in interest for conductive composites. Already in 1994, Gubbels *et al* [125] showed that the

percolation threshold of carbon black in polymers could be lowered by an order of magnitude by inducing the selective localization of fillers at the interface between co-continuous phases in an immiscible blend of polystyrene and polyethylene. More recently, Capozzi et al. [98] demonstrated that a low percolation threshold could be obtained by confining indium tin oxide (ITO) conductive particles to the grain boundaries of composites obtained by compression molding of poly(methyl methacrylate) powders mixed with ITO. In 2012, Li et al. [126] obtained a low percolation threshold with the selective dissolution of a co-continuous polystyrene (PS)/polypropylene (PP) blend with carbon black confined to the PS. As the PS phase is selectively dissolved, carbon black is released. When the solvent dries, carbon black particles assemble on the 2D topology of the phase boundaries. These methods all rely on selective localization of fillers within the polymeric matrix to enhance the percolation probability.

We herein present a technique for lowering the percolation threshold in highly conductive epoxy-silver composites. The phase selective filler synthesis silver epoxy composite materials (PSFS-SEC) rely on the in-situ synthesis of silver nanoparticles within the aqueous phase of an epoxy emulsion. The experimental section details the procedure for PSFS-SEC samples. The results and discussion section provides insights about the microstructural particularities of PSFS-SEC's, along with their electrical properties at different filler loadings. Electrical properties of epoxy samples filled with silver particles representative of commercial solutions are presented for comparison. The curing mechanisms of PSFS-SECs are also discussed. Finally, the current limitations of the technology along with possible solutions and applications for PSFS-SECs are discussed.

4.3 Experimental

4.3.1 Silver ink preparation

Particle-less silver precursor ink was prepared according to Walker and Lewis [112]. 8g silver acetate ReagentPlus® 99% (Sigma Aldrich) was dissolved into 20 ml 28-30% ACS reagent ammonium hydroxide (Sigma Aldrich) at room temperature under moderate magnetic stirring. At this point the solution had a clear yellow tint. 1.6 ml formic acid ACS reagent >88% (Sigma Aldrich) was then added drop wise while stirring continuously. The solution turned from yellow to gray as large silver aggregates precipitated. The solution was then transferred in a hermetic vial and left to rest until the gray particles sedimented. The clear supernatant was collected and the

precipitate was discarded. Upon evaporation, the diamminesilver ions in solution are reduced to elemental silver and silver acetate. Further heating to 90 °C leaves pure elemental silver. The silver mass content of the ink was found to be 18 wt.% by assessing the mass loss of a small quantity of silver ink upon evaporation and heating at 100° for several minutes.

4.3.2 PSFS-SEC samples preparation

The epoxy resin emulsion EPI-REZ 5522-WY-55 and EPIKURE 8290-Y-60 hardener (Momentive Performance Materials Inc.) were mixed in the ratio 4:1 according to resin mass and stirred for 2 minutes after the mixture appeared homogeneous. Viscosity was lowered by adding 1 ml deionized H_2O for every 5g of resin/hardener mixture. The mixture was placed on a magnetic mixer and various amounts of the prepared silver ink were added dropwise. The mixture was then immediately transferred to a custom made reservoir for the dip-coating operation. Prior to the coating operation, microscope slides were thoroughly cleaned with acetone and isopropanol. A layer of the epoxy-silver ink mixture was then applied using the dip-coating method. The slides were manually dipped in the reservoir and removed slowly. The backside of the slide was then wiped clean and the microscope slide was held horizontally for the liquid to spread evenly under the action of gravity. The sample was then placed in an oven heated at 210 °C for 1 minute. The short time was chosen to minimize epoxy degradation while maximizing silver conversion. The whole dipping procedure was repeated. 15 layers were required to build a solid coating 8 to 30 µm thick, depending on the mixture's residual solids and viscosity.

4.3.3 Conductivity measurements

Sample conductivity was measured with a Jandel tungsten tip cylindrical four point probe with regular linear array spacing of 1mm. The voltage reading was performed by a Agilent 34401A multimeter and the current was generated by a Keithley 220 programmable current source. For each sample, three or more voltage vs. current curves were obtained at different areas of the sample, depending on the spread in data. The average resistivity measurement was obtained by fitting a linear voltage vs. current relation on the data points. The equation was not forced through the origin and the resistivity was obtained from the slope of the current-voltage relation. The standard current distribution correction factors were applied for the probe and sample geometry, assuming a negligible sample thickness.

The PSFS-SEC sample thicknesses were measured by mapping the topology of the sample surface around holes in the coating. The holes were made by scraping the coating with a steel blade until the bare glass showed on an approximately 1 mm^2 area. The topology maps were recorded with a Dektak 3030 profilometer.

4.4 Microscopy

Optical microscope images were obtained with a Olympus BX61microscope with UPlanFL N 40X and 100X objectives. The fluorescent lighting was provided by an Olympus 100W mercury fluorescence light in a U-LH100HGAPO housing. The measurements on optical images were performed with the ImagePro 6.0 software. Electron microscopy images were realized on a JEOL JSM7600F field-effect scanning electron microscope (FE-SEM).

4.5 Results and discussion

4.5.1 Microstructural characterization

Figure 4.1 shows an image of the epoxy resin emulsion. The size of epoxy colloids is at the limit of the resolution of the equipment and there is significant blurring due to the narrow depth of field obtained at such magnification. However, epoxy solids appear as distinct black dots and can be clearly distinguished from the aqueous media. Size measurements are therefore possible. Figure 4.1 b) shows the size distribution of the epoxy solids droplets in the emulsion as measured from the features shown in a). The statistics obtained on 5249 features indicate that the majority of the epoxy droplets are sub-micron sized, with a modal value around 0.63 µm and a mean value of 0.98 µm.

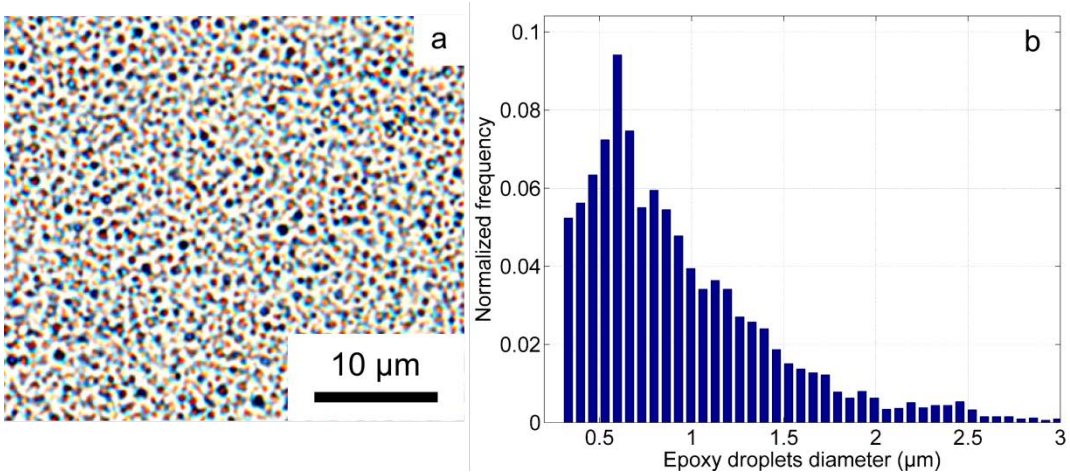

Figure 4.1: a) Representative optical microscope image of the EPI-REZ 5522-WY-55 epoxy emulsion. b) Size distribution of epoxy solids colloids within the emulsion. The mean size is 0.98 µm and the modal value lies within the [0.6, 0.66] µm interval. The measurements were performed on image a)

Figure 4.2 represents a single layer of cured PSFS-SEC with 4.4 vol. % silver content. The contrast between phases was obtained using simultaneously backlighting with white light and front lighting with fluorescence lighting. Pure epoxy is translucid and silver is opaque. Therefore, the phase that displays a yellow tint is attributable to an epoxy-rich phase as it is lit by the transmitted white light. The yellow tint is concordant with the color of the cured resin. The opaque phase appears a bright blue under fluorescence lighting , suggesting it is attributable to the presence of silver as a strong surface plasmon resonance at 450 nm exists for silver nanoparticles in the 70-150 nm size range [127]. Therefore, the distinct contrast in the image is attributable to a phase separation between silver-rich and epoxy-rich phases. This separation allows for the concentration of filler particles in a restrained volume, which effectively promotes the volume ratio and percolation of conductive fillers within the sub-phase.

The comparison of particle sizes before (Figure 4.1) and after curing (Figure 4.2) suggests that aggregation of epoxy solids occur during the evaporation of the aqueous phase as the sub-micron features are converted to large tens of microns across islands in the cured composite. Small round-shaped opaque details appear in the epoxy-rich phase of Figure 4.2 that retain approximately the particle size of the initial epoxy droplets, suggesting that some of the silver is formed at the early stages of epoxy particles agglomeration and is trapped between the original droplets.

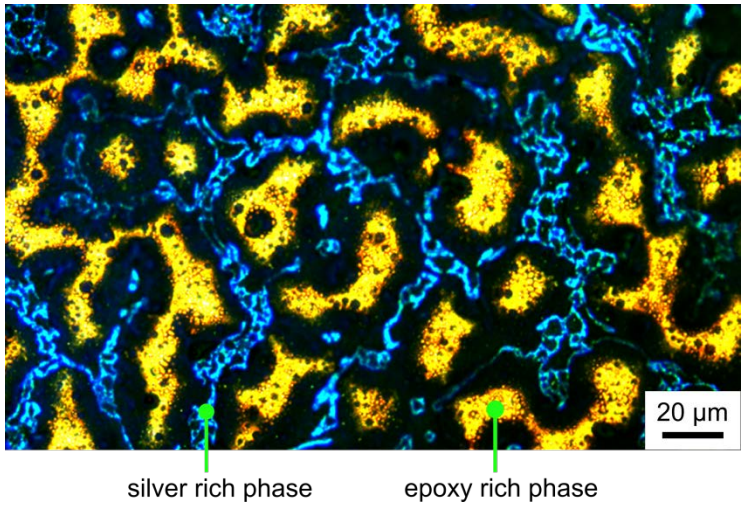

Figure 4.2: Optical microscope image of an epoxy emulsion-silver ink sample with 4.4 vol.% silver content. The epoxy phase is lit by light transmission while the silver-rich phase is lit with reflected fluorescent lighting

Figure 4.3 shows SEM images of the surface of a 12.3 vol.% PSFS-SEC sample with the detector set to low angle backscattered electron (LABE) mode. The backscattering yield of the target atoms is proportional to the differential cross-section on the direction of interest. Since the differential cross section generally increases with atomic mass, the backscattering yield for silver is higher than for epoxy, hence silver appears bright while epoxy is dark and transparent as electrons can travel a long way without interaction. In Figure 4.3 a), the characteristic length scale of approximately 10µm of the epoxy-rich islands is coherent with the features found in Figure 4.2.

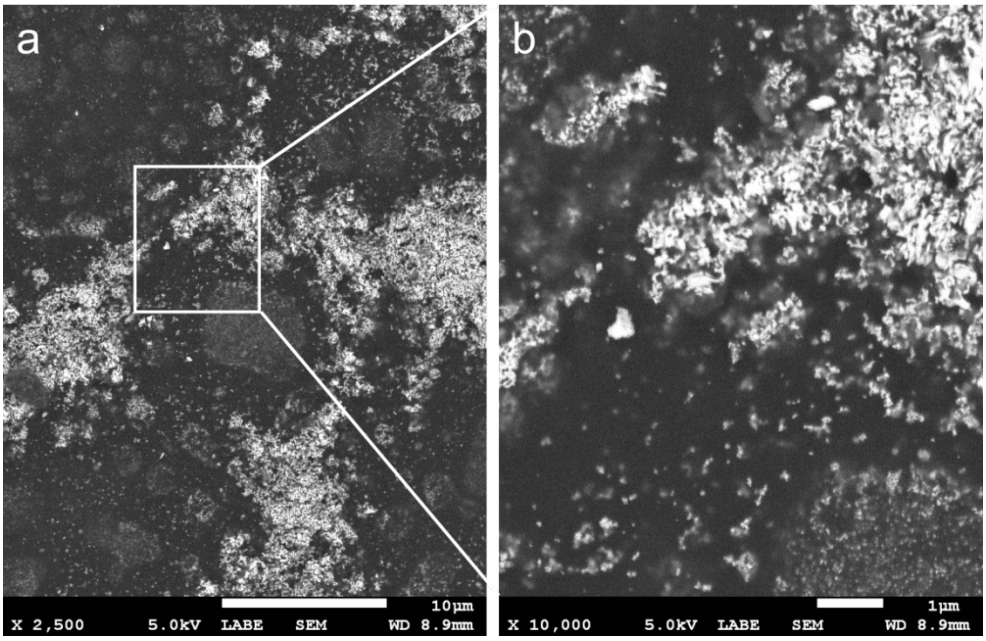

Figure 4.3: SEM images of the cured epoxy-silver composite in low angle backscattered electron imaging. Silver appears bright while epoxy is dark and transparent

Figure 4.3b) is a zoom-in of the zone depicted in a). The silver particles are found to be nano-sized, and it is seen that a fraction of silver particles are entrapped in the bulk of the epoxy phase where they cannot participate to the conduction network. These findings confirm the observations made earlier and suggest that epoxy solids aggregation and silver precipitation simultaneously happen during the evaporation of the aqueous media, with a slight edge to the aggregation mechanism. As the evaporation begins, aggregation of the epoxy happens quickly and large epoxy islands appear. During this step, only a little amount of silver precipitates, which is trapped between the original sub-micron sized epoxy droplets. As the evaporation further proceeds, the silver precipitation reaction speeds up, and the metal is confined in the area between large aggregates of epoxy solids, giving rise to the structures tens of microns across seen in Figure 4.2 and Figure 4.3.

4.6 Electrical characterization

Figure 4.4 shows the raw current-voltage data collected on samples prepared with 2.96, 4.37, 5.74 and 12.32 Ag vol.%. Other concentrations were studied but were omitted here for the sake of clarity. The resistivity values for all concentrations studied are listed in Table 4.1.The linear curve fit incorporates all the data points and was not forced through zero as a small voltage offset may

exist. The spread in the data originates from differences in resistivity when the probe was moved from a sample area to the other. The uncertainties listed in Table 4.1 reflect these differences.

Table 4.1: Experimental resistivity values for PSFS-SEC samples with various silver loadings

Vol.% Ag	2.96	4.37	5.06	5.74	6.41	7.72	12.32
Resistivity (mΩ·cm)	11.1±0.96	4.05±0.19	2.69±0.62	1.99±0.46	1.43±0.29	0.884±0.1	0.185±0.02

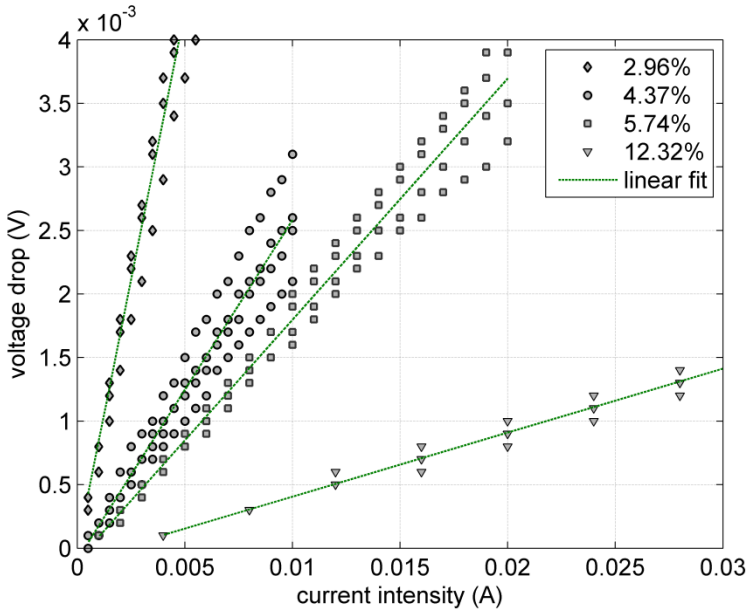

Figure 4.4: Current-voltage curves for PSFS-SEC samples of various silver loadings

At the highest loading of 12.32 vol.%, the PSFS-SEC resistivity is only 15 times higher than the ideal resistivity of an imaginary perfectly connected silver-epoxy composite with equal loading, as given by the rule of mixtures. This underlines the material's efficiency in establishing a conductive network of filler particles.

Figure 4.5 shows the evolution of the resistivity of the material with increasing Ag filler volume ratio. In percolation theory, the conductivity of a composite relative to its filler content follows a power law in the form:

$$\rho = \rho_0(\Phi - \Phi_c)^t, \tag{10}$$

where ρ_0 is the resistivity of the bulk filler material, t is a constant, Φ is the filler volume content and Φ_c is the percolation threshold. The constant t is the critical exponent. It is related to the rate

of improvement of the conductive network after the critical concentration is achieved at the percolation threshold [128]. Considering a perfectly connected network of conductive particles embedded in the polymer resumes the problem to a simple expression of the rule of mixtures, corresponding to equation (1) with $\Phi_c = 0, t = -1$. Hence the efficiency of the material to form a network is increased when those values are approached.

The percolation power law relation was fitted using a least squares approach on the experimental data. The result of the fit can be seen in Figure 4.5 as the dotted line. The best fit yielded a Φ_c value of 0.0027 and a t value of -2.45. The fit yielded very good agreement to the data, with a squared residuals sum of 4.243×10^{-8} for a R^2 value of 0.9995. Therefore, the percolation framework indicates a percolation threshold as low as 0.27%. This value is remarkably low for a metal-polymer composite. Lee et al. [122] found a percolation threshold as high as 33.5% for spherical silver nanoparticles in a polyvinyl acetate emulsion, more than two orders of magnitude higher than our findings. Wu et al. [124] investigated the effect of filler size on percolation threshold in spherical silver nanoparticles-epoxy systems. They found percolation ratios ranging from 15.6 to 25 Ag vol.%. The optimization of particle size therefore accounts for the lowering of the percolation threshold by a factor of 2 or so. Nam et al [129] observed a decrease in the percolation threshold of an epoxy-silver nanospheres system from 24 to 22.5 Ag vol.% upon addition of silica nanospheres to the composite. In comparison, our method allows for a 100-fold decrease in the percolation threshold, as compared to the silver nanospheres-epoxy system. This result suggests that the percolation mechanism in PSFS-SECs is extremely efficient. Current conductive adhesives typically incorporate silver flakes in epoxy. The typical filler loading of this system is of 35-30% [124] with a percolation threshold around 11 vol.% [122]. PSFS-SECs offer a 40-fold decrease of this value, which would allow for considerable savings in material costs and weight.

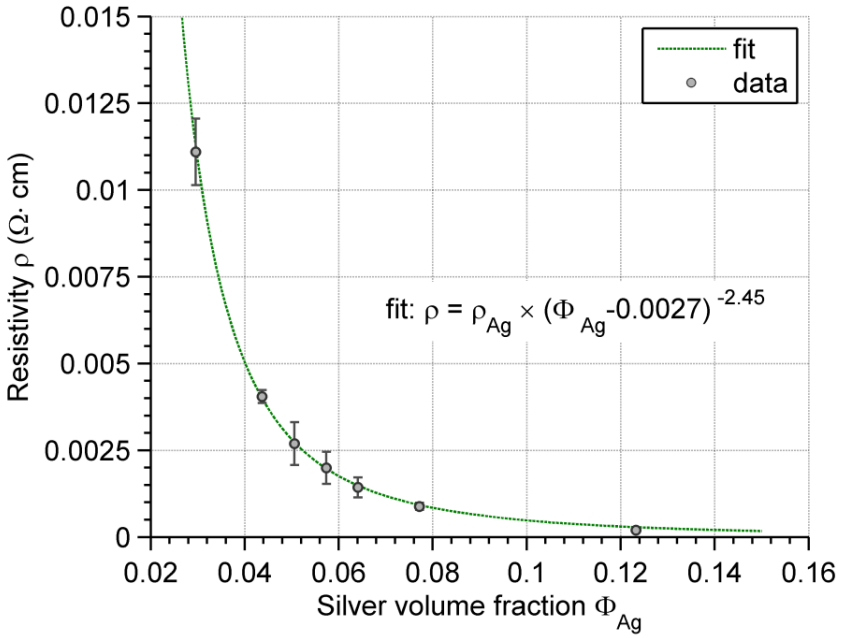

Figure 4.5: Evolution of the PSFS-SEC's resistivity with silver volume content the green dotted line is the best fit of the percolation power law

The theoretical critical exponent for percolation lies between the values of 1.5 and 1.9 [128, 130]. The value found here greatly exceeds those values, indicating that the percolation mechanism in the biphasic emulsion system may not be correctly described by percolation theory. However, such a discrepancy with theory is predictable since percolation theory does not take into account any effect related with phase separation. Mamunya et al.[130] found values of t as high as 3.2 for poly (vinyl-chloride)-copper composites The samples were prepared with the compression molding of a mix of polymer and copper nanoparticles powders. The authors underline that real cases often diverge from the theoretical value. They argue that the theory does not take into account particle shapes, interaction between fillers and resin and between individual particles and inhomogeneities caused by processing conditions.

The PSFS-SEC technology is currently limited by the layer by layer application process which is not suitable for adhesive or low-temperature soldering applications. The need for silver ink evaporation requires that gases be evacuated from the bulk of the material. Also, the high processing temperature of 210 °C is not suitable for many substrates. However, the silver ink alone only requires a 90 °C temperature for complete conversion to elemental silver. It is thought that a better knowledge of the curing dynamics of the composite could provide insight on how the

processing temperature could be lowered. The addition of fillers such as carbon nanotubes could also provide pathways for gas evacuation [131] while adding the freedom to control the uncured material's viscosity. If these problems were to be solved, PSFS-SECs could be very interesting candidates for next generation conductive adhesives and coatings.

4.7 Conclusion

We demonstrated that the in-situ formation of silver fillers from an aqueous silver precursor ink in an emulsified epoxy formulation could lead to a phase separation mechanism beneficial to the establishment of a conductive network within the material. The initial length scale of the epoxy colloids is not retained in the process, indicating that the elemental silver particle formation and epoxy coalescence mechanisms operate on different time scales.

The novel method for the enhancement of the percolation mechanism in silver-epoxy composites has allowed an improvement of two orders of magnitude in the percolation threshold as compared with the case of silver powders in epoxy. A comparison with the technology representative of the commercial solutions, namely silver flakes dispersed in epoxy matrix, yielded a significant 40-fold improvement in the percolation threshold. While percolation theory was not developed on similar grounds, it describes with great accuracy the evolution of the resistivity with conductive filler volume fraction.

The PSFS-SEC method allows for a very low viscosity material before curing that can be sprayed on a substrate, making it a good candidate for conductive coatings. The method presently requires a high curing temperature of 210 °C and a layer-by-layer application, but it is believed that a better understanding of the curing dynamics could help in facilitating the application of the technology. Further research is planned on the subject.

4.8 Acknowledgements

The authors acknowledge the financial support from Le Fonds Québécois de la Recherche sur la Nature et les Technologies (FQRNT), Natural Sciences and Engineering Research Council of Canada (NSERC), and Consortium for Research and Innovation in Aerospace in Quebec (CRIAQ). The authors acknowledge also the financial support from Bombardier Aerospace, Bell Helicopter

and 3M Canada. The authors would like to thank the technical support of Mr. Rouhollah Farahani for consulting work on nanocomposites fabrication.

CHAPTER 5 ARTICLE 2: SYNTHESIS OF HIGHLY CONDUCTIVE, UNIFORMLY SILVER-COATED CARBON NANOFIBERS BY ELECTROLESS DEPOSITION

Xavier Cauchy, Jolanta-Ewa Klemberg-Sapieha and Daniel Therriault*

Laboratory for Multi-scale Mechanics, École Polytechnique de Montréal, P.O. Box 6079, Station Downtown, Montreal (QC), H3C 3A7, Canada

ACS Applied Materials and Interfaces, 14th of July, 2017.

5.1 Abstract

Noble metal coated carbon-based nanoparticles when used as electrically conductive fillers have the potential to provide excellent conductivity without the high weight and cost normally associated with metals such as silver and gold. To this effect, many attempts were made to deposit uniform layers of metals on core nanoparticles with an emphasis on silver for its high conductivity. The results so far were disheartening with the metal morphology being better described as a decoration than a coating with small effects on the electrical conductivity of the bulk particles. We tackled in this work the specific problem of electroless deposition of silver on carbon nanofibers (CNFs) with the investigation of every step of the process. We performed X-ray photoelectron spectroscopy (XPS), transmission and scanning electron microscopy (TEM, SEM), Zeta potential and electrical conductivity measurements to identify a repeatable, reliable set of parameters allowing for a uniform and fully connected silver deposition on the surface of the CNFs. The bulk particles' specific electrical conductivity (conductivity per unit mass) undergoes a more than ten-fold increase during the deposition, reaching 2500 $S \cdot cm^2/g$, which indicates that the added metal mass participates efficiently to the conduction network. The particles keep their high aspect ratio through the process, which enables a percolated conduction network at very low volume loadings in a composite. No by-products are produced during the reaction, so the particles do not have to be sorted or purified, can be used as produced and the reaction time is ~15 minutes. The particles might be an interesting replacement to conventional fillers in isotropic conductive adhesives, as a conductive network is obtained at a much lower loading. They might also serve as electrically

conductive fillers in composites where a high conductivity is needed, such as lightning strike protection systems, or as high surface area silver electrodes.

5.2 Introduction

Electrically conductive nanoparticles have attracted considerable attention from researchers because of their ability to impart electrical transport properties to otherwise insulating polymers. Applications such as isotropic conductive adhesives (ICAs) for heat sensitive electronics [132] or lightning strike protection for composite aircraft skins [8] require very high conductivities for efficiency and safety, respectively. Carbon nanotubes (CNTs) were heavily investigated as electrically conductive fillers [5, 7, 68, 71, 133] because of the potentially very high transport capabilities of individual particles [48]. Moreover, these particles were shown to allow electrical transport in polymers at very low concentrations because of their high aspect ratio [7, 68]. However, the electrical performance of CNT-loaded composites always lagged behind expectations with maximum conductivities in the range 10^{-3}-10^{-1} S/m [68, 69, 116, 134], far lower than the typical 10^{7} S/m value for high conductivity metals. The explanation for this disappointing performance lies in a strong tunneling resistance between individual particles [133] and in high contact resistance depending on the configuration of the adjacent particles [135]. There is also an important disparity between the conductivity values of CNT-filled polymers [7] since dispersion state, nanotube type and surface treatment have considerable impact on the end result [54, 68]. For these reasons, the fillers of choice for isotropic conductive adhesives remain metallic. Silver particles are the norm since silver has the highest conductivity of all metals. Moreover, silver nanostructures have been shown to be able to sinter at low temperature [136], under microwave irradiation [108], chemically at room temperature [103] and with infrared irradiation [137]. Silver however suffers from two principal drawbacks: it is expensive and, at 10.49 g/cm^3, it is heavy. These two drawbacks can be diminished by lowering the silver content in the composite material. Increasing the aspect ratio of fillers is a proven strategy in order to obtain lower percolation thresholds and thus a higher conductivity at a lower loading [138]. However, major obstacles remain to the scalability of silver nanowires production. Among these, a time consuming purification process, loss of silver metal inherent to the polyol method, long synthesis times and low production rates are often cited [139-141]. Our strategy is then to circumvent these shortcomings by using high aspect ratio carbonaceous particles as templates for electroless

deposition of silver to obtain high aspect ratio hybrid particles with low metal to metal inter-particle contact resistance and thus provide an alternative path for high performance electrically conductive nanofillers.

Electroless deposition is a technique used extensively in the last century to produce mirrors [142, 143]. It has however been revisited lately for applications in nanotechnology, where small complicated geometries cannot be coated with vapor deposition processes [144]. Electroless deposition was successfully used to metallize complicated microstructures [144, 145] and to fabricate surface plasmon resonance sensors [146] and surface-enhanced Raman scattering substrates [147, 148]. Deposition on carbonaceous substrates has been attempted with varying success. The conductivity of graphite-filled ICAs was shown to increase by up to two orders of magnitude with electroless silver deposition [149, 150] and a uniform coating was obtained on carbon spheres [151, 152], but the deposition on nano-sized particles proved to be more challenging. The process applied to carbon nanotubes resulted in mere decoration [113, 153], a discontinuous coating [154-157] or loss of aspect ratio [158, 159]. Arai *et al*. did show convincingly that pure nickel and Ni-B alloy electroless deposition on vapor-grown nanofibers could yield an excellent coating uniformity [160, 161]. The same group attempted silver electroless deposition with silver iodide and dimethylaminoborane as a reducing agent. The method was less successful as the coating continuity was not acheived [162].

We herein show that electroless deposition of silver metal on carbon nanofibers (CNFs) can result in a smooth silver coating with preservation of the particles' high aspect ratio. We provide detailed analysis of every step of the process, namely functionalization, sensitization and deposition through the use of X-ray photoelectron spectroscopy (XPS), transmission electron microscopy (TEM), scanning electron microscopy (SEM) and electrical conductivity measurements, among others. We provide a window of working parameters for each step with insight into possible underlying mechanisms. We finally show that the process results in uniformly silver coated carbon nanofibers with improved bulk electrical conductivity.

5.3 Experimental section

5.3.1 Functionalization

CNFs (PR-25-XT-HHT Pyrograf® Products Inc.) were acquired from Sigma Aldrich. The nanofibers have a nominal diameter of 100 nm and a nominal length between 50 and 200 µm. Functionalization was carried out by immersing 1g of CNFs in 70 mL of a mixture of HNO_3 (Anachemia ACS 68-70%) and H_2SO_4 (Anachemia ACS 95-98%) in the volume ratio of 1:3 and sonicating it for 3 hours in an ultrasonication bath (42 kHz Cole-Parmer 08891-11). Alternatively, CNFs were functionalized by refluxing in the same acid mixture in a round bottom flask with magnetic stirring. The flask was immersed in a silicon oil bath heated to various temperatures and the reaction was performed for 1 and 3 h. The functionalized particles were filtered out using 0.4 µm pore diameter polycarbonate membranes and a vacuum filtration apparatus. Particles were rinsed with deionized water until a neutral pH was reached and were then stored in deionized water.

5.3.2 Sensitization

Stannous chloride dihydrate ($SnCl_2 \cdot 2H_2O$, 98%) from manufacturer Alfa Aesar was acquired from VWR. All solutions were obtained by first dissolving the $SnCl_2$ in deionized water to obtain a 10 g/L concentration and adding various amounts of HCl to dissolve the precipitate (more details will be discussed in Results and discussion Section). Functionalized CNFs were filtered out from the deionized water and dispersed in the acidic $SnCl_2$ solution by mechanically disrupting aggregates with a stirring rod in 10 ml of solution. 30 ml of solution was added and the mixture was sonicated for 2 minutes. Aggregates were then decanted and the procedure was repeated until a nanofiber concentration of 625 mg/L was reached. The dispersion was then placed in a sealed glass bottle and sonicated for 45 minutes, followed by a 90 min dwell and another 45 min sonication with temperature kept below 45 °C, as confirmed through monitoring with a thermocouple. Particles were filtered out of the solution by vacuum filtration and redispersed in deionized water. The rinsing operation was repeated 5 times and the filtrate was tested for Cl^- ions by adding aqueous silver nitrate ($AgNO_3$). If Cl^- ions are present in solution, silver chloride (AgCl) precipitates and the solution turns cloudy. Sensitized CNFs were stored in 18 MΩ pure water at a concentration of 100 mg CNFs for 350 mL H_2O.

5.3.3 Tollen's Reagent

$AgNO_3$ (ACS reagent, Alfa Aesar) acquired from VWR was dissolved in 60 mL of 18 MΩ pure water for a 0.5 M concentration. Under magnetic stirring, 1 mL of a 6×10^{-2} M KOH solution was added to the solution. At this point the solution exhibits a cloudy yellow color. Ammonium hydroxide (Alfa Aesar, 28% NH_3) was then added dropwise. The solution turned dark brown before it gradually cleared up and became transparent again. Just enough ammonia was added to make the solution transparent, which amounts to ~4-5 mL, depending on the residual NH_3 content in the reagent.

5.3.4 Reducing solution

For the investigation of the effect of Tollens' reagent volume, a reducer master batch was prepared by adding 6 mL of denatured ethanol to 36 g of a 20% dextrose solution. 70 g of a sensitized CNF dispersion with 0.029% CNF content by weight was added to the reducer master batch. The resulting solution was divided equally into 8 glass vials.

For the investigation of the effect of dextrose concentration, 8.75 g of the same sensitized 0.029% CNF dispersion masterbatch was added to each of 8 glass vials. After adding 3.6 mL of pure water, dextrose was added in quantities varying from 35.5 mg to 4.544 g, doubling the concentration from sample to sample and keeping the water mass the same as in the investigation of Tollens' reagent volume. 750 µL of ethanol was then added to each sample.

5.3.5 Reaction

The Tollens' reagent was added to the glass vials containing the sensitized CNFs and the reducing solution. The vials were closed airtight and were agitated for 15 minutes for the reaction to proceed. The solution was then poured in 40 mL of deionized water and rinsed twice with 80 mL of deionized water by vacuum filtration. The resulting nanoparticles, in layers evenly deposited on a polycarbonate membrane, were dried overnight under vacuum and weighed.

5.3.6 Characterization

Electrical conductivity was measured using a 4 point probe (Jandel 100µm tip, 1 mm spacing, linear array) hooked to a current source (Keithley 220) and multimeter (Hewlett Packard 34401A).

Three sets of voltage vs. current measurements were obtained on different zones of the sample and a two parameter linear fit was performed to determine the conductivity value. The error on conductivity values corresponds to the standard deviation of the conductivity value for the different data sets.

SEM images were obtained using a JEOL JSM7600F field emission scanning electron microscope in secondary electron imaging mode. The acceleration tension was set at 10.0 kV with a working distance of approximately 8 mm. TEM images were obtained on a JEOL JEM-2100F microscope equipped with a field emission electron gun. Acceleration voltage was 200 kV.

XPS was performed using a VG scientific ESCALAB 3MKII apparatus with the Mg Kα ray as the X-ray source. The sampling depth was 50-100 Å. The background subtraction was performed with the Shirley method and atomic sensitivity factors were derived by Wagner.

Zeta potential was measured using a Malvern Instruments Zetasizer Nano ZSP analyzer. The sensitized CNF solution was diluted to 20 times its volume before analyzing. The Malvern universal dip cell with a glass cuvette was used. Zeta potential was calculated using the Smoluchowski method.

5.4 Results and discussion

5.4.1 Starting Material and functionalization

As-received CNFs are described by the manufacturer as having a stacked-cup core with a graphitized chemical vapor deposited carbon overcoat. Figure 5.1-a shows a schematic of the nanofiber structure: the graphitic planes organize in a conical shape, which stacks in the axial direction. Graphitization of the vapor-deposited carbon at 3000 °C causes the atoms to organize in concentric graphitic planes, similar to the structure of multiwall carbon nanotubes. Figure 5.1-b is a TEM image of the as-received particles that confirms the structure of a typical nanofiber. However, roughly 10% of the fibers observed exhibited the structure depicted in Figure 5.1-c and d, which is commonly known as the *bamboo shaped* structure. Figure 5.1-e shows a high-resolution XPS spectrum obtained for the as-received product. The analysis showed a very clean 100% carbon signal. The inset shows a magnification of the C1s asymmetrical peak typical of highly graphitic carbon. The component at 286.4 eV represents 88.7 at. % and is attributable to carbon bonding in

the sp^2 hybridization state. The remaining 11.3 at. % are found at 291.3 eV, typical of bonding-antibonding transitions in π orbitals accompanying sp^2 carbon. The absence of sp^3 carbon is indicative of a highly graphitic surface.

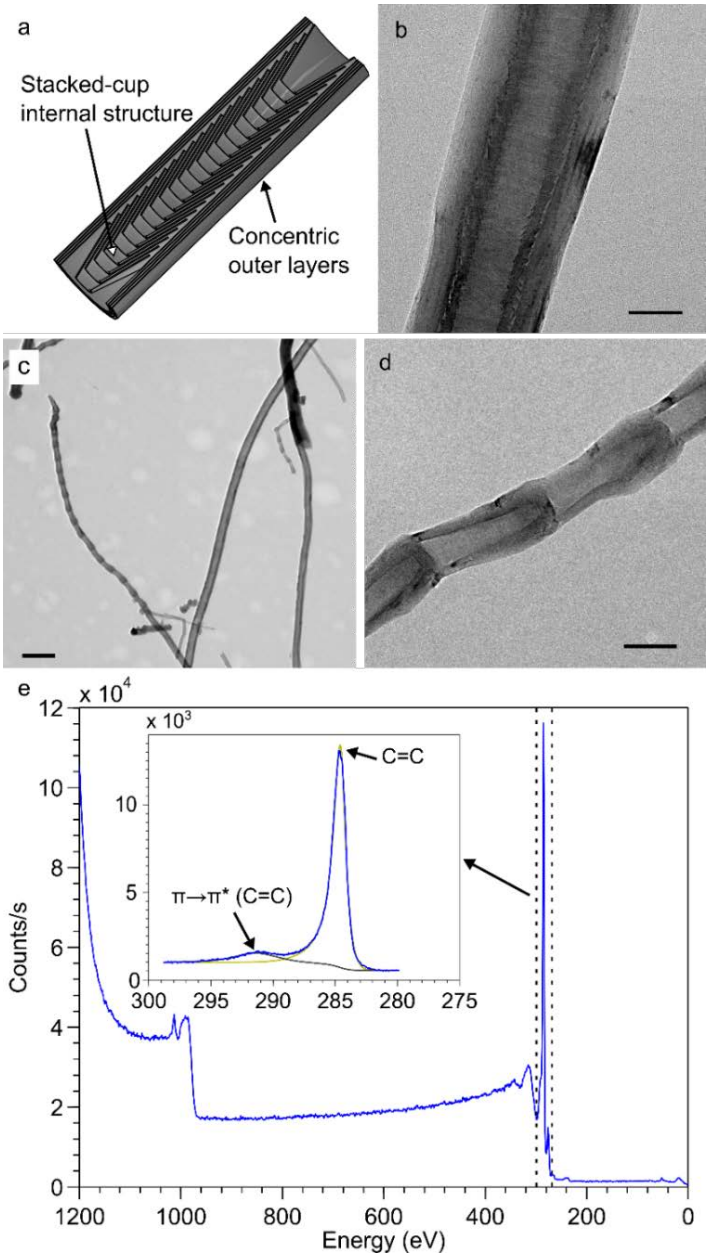

Figure 5.1: As-received CNFs characterization. a) Schematics of the CNF graphitic planes structure. b) TEM image showing the concentric and stacked cup regions of a typical CNF (scale bar 50 nm). c) TEM image showing the high aspect ratio of the CNFs both bamboo shaped and concentric-stacked cup type (scale bar 1 μm). d) A close-up of a bamboo shaped CNF. The graphitic planes configuration is clearly visible (scale bar 100 nm). e) XPS survey of pristine CNFs. Only the carbon peak is visible. The inset shows a high resolution spectrum of the carbon C1s peak. It shows only graphitic carbon, with the corresponding bonding-anti bonding peak

The CNFs were acid functionalized to ensure a clean surface and enhance wetting for the subsequent sensitization step. A 3:1 vol. H_2SO_4:HNO_3 mixture is a proven acid mixture for attachment of oxygen-containing groups on the surface of CNTs and CNFs [78]. We investigated the effect of different times and temperatures on the surface composition of functionalized CNFs with XPS. The results are summarized in Table 5.1. Other than the extent of the functionalization, the conservation of the structural integrity of the nanoparticles is of prime importance since high aspect ratio conductive particles are sought at the final step of the process. It was shown that functionalization in this particular mixture of acids leads to a loss of material, and therefore a strong degradation of the particles' structure starting at a mixture temperature of 70 °C, and that the yield is as low as 30% for a temperature of 100 °C [78]. Data in Table **5.1** shows that the surface oxygen content of nanoparticles treated at 60 °C is considerably lower than for those treated at 75 and 90 °C. However, a comparison of the increase in oxygen content in particles treated for 1 and 3 hours shows that it doubles for particles treated at 60 °C while it stays nearly constant for those at 90 °C. This suggests that the acid treatment will give equivalent results at low temperature if performed for longer times while preserving the CNF aspect ratio.

Table 5.1: Oxygen at. % on CNF surface for different treatment conditions

Method	Refluxing					Ultrasonic agitation
Time (h)	1			3		3
Temperature (°C)	60	75	95	60	90	< 45
oxygen atomic %	5.2	10.2	14.2	10.6	15.1	11.7

We also investigated acid treatment coupled with ultrasonic agitation for low temperature functionalization. The same mixture was immersed in the ultrasonic bath for 3 hours before filtration. During the treatment, the water bath temperature rose from 23 °C to 45 °C because of the dissipated ultrasonic energy. The resulting oxygen content was 11.7%, which is higher than for a 3 h treatment at 60 °C without ultrasonication. Since the goal is to avoid the degradation of

nanoparticles and low yield associated with an acid mixture temperature over 70 °C, we needed to verify to what extent the nanoparticle structure was affected by sonication. Figure 5.2-a shows a TEM image of CNFs after ultrasonically assisted functionalization. The image confirms that the high 100+ aspect ratio is conserved through the low temperature ultrasonically assisted treatment. Figure 5.2-b shows the typical damage found after functionalization: a faint band is visible on the particle boundary that is attributable to lifted graphitic planes, although roughly half the particles did not display any noticeable damage. Overall, the structure of the nanoparticles was preserved. Figure 5.2-c and d present the high resolution XPS spectra from the carbon and oxygen peaks of functionalized nanofibers. The peak at 289.3 eV in the C1s spectrum is attributed to O-C=O bonds with 3.9 at.% and the peaks at 287.8 and 286.6 eV are attributed to C=O and C-O bonds at 2.8 and 2.7 at.%, respectively. The presence of these bonds on the surface of functionalized CNFs is consistent with groups usually found on acid-functionalized carbon [163], with a slight prevalence of carboxylic acids. The O1s peak shows a total oxygen at.% of 12.7. Convoluted in the O1s peak is detected 2.7 at.% oxygen pertaining to adsorbed water that wasn't found on pristine nanofibers, further confirming the increased hydrophilicity of acid functionalized carbon nanofibers [78, 163]. To assess the extent of the increase in hydrophilicity, pristine and acid functionalized CNFs buckypapers were subjected to the sessile drop method for angle of contact measurements. Figure 5.3 shows an example of such measurements. On average, the functionalized CNFs showed a decrease of 15.3° in contact angle. Although modest, this increase in hydrophilicity is desired for enhanced wetting during the tin sensitization treatment.

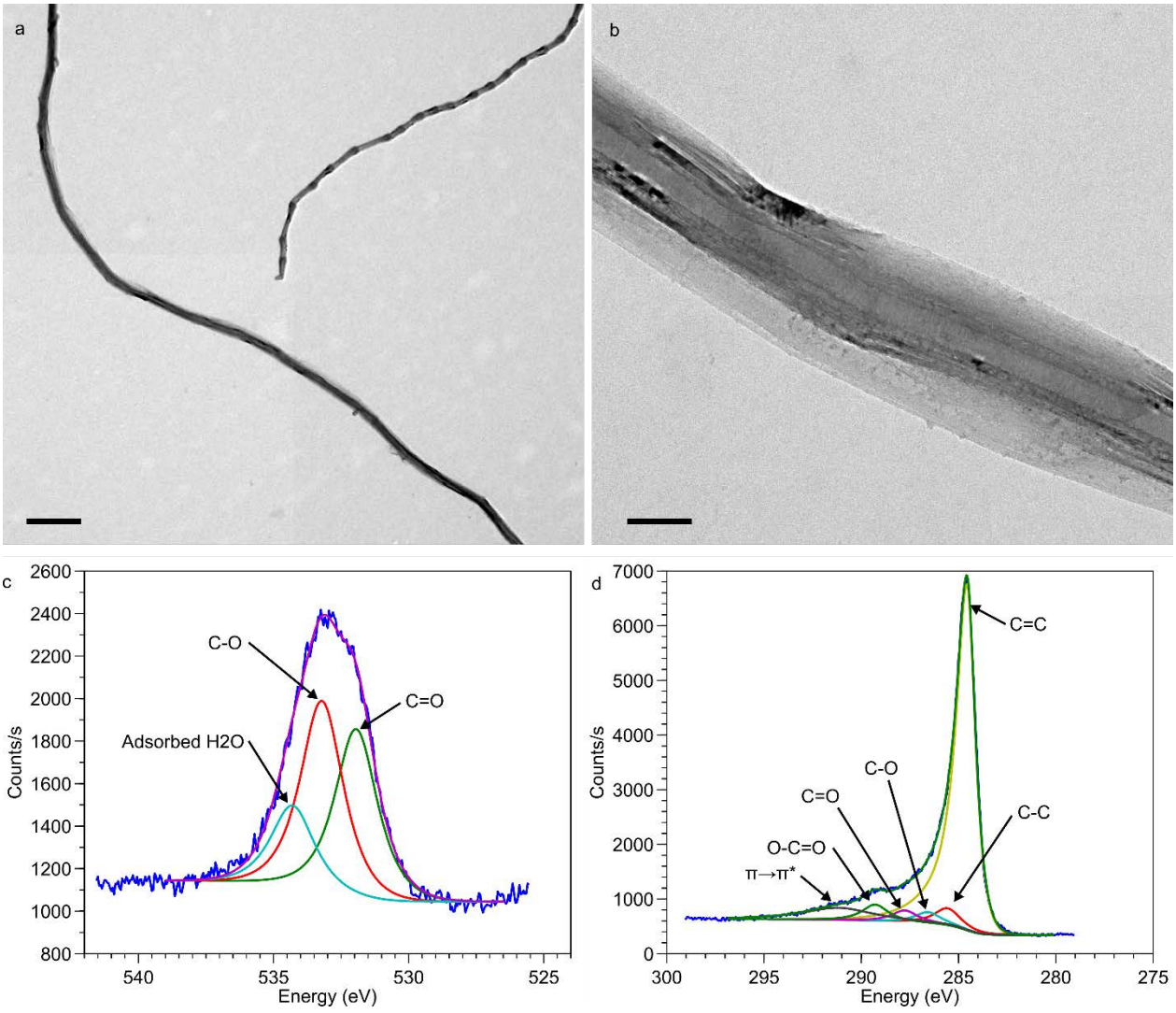

Figure 5.2: Functionalized CNFs characterization. a) TEM image showing that the aspect ratio (~100) is preserved through functionalization (scale bar 1µm). b) TEM showing lifted graphitic planes at the nanofiber surface. This is the type of damage that can be found on ultrasonically assisted acid functionalization of CNFs (scale bar 100 nm). c) XPS high resolution spectrum of the O1s peak created by functionalization. The bonds are consistent with carboxylic functional groups. d) High resolution spectrum of the C1s peak. The importance of O–C=O relative to C–O and C=O bonds show a slight prevalence of carboxylic acid groups. Many new bonds are formed compared to pristine CNFs (Figure 5.1-e)

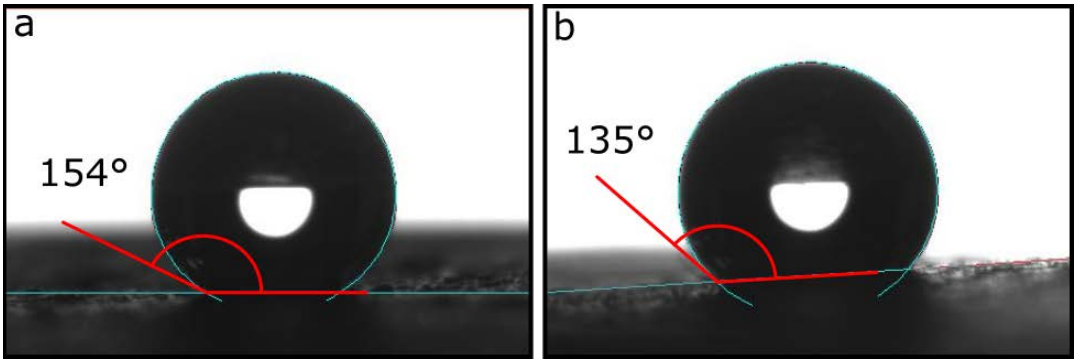

Figure 5.3: Contact angle measurements on CNF buckypapers. a) pristine CNF buckypaper. b) Acid functionalized buckypaper

5.4.2 Sensitization

The silver deposition process is initiated by reduction of Ag^{-} by Sn^{2+} on the surface to be coated [152]. The distribution of tin seeds on the CNFs during sensitization is therefore crucial to the quality of the subsequently deposited silver film. We performed sensitization by immersing the functionalized nanofibers in a $SnCl_2$ solution with the addition of HCl and exposing it to ultrasonic energy. The HCl concentration was shown to have an important influence over Sn(II) oxidation to Sn(IV) [164], activator seed density and contact angle [165]. All these parameters are thought to affect the deposited metal film quality. We therefore chose to vary HCl concentration in the $SnCl_2$ solution and investigate its effect on the dispersion stability and on the zeta potential. HCl was added in 6 concentration values logarithmically varying from 20 to 640 mM. Figure 5.4 shows the sedimentation behavior of sensitized nanofibers with HCl concentration values increasing from left to right. Figure 5.4-a shows particles in the sensitizing solution, after the whole sonication cycle was completed. Functionalized CNFs will disperse spontaneously in the $SnCl_2$ solution up to a HCl concentration of 160 mM. Samples 5 and 6 in Figure 5.4 have concentrations of 320 and 640 mM HCl respectively. The nanofibers in these samples could not be dispersed even with sonication times up to 2 hours. Figure 5.4-b shows the sensitized nanofibers 4 hours after 5 cycles of rinsing with 40 mL deionized water and moderate vial agitation to redisperse the filtered particles. Sample 6 in Figure 5.4-b shows more sedimentation than all the other samples. This particular sample also showed numerous visible aggregates which were absent from the other dispersions. The samples were then sonicated for 10 minutes and left untouched for sedimentation assessment. Figure 5.4-c shows the dispersions after settling for 90 hours. The stability of the dispersions increased gradually

from 20 to 320 mM and decreased for the highest concentration. Poor wetting of nanofibers was also noticeable in the latter case where some particles remained preferentially on the air-water interface and adhered to the vial walls.

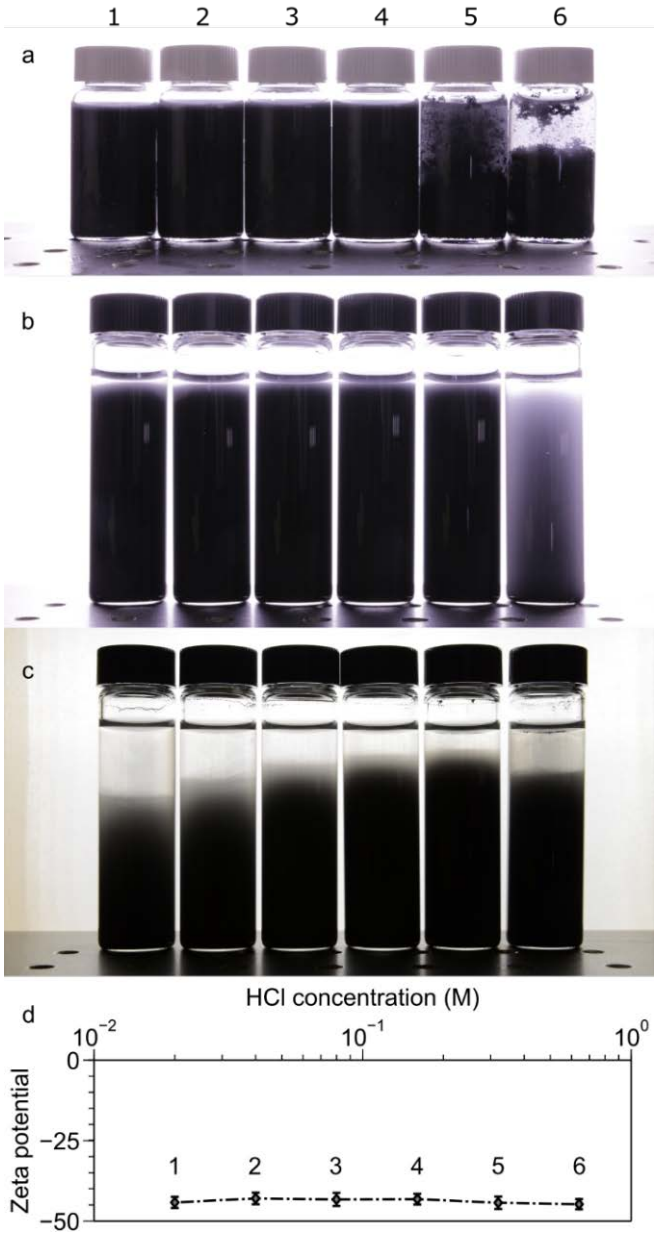

Figure 5.4: Sedimentation behavior and Zeta potential for sensitized CNFs. HCL concentration doubles in each sample, from 20 mM (#1) to 640 mM (#6). a) Particles in the SnCl2 solution at the end of the sonication process. CNFs do not disperse in the 320 and 640 mM solutions. b) Rinsed particles in deionized water. No ultrasonic power was applied for dispersion. The sample with 640 mM HCl does not disperse spontaneously. c) Same as b), with 10 min. ultrasonic agitation and 90 hours sedimentation. The settling time increases with concentration until 320 mM (sample 5). d) Zeta potential of the dispersions in c) diluted to 10 times their volume. No significant variation was measured

The sedimentation speed of the particles is influenced mainly by particle size and density [166]. Incidentally, flocculation will accelerate the settling of the dispersion by forming larger aggregates which are less subjected to the dispersing effects of Brownian motion. Flocculation occurs when the Zeta potential barrier is not high enough to shield particles from their neighbor's attractive van der Walls forces. To assess whether zeta potential differences were responsible for different settling times, we measured the potential on 0.5 mL of each dispersion diluted to 10 mL. The measured values are presented in Figure 5.4 d). Surprisingly, the Zeta potential values were fairly constant over the range of concentrations studied. Another interesting fact lies in the negative value of the potential for neutral pH aqueous media. It was shown that sensitization reduces silver mainly by oxidation of Sn(II) species to Sn(IV) [167]. The simplest scheme for sensitization would then correspond to adsorption of Sn^{2+} ions on the surface of CNFs along with an adsorbed H_2O layer. Upon drying, Sn^{2+} ions would be exposed to oxygen and allowed to be oxidized to Sn^{4+}, with probable formation of SnO_2, which would explain the necessity to keep the surface wet, as Sn(IV) species were shown to be unable to initiate electroless deposition [167]. However, this scheme would result in a positive Zeta potential, which was not observed here. A more detailed scheme was edified by Cohen and West [168] which involves colloid formation around the naturally present Sn^{4+} species by polymerization of $Sn(OH)_4 \cdot nH_2O$. These colloids will in turn bind Sn^{2+} ions for a ratio close to 1 Sn^{2+} ion per 2 Sn^{4+} ions. The authors show convincingly in another publication [169] that it is these colloids that are adsorbed on the surface to be sensitized. The measured Zeta potential would then correspond to the colloids' potential. Further research could confirm whether the Zeta potential of Sn colloids alone correspond to our observations on CNFs.

Further observations support the adsorbed colloids theory. Generally speaking, as particles are left to settle the Zeta potential barrier is overcome and van der Walls forces dominate, making the sediments hard to redisperse. The strategy for preventing sediments formation is the addition of thickeners such as hydroxyethylcellulose [166]. Here, the settled particles are very easily dispersed, supporting the idea that the tin colloids act as a thickener, preventing the particles from coming close enough together for the van der Walls forces to dominate. The difference in settling time must then be attributable to particle size. Since the starting particles underwent identical preparation steps, the additional mass must be added by the tin sensitization. It was shown [168] that the hydrolysis leading to $Sn(OH)_4$ could be inhibited by the presence of Cl^- ions in excess of 500 mM. Without this Sn(IV) complex, the colloids formation cannot occur. In support of this

finding, samples 5 and 6, respectively approaching and crossing the 500 mM threshold, show a dramatic decrease in dispersibility in Figure 5.4-a. Moreover, in subsequent water dispersions, sample 6 does not recover and marks a rupture in the sedimentation behavior trend. This confirms that the sensitization does indeed enter a different regime when Cl^- ions in the sensitization bath cross a concentration threshold somewhere around 500 mM. It was also noted that the solution with the lowest HCl concentration clogged the membrane pores during the filtration process, with dramatically decreased flow through the membrane. This observation is consistent with the model where the colloids are sensitive to pH. High HCl concentration dissolves the outer layers, resulting in smaller colloids [168]. The lowest HCl concentration value therefore allows for larger colloids which block water flow through the filter pores. It is interesting to underline here that the sensitization treatment allows for a remarkable stability of carbon nanoparticle dispersions. This finding alone may facilitate developments based on CNFs or CNTs, since efficient dispersion is a major concern in the field of nanocomposites manufacturing.

To the best of our knowledge, no direct high-resolution images of sensitization deposits were available in the literature prior to our work. Figure 5.5 shows high resolution TEM images of sensitized particles at 60 (Figure 5.5-a) and 160 (Figure 5.5-b) mM HCl concentrations. Compared to the functionalized CNF in Figure 5.2-a and b, we notice that the sensitization yields small spherical particles of 2-3 nm diameter on the surface of the nanofibers. A rough estimate based on Figure 5.5-b shows that the density of tin particles is around 1.5×10^5 particles/μm^2 which is one order of magnitude higher than the value obtained by Feldstein et al. on formvar [170]. Measurement of inter planar spacing on individual particles yielded a value of 3.4 Å, consistent with the [110] direction of the SnO_2 lattice [171, 172]. The lattice dimension is further confirmed by noticing very similar inter planar spacing in tin particle planes and in the underlying graphitic structures. Figure 5.5-a displays bare patches without any tin particles. It is unclear why these patches are more common for the 60 mM HCl concentration sample. However, since particles settle faster at both low and high HCl concentrations and since the 160 mM sample shows better uniformity than that at 60 mM, we chose to proceed with a 160 mM HCl concentration for the investigation of the silvering process parameters.

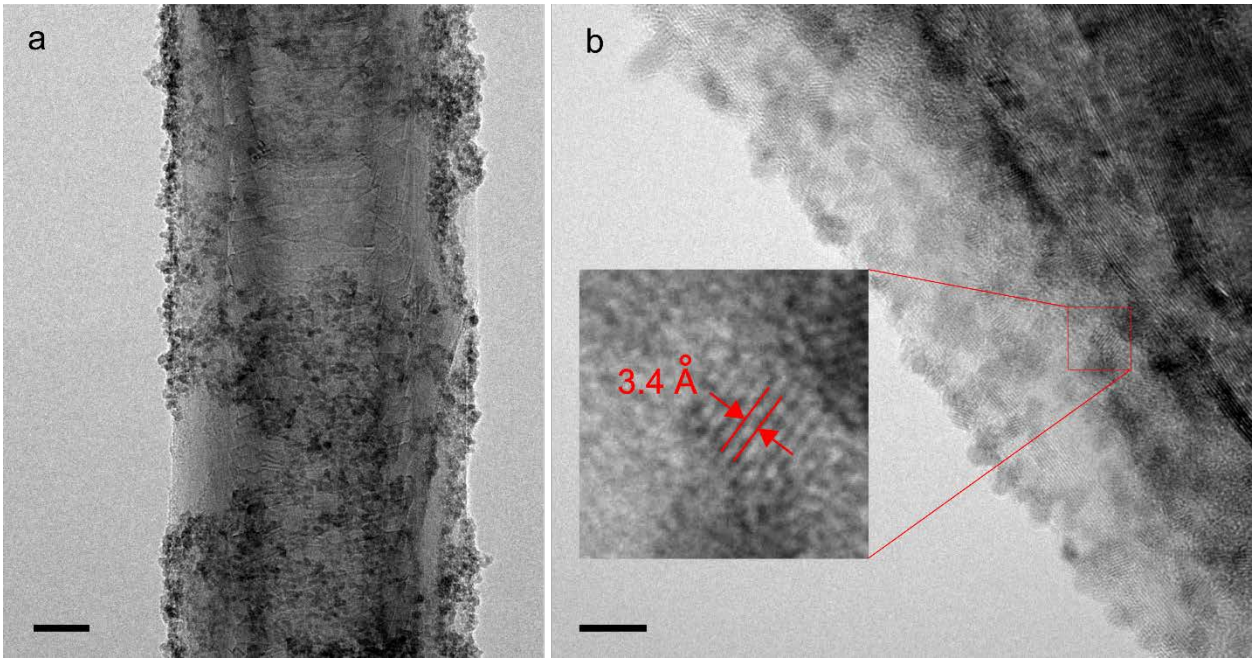

Figure 5.5: Representative TEM images of sensitized CNFs. a) Sensitized with 60 mM HCl. Large patches of tin free carbon are visible (scale bar 20 nm). b) Sensitized with 160 mM HCl solution. The distribution of tin particles is uniform and amounts to roughly 1.5×10^5 particles/μm^2. The inset shows the crystal plane distance of 3.4 Å, which is consistent with SnO_2 (scale bar 5 nm)

We performed XPS analysis on dried sensitized particles. Figure 5.6 shows the spectra of Sn 3d and O 1s peaks on the sensitized sample. As SnO and SnO2 3d5/2 peaks are very close together, the 3d peak by itself is not enough to confirm the oxidation state for Sn(IV). The usual way to proceed in this case is to assess the value of the Auger parameter which is unaffected by surface charge. It is defined as the sum of the kinetic energy of the Sn $M_4N_{45}N_{45}$ peak with the binding energy of the Sn $3d_{5/2}$ peak. In our case, the Auger energy is found at 431.7 eV for an Auger parameter value of 919.2 eV. This indicates that tin is tetravalent in the dried samples. Moreover, the stoichiometry shows a 2.1 at. % ratio between the tin SnO_X and the oxygen Sn-O binding energies, indicating 2 oxygen atoms for every SnO_X detected. We can therefore more confidently state that all tin oxidizes to SnO_2 upon drying. This provides an explanation to the historically known fact that sensitized surfaces must not be allowed to dry before silver deposition [173, 174].

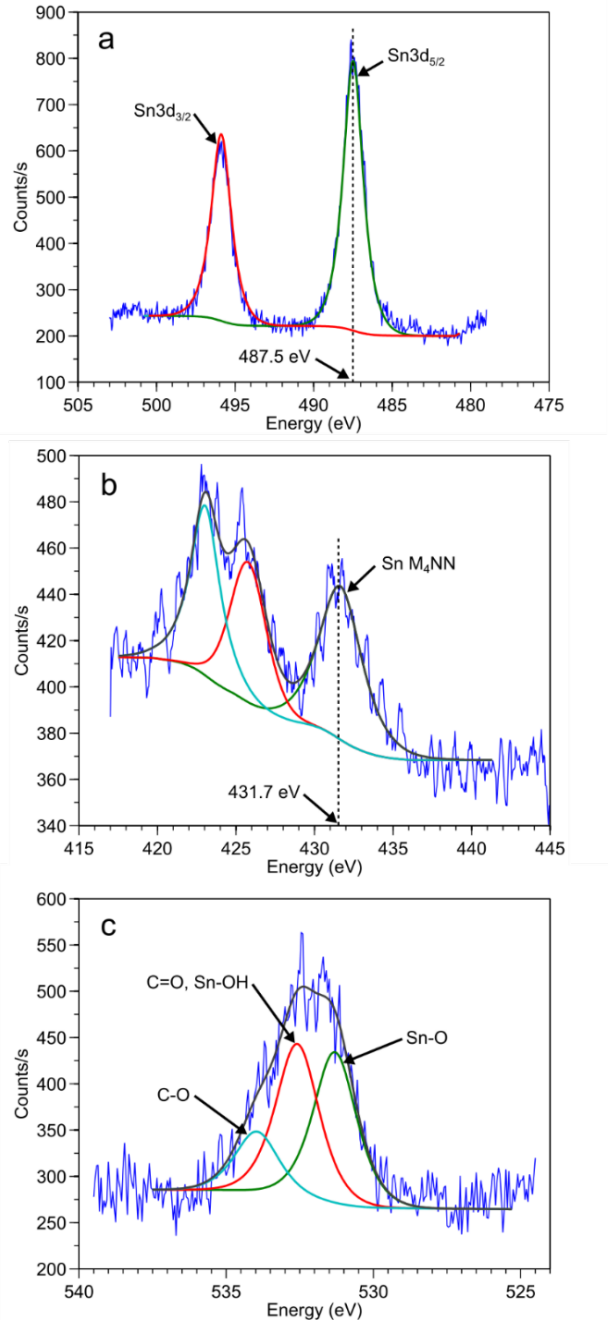

Figure 5.6: High resolution XPS spectra of tin-sensitized CNFs. a) Shows the tin peak with the usual 1.5 ratio between Sn3d3/2 and Sn3d5/2 peak areas. The Sn3d5/2 peak is found at 487.5 eV. b) Sn Auger peaks. The kinetic energy of the Sn M4N45N45 is found at 431.7 eV and adds to the Sn3d5/2 energy for an Auger parameter of 919.2, which indicates that tin is under the Sn(IV) oxidation state. c) Oxygen 1s peak. The Sn-OX stoichiometry further confirms that tin is tetravalent

5.4.3 Silver Deposition

Silver deposition is performed by electroless deposition through diamminesilver ions reduction by the dextrose aldehyde group. Deposition on small structures such as CNFs requires control over the silver particles growth rate. The literature conveys many examples relating a smooth and uniform deposition to a slower deposition rate [144, 175, 176]. However, Boehm *et al*. showed that an optimal surface plasmon resonance signal, which the authors correlate with a good surface smoothness, coincided with the maximum deposition rate, keeping all variables constant except potassium hydroxide content in the diamminesilver solution [146]. They nevertheless found that increasing the plating rate by increasing the temperature was detrimental to the film quality. All aldehydes can reduce silver in the Tollens' scheme. Using dextrose as a reducing agent yielded a lower deposition rate and better results than formaldehyde in terms of coating uniformity and density. We therefore proceeded to investigate dextrose-reduced reactions. The silver solution was prepared fresh for every experiment following the 1:500 [KOH]:[Ag] ratio found optimal for surface plasmon resonance on microscope slides by Boehm *et al.* [146].

We first proceeded to investigate the effect of the amount of Tollens' reagent in solution. Silver solution was added to the samples in increasing volumes. The dispersions were then filtered and extensively rinsed with deionized water, resulting in layers of nanoparticles evenly spread on polycarbonate filter membranes so that sheet conductivity measurements are possible. Since all samples have the same area and starting amount of carbon material, sheet conductivity and mass data points are directly comparable. These values are plotted in Figure 5.7-a. The mass of samples increases linearly with the Ag solution amount. As the total sample mass is in all cases well under the mass of silver in solution, the increasing number of silver ions cannot solely explain the change of mass between samples. Another explanation lies in the increasing deposition rate because of the reaction media getting more alkaline as more ammonia and KOH is added [177]. The sheet conductivity data has a more complex behavior. For a Ag/KOH molar ratio below 0.7, the conductivity increases very slightly, but jumps suddenly by more than one order of magnitude as the molar ratio reaches 0.8. As the weight of samples increases in a nearly linear fashion, the conductivity is not proportional to the samples' weight. This is further confirmed in Figure 5.7-b, where the specific conductivity (sheet conductivity per unit area density) is plotted. Considering a uniform layer of metal, one would expect the specific conductivity to remain constant as more silver is added. However, a sudden increase is observed here as well.

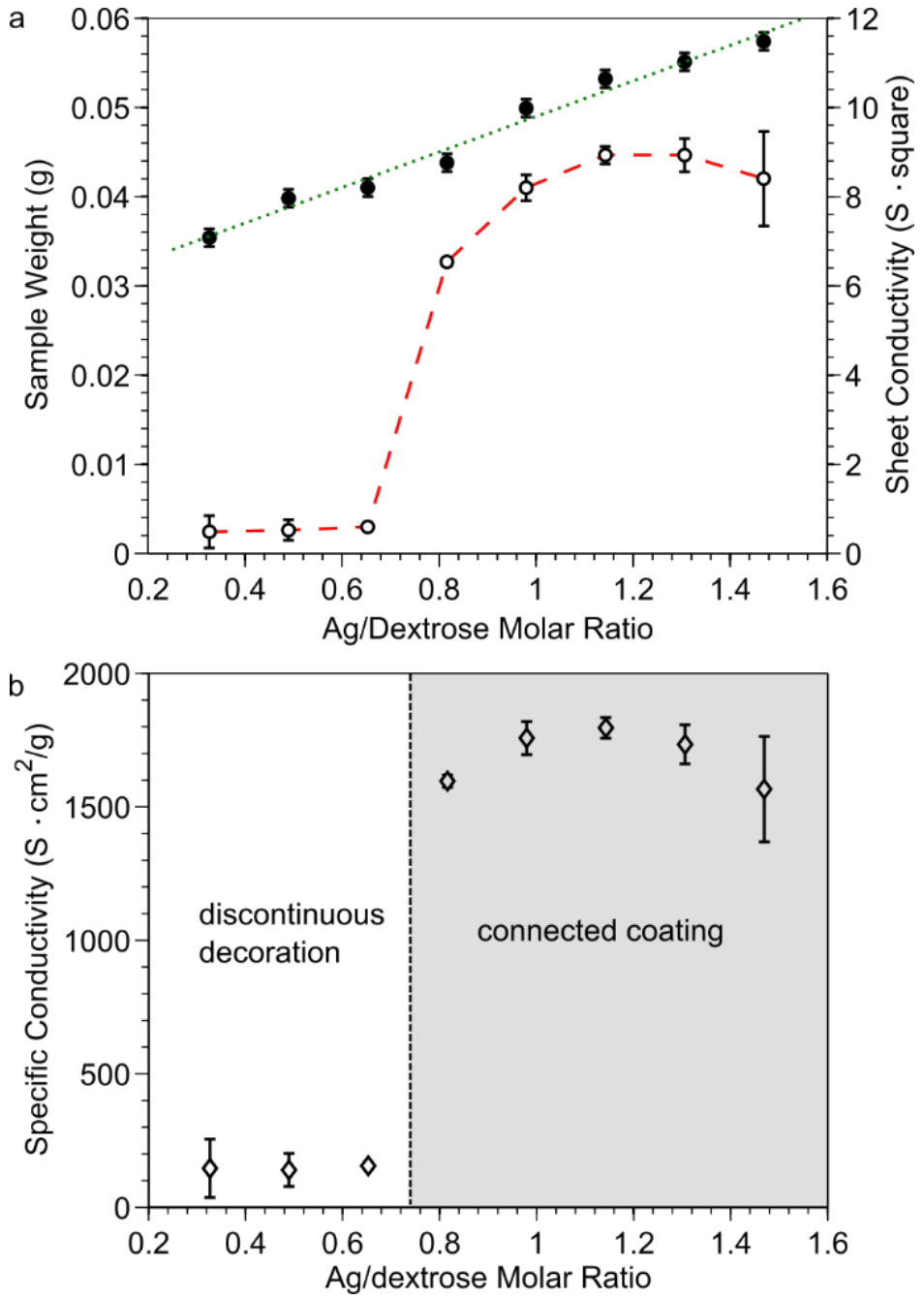

Figure 5.7: Electrical properties of hybrid nanoparticles as a function of silver to dextrose molar ratio. a) A linear trend appears in sample mass (●) while the electrical conductivity (o) undergoes a sudden change at 0.8 molar ratio. b) Specific conductivity (◊) of the samples

The behavior is explained by the morphology of the silver deposits on the different samples. Figure 5.8 shows SEM images of samples with 0.65, 0.81, 1.14 and 1.47 Ag/dextrose molar ratios, corresponding to the samples before and after the sudden jump in conductivity, at maximum

specific conductivity and at highest silver solution volume. The silver deposits for 0.65 molar ratio (Figure 5.8 a and b) exhibit a disconnected morphology with large patches of bare carbon. In this situation, the silver network on the connected 2-d geometry of the carbon particles' surface is not achieved. Therefore, the conduction properties are in large part attributable to the carbon transport properties. Figure 5.8-b shows a magnified view of a large silver cluster. These clusters can be found all over the sample. They are detrimental to the specific conductivity as they do not participate in the network but add a considerable amount of mass to the sample. In strong contrast, at 0.81 molar ratio (Figure 5.8-c and d) silver shows preferential formation on the surface of the nanofibers and no large aggregates are found. Although some carbon is visible through the coating, a fully connected network of silver is deposited on the surface. The sample at 1.14 molar ratio (Figure 5.8-e and f) also shows a fully connected morphology without large aggregates. In this case, however, the visible patches of carbon are fewer, which favors the electrical conductivity by limiting the bottlenecks created by coating inhomogeneities. At 1.47 molar ratio (Figure 5.8-g and h), the sample shows a connected network of silver, but also exhibits the large aggregates discussed before. Overall the coating is not as homogeneous as in the 1.14 molar ratio sample, which means that the mass is used less effectively in transporting charges. Keeping all other parameters constant, only values of 0.8 to 1.5 Ag/dextrose molar ratios will yield coated rather than decorated particles, with an optimal value between 1.0 and 1.3 mL.

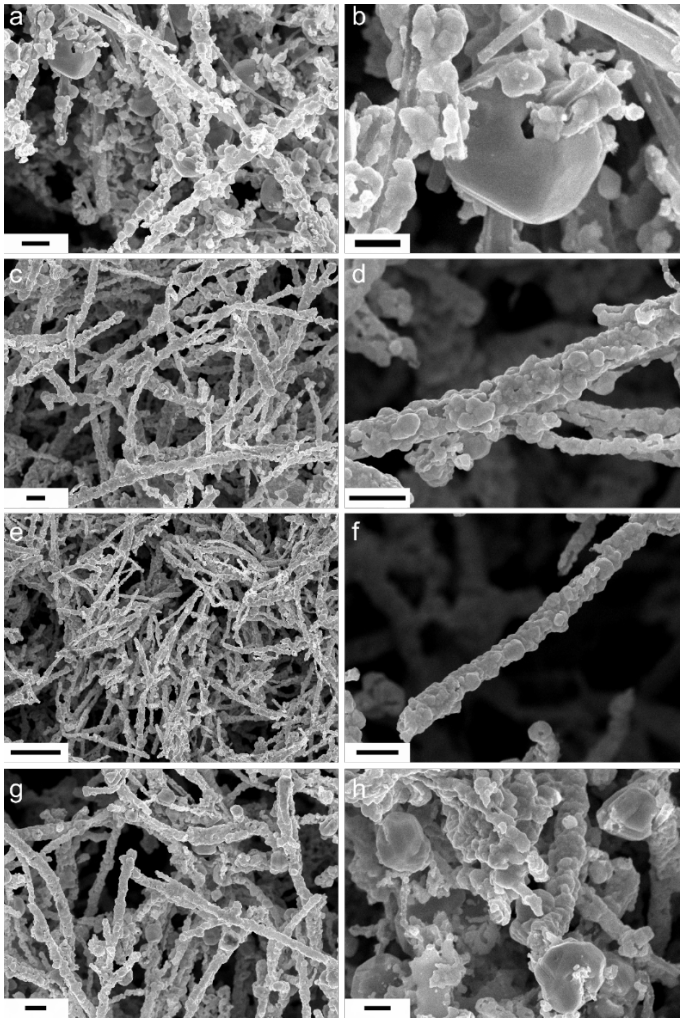

Figure 5.8: SEM images of samples with different Tollens' reagent contents. a) bulk view of sample at molar ratio 0.65. The coating is disconnected, and large isolated silver aggregates are visible (scale bar 1 µm). b) close-up of a large silver crystal at 0.65 molar ratio (scale bar 500 nm). c) Bulk view of sample at molar ratio 0.81. The coating morphology suddenly transitioned from disconnected to mostly connected and uniform. No large aggregates are visible (scale bar 1 µm). d) Close-up of the silver coating at 0.81 molar ratio. Silver deposits are connected but some bare patches are visible (scale bar 1 µm). e) Bulk view of sample at 1.14 molar ratio corresponding to the maximum specific conductivity. All fibers are coated evenly and no large aggregates are visible (scale bar 5 µm). f) Close-up view of sample at 1.14 molar ratio. No bare carbon patches are visible (scale bar 1 µm). g)-h) Sample at 1.47 molar ratio. The coating is uniform, and no bare patches are visible, but large aggregates are visible (scale bars 1 µm and 500 nm, respectively). The coating becomes continuous somewhere around 0.8 molar ratio

We then proceeded to investigate the concentration of reducing agent in solution. The reaction was performed with 3.5 mL Tollens' reagent, corresponding to the maximum specific conductivity in Figure 5.7 (molar ratio 1.14). Filtration and measurements were performed as for the prior investigation. Figure 5.9 shows the variation of weight, conductivity and specific conductivity of the hybrid nanoparticles filtered films. What first stands out is that the samples mass increases at first but starts to decrease after reaching the dextrose/Ag molar ratio of 4. The initial increase in mass can be explained by that the fact that dextrose is the limiting factor in this region, hence not all silver is allowed to react. Indeed, the sample mass reaches a plateau after dextrose and silver reach stoichiometric equilibrium (molar ratio dextrose/Ag of 0.5).

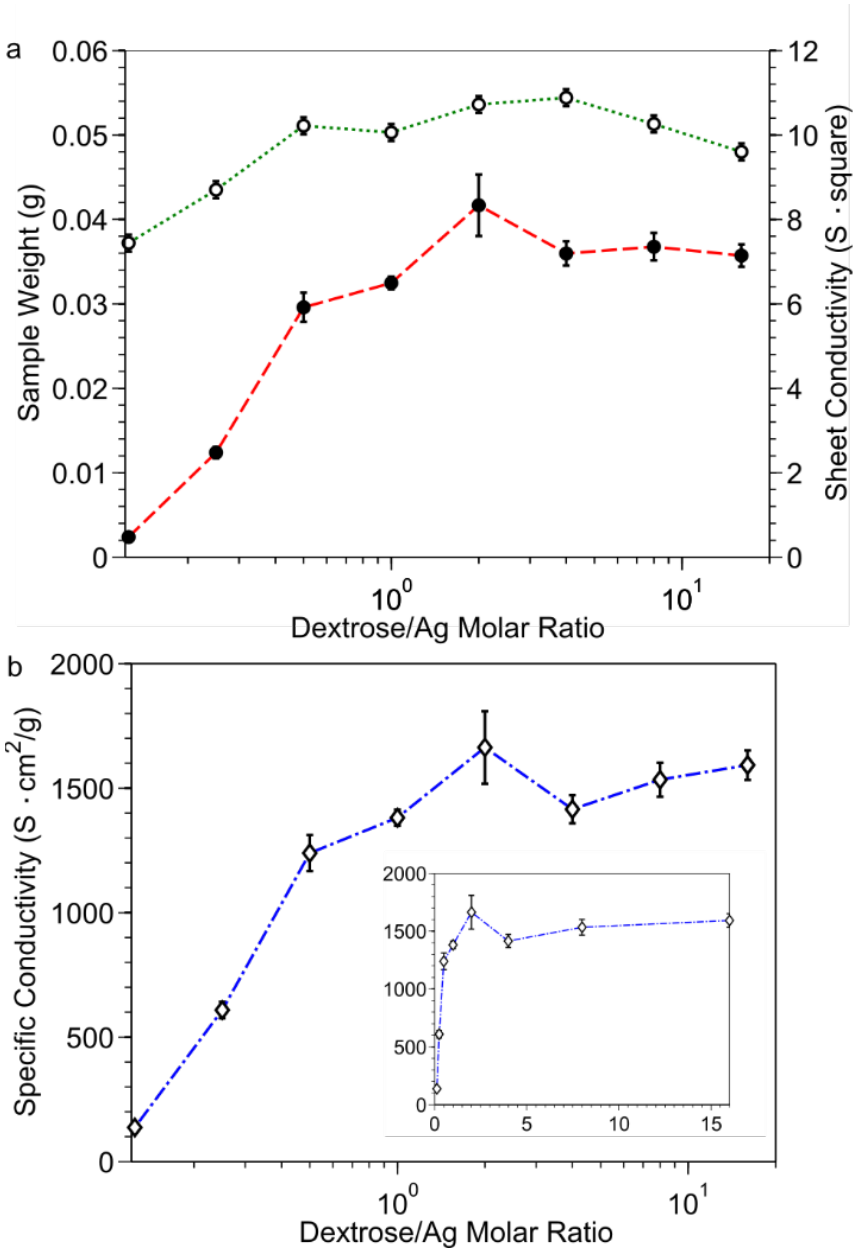

Figure 5.9: Electrical properties with respect to dextrose to silver molar ratio. a) Mass (●)and sheet conductivity (○). The mass of samples stays fairly constant over the 0.5 molar ratio, consistent with a stoichiometric concentration of dextrose. As dextrose is in excess, the sample mass stays constant. b) Specific conductivity (◊). The values remain mostly constant for glucose in excess. The inset provides the same values on a linear scale for comparison with Figure 5.7

Figure 5.10 shows SEM images of samples with various dextrose concentrations. The image on the left is an overview of each sample's appearance while the image on the right provides a close-up on the coating morphology. At 0.25 molar ratio (Figure 5.10-a and b), the metallic silver does not form a uniform layer, but rather deposits in large 100-500 nm islands. Large micron-sized aggregates are also visible which are not present at higher dextrose concentration. This suggests that dextrose as a limiting factor does not simply stop the reaction before a uniform coating is obtained but produces a less controlled reaction resulting in larger crystals and poor coverage. Differences between molar ratios 1 (Figure 5.10-c and d) and 4 (Figure 5.10-e and f) are not significant, with a slightly more uniform coating with more dextrose. Figure 5.9-a shows that the sample mass decreases slightly after a molar ratio of 4, which could be attributable to a slower reaction rate because of a reduced diffusion owing to a higher viscosity. The slight decrease in sample mass is not mirrored by a decrease in conductivity, and no clear trend is observed in the specific conductivity (Figure 5.9-b) for a molar ratio above unity. While adding Tollens' reagent in excess destabilizes the reaction, both Figure 5.9 and Figure 5.10 suggest that adding dextrose up to 32 times the stoichiometric amount is not detrimental to the reaction. The deposition behavior is thus far more sensitive to the amount of Tollens' reagent than it is to dextrose concentration. Furthermore, it was noticed that a high dextrose concentration helped to prevent the aggregation of particles during the electroless deposition process. It is therefore recommended that dextrose be used well in excess of the stoichiometric dextrose/Ag ratio of 0.5.

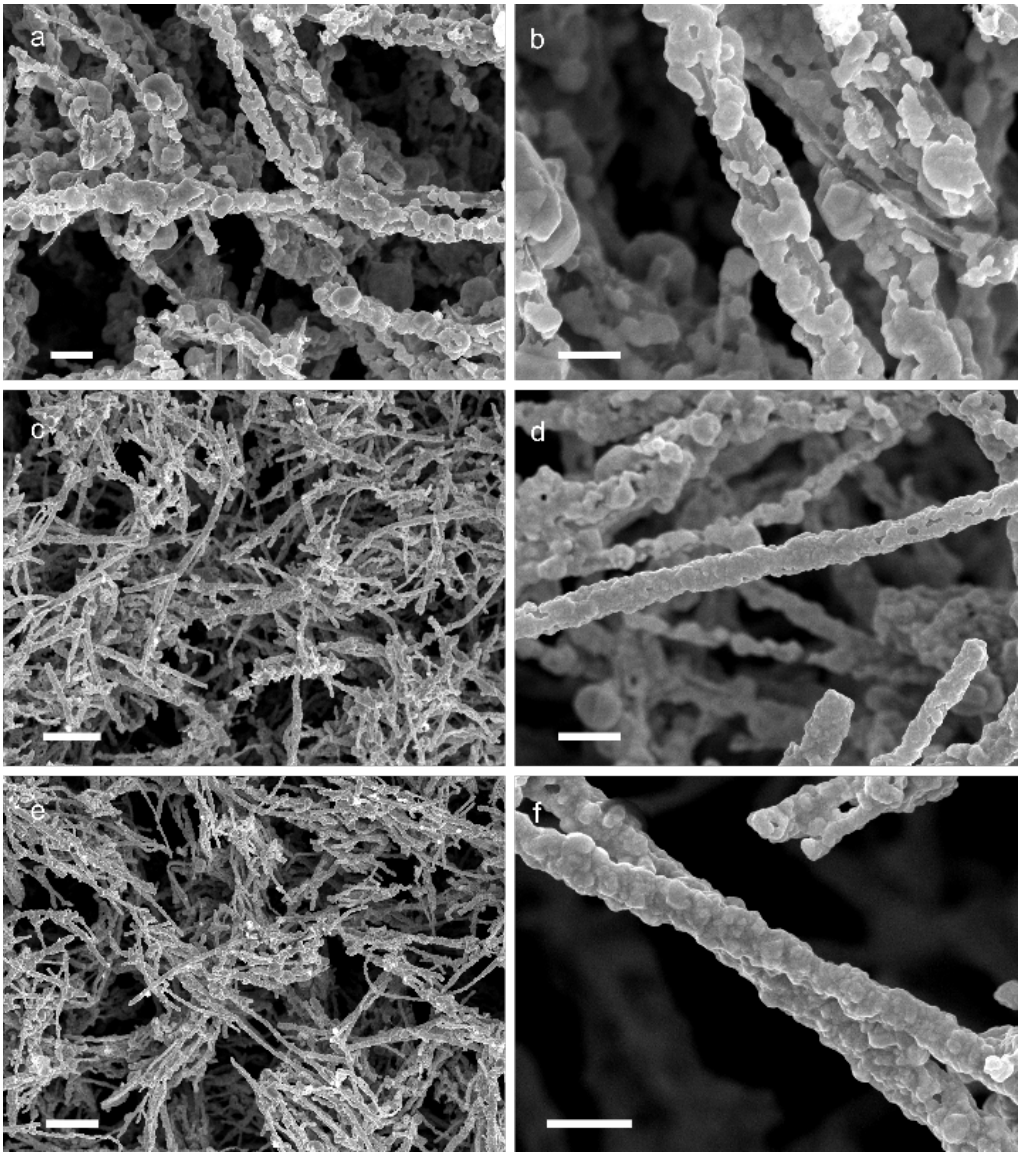

Figure 5.10: SEM images of samples with different dextrose concentrations. a) and b) Sample #2. Silver metal forms in disconnected 100-500 nm thick islands. Scale bars are a) 1 µm and b) 500 nm. c) Bulk view of sample #4. All fibers are coated and the silver is connected. Scale bar is 5 µm. d) close-up view of a fiber from sample 4. Some bare patches of carbon are visible. Scale bar is 1 µm. e) and f) Sample #6. All fibers are uniformly coated. No bare patches are visible. Scale bars are e) 5µm and f) 1 µm

The highest specific conductivity we measured on a 10 cm^2 bulk hybrid silver-CNFs sample was 1800 $S \cdot cm^2/g$ which is only roughly one order of magnitude lower than the specific conductivity of pure silver. The thickness of this film was of 127 µm for a density of 0.4 g/cm^3 (supporting

information, Figure S1), which suggests that an efficient conduction network is achieved at only 4% volume loading since the particles' density can be approximated to that of silver. This finding is of crucial importance, since the loading required for percolation in conductive adhesives is around 20-30%. This exceptionally low volume loading can be explained by the high aspect ratio of the particles which allows for a much more efficient conductivity network. It is thought that the particles undergo oxidation upon drying as some samples went from a yellow to a grey tint. This might explain the difference between the maximum conductivities reached during the investigations of Tollens' reagent amount vs. dextrose amount in solution, as the samples from the latter exhibit a much darker tint (supporting information, Figure S2). It is however unclear why one series of experiment did undergo more oxidation than the other. We believe that it is linked to the rinsing procedure as the samples displayed less oxidation on the periphery of filtered cake. This part of the sample resides under the ridge of the clamped funnel and as such is subject to less water flow during the rinsing step (supporting information, Figure S3). This behavior suggests that protecting the particles with a capping agent such as poly(acrylic acid) might be an easy way to increase the conductivity of the material. As the process is easily scalable to arbitrarily large batches, the technology could replace the silver particles traditionally found in applications such as conductive inks and adhesives. The added value of the technology in this situation is two-fold: cost reduction as less silver metal is required to achieve an excellent conductivity and overall weight reduction which resonates with applications in the aerospace sector.

5.5 Conclusion

We provided a detailed analysis of all the main steps of the electroless silver deposition on CNFs, from the characterization of the starting material through functionalization and tin sensitization until silver deposition itself. We demonstrated that acid functionalization at temperatures lower than 45 °C could efficiently attach carboxylic groups on CNFs without affecting their aspect ratio. We provided new insight into the tin sensitization process that supports a previously published theory on the matter and proposed an optimal HCl concentration for the sensitizing bath. We then provided a range of parameters for which the electroless deposition of silver reliably results in a smooth, continuous and uniform coating on high aspect ratio CNFs. The particles can be used as-produced without the need for time-consuming purification and can be recovered by simple vacuum filtration, thus eliminating the multiple centrifugation steps that plague silver nanowires

fabrication processes. The process is scalable with no noted effect of the vessel size on any step of the process. The resulting bulk particles proved to be efficient in transporting current with a specific electrical conductivity of 1.8 x 10^3 S·cm^2/g, roughly one order of magnitude lower than that of pure silver (6x10^4 S·cm^2/g). The high aspect ratio allows for a more efficient conductivity network, since more contacts are allowed par particle and each particle can transport charges further. Moreover, the packing density of the nanoparticles is of the order of 4%, which indicates that not only are the particles more efficient than packed spherical nanoparticles, but they achieve a robust conduction network at a much lower volume fill ratio, as fillers used in adhesives reach percolation around 20-30 vol%. As such, the hybrid nanofibers are excellent candidates for conductive composites formulation as they offer both a lower weight and a lower cost of silver metal than typical silver flakes. Conductive adhesives and composites for lightning strike protection might therefore benefit from this technology. Since the particles maintain their high aspect ratio, they also exhibit a large surface area and might spark interest as high surface area electrodes. We aimed at providing a study of the deposition process as a whole. Some of its aspects remain unclear, such as the sensitizing dynamics, or the fundamental reasons for the unevenness of the silver deposition under certain conditions. Along with clarification on this subject, optimization work on the pre-treatment steps could be undertaken to alleviate the time required for the manipulations. As our focus was on optimizing the deposition uniformity and the electrical conductivity of the particles, little work was consecrated to the time-wise efficiency of the process, and we believe that dramatic improvements could be achieved. As the technique might be valuable for metallizing a wide array of complex-shaped nanostructures in addition to the carbon nanofibers reported herein, many applications could benefit from additional research on the topic.

5.6 Supporting information

5.6.1 Electroless silver deposition reaction

The widely accepted reaction set for the Tollen's reagent preparation is as follows:

$$2\ AgNO_3 + 2\ KOH \rightarrow Ag_2O + 2\ KNO_3 + H_2O \quad (11)$$

$$4\ NH_3 + Ag_2O + 2\ KNO_3 + H_2O \rightarrow 2\ [Ag(NH_3)_2]NO_3 + 2\ KOH \quad (12)$$

The deposition reaction then proceeds as follows:

$$CH_2OH(CHOH)_4COH + 2\ Ag(NH_3)_2^+ + 2\ OH^-$$

$$\rightarrow 2\ Ag + CH_2OH(CHOH)_4COOH + 4\ NH_3 + H_2O \qquad (13)$$

As is shown in equation (1), the potassium hydroxide is restituted in solution upon dissolution of silver oxide with ammonia. The amount of potassium hydroxide therefore directly influences the concentration of hydroxide ions in the tollen's reagent and thus the reaction dynamics. Equation (3) also shows that at stoichiometric equilibrium there is 1 Mol glucose for 2 Mol silver.

5.6.2 Nanoparticles packing

The measurement of the volume ratio of the nanoparticles provides information about the efficiency of the electrical network within the material. Figure 5.11 shows the cross section of the nanoparticles layer for the highest specific conductivity measured. The 127 µm thickness along with the 5.14×10^{-3} g/cm^2 makes for a 0.4 g/cm^3 density. Approximating the nanofibers to be the same as silver, we obtain a packing density of approximately 4%, which is much lower than the percolation threshold for conventional conductive fillers.

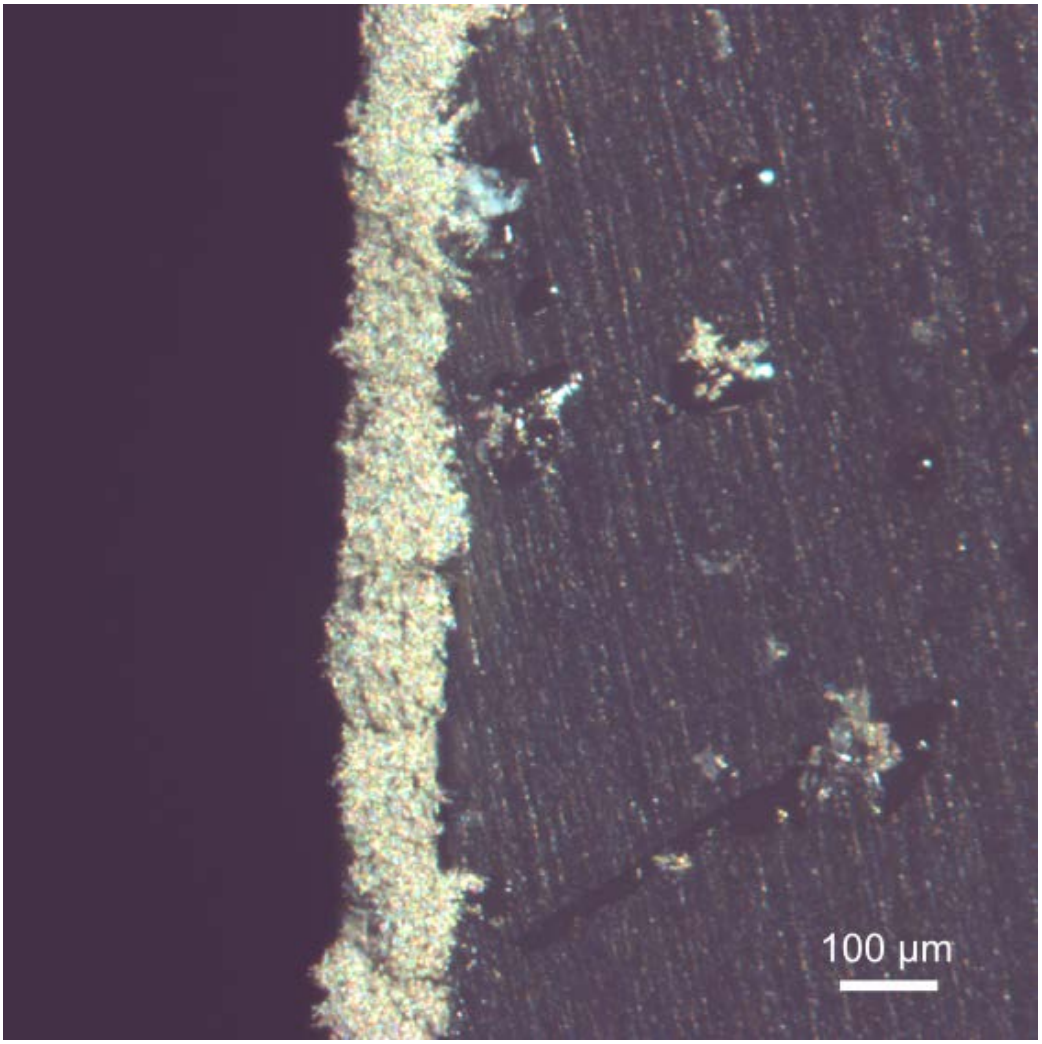

Figure 5.11: Optical microscope image of the cross section of the highest specific conductivity sample with a Ag/dextrose molar ratio of 1.14. The average thickness of the nanoparticle film is 127 µm for a density of 0.4 g/cm^3

5.6.3 Oxidation

The experiments for dextrose concentration and Tollen's reagent amount variation yielded significantly different results in the maximum specific conductivity reached. Moreover, at a dextrose/Ag molar ratio value of 0.88, the dextrose variation curve in Figure 8 (main text) should reach the same value as the maximum of Figure 6 since the solutions are identical. This suggests that the reaction is very sensitive to experimental conditions. Figure 5.12 shows a photograph of samples at nearly identical solutions compositions. The tint difference suggests that the dextrose

variation sample underwent more oxidation, which might explain the lower specific conductivity reached.

Figure 5.13 shows a close-up of the sample periphery. The region that resides under the funnel overhang displays a lighter color which might indicate less oxidation. Since this region is protected from the water flow during the rinsing operation, we believe that residues from the electroless deposition solution protect the particles from oxidation.

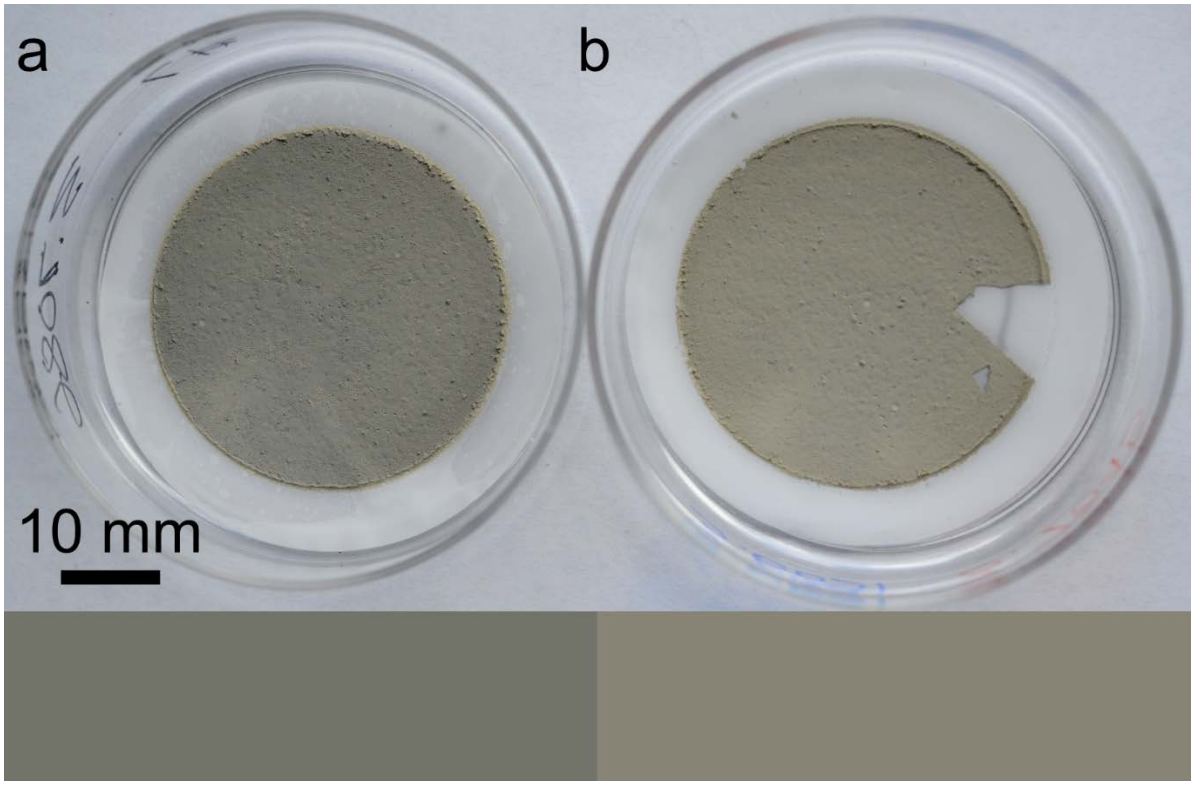

Figure 5.12: A photograph of samples produced during experiments on a) dextrose concentration variation and b) Tollen's reagent amount variation. The color bars show the average color picked on the samples images

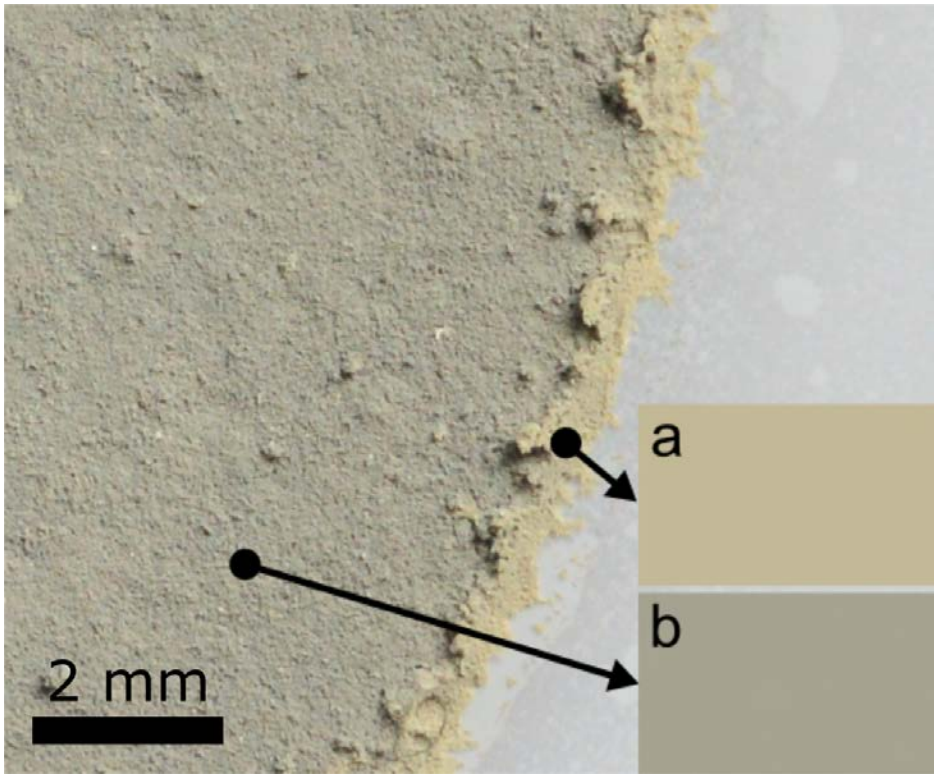

Figure 5.13: The edge o nanoparticles after drying. The region under the ridge of the funnel (a) shows a lighter color than the bulk of the sample (b)

CHAPTER 6 ARTICLE 3: HYBRID CARBON-SILVER NANOFILLERS FOR COMPOSITE COATINGS WITH NEAR METALLIC ELECTRICAL CONDUCTIVITY

Xavier Cauchy, Jolanta-Ewa Klemberg-Sapieha and Daniel Therriault*

Laboratory for Multi-Scale Mechanics, École Polytechnique de Montréal, P.O. Box 6079, Station Downtown, Montreal (QC), H3C 3A7, Canada

Small, 9th of May, 2018.

6.1 Abstract

Polymeric composite materials are now very well established in all areas of engineering and are still increasingly being used to replace metallic counterparts. As an important advantage, composite materials hold the promise of multifunctionality, that is fine tuning the material composition to synthetically achieve specific requirements. Among these requirements, the electrical conductivity is still limited to values orders of magnitude below those of typical metals. We herein present an approach to conductive fillers which involves taking advantage of the favorable properties of both carbonaceous and metallic fillers to provide near metallic conductivity to the surface of carbon fiber reinforced polymer composites. We achieved the synthesis of hybrid core-shell high aspect ratio carbon-silver nanoparticles with a continuous silver coating, which allows both a low contact resistance between individual fillers and a greater connectivity owing to the wire-like morphology of the particles. Incorporating the nanoparticles in an epoxy matrix yields a conductivity of 2.5×10^5 S/m at a loading of 6.3 vol. % for a corresponding material density of 1.9 g/cm^3. The conductivity reached is high enough even to divert emulated lightning strike energy.

6.2 Introduction

The important recent developments in nanosynthesis and the related properties of nanomaterials drive the search for applications in multifunctional polymeric composite materials. Among the desired added functionalities, a high electrical conductivity still evades researchers since the insulating nature of most matrix systems prevents the electrical current from travelling from one filler particle to the other. The inclusion of conductive fillers in the matrix has been thoroughly

investigated in the recent decades with much effort concentrated on carbon nanotubes (CNTs) [5, 7, 68, 71, 133] because of the high conductivity of individual particles [48] and low percolation threshold [7], owing to their high aspect ratio. Other fillers include metallic nanowires [121, 178], metallic nanoparticles [99], indium tin oxide nanoparticles [98], reduced graphene oxide [179] or a combination of different fillers [113]. A high aspect ratio and low contact resistance are desirable properties of nanoparticles for electrical conductivity applications. Here, we show the feasibility of using controlled electroless silver deposition on high aspect ratio carbon nanofibers (CNFs) to yield highly conductive hybrid cylindrical nanofillers with a carbon core and a metallic surface. We then demonstrate a moderate scale application of the technology for lightning strike protection of carbon fiber reinforced plastics (CFRP) by embedding a layer of hybrid nanoparticles on the surface of a 30 cm by 30 cm CFRP panel. The silver deposition was performed in an aqueous solution and is based on the well-known Tollens' test for aldehydes. The process successfully resulted in uniform coating of individual CNFs throughout the sample with an inexpensive pre-treatment. The loose nanoparticle deposits exhibit an electrical conductivity per unit mass lower than that of pure silver by approximately one order of magnitude, whereas the conductivity of various nanoparticles was reported to reach only 0.1-1% of the bulk value upon compaction [99]. CFRP protective coatings were fabricated by transferring the nanoparticle films obtained by vacuum filtration of the dispersed nanoparticles directly to commercial B-staged epoxy films, thus making the process easily scalable. The films were then bonded to CFRP panels and submitted to simulated lightning strikes. The comparison with unprotected panels showed convincingly how a small amount of nanoparticles is able to efficiently divert lightning strike energy from the body of the panels. Many more applications are foreseen where lightweight, flexibility and nearly metallic conductivity is required.

Historically, the addition of conductive fillers to polymers was shown to be successful in providing electrical properties to the material. CNTs were used to provide electromagnetic interference (EMI) shielding capabilities at relatively low mass fraction [117, 180], achieved remarkably low percolation thresholds [7, 68, 71], defined as the lowest concentration where the electrical conduction network is established within the material. However, the typical electrical conductivity obtained at percolation threshold is of the order of 10^{-3}-10^{-1} S/m [68, 69, 116, 120], which is 8 orders of magnitude lower than typical metallic-like conductivity (~10^{7} S/m). Pure, dense films of CNTs can be fabricated but generally require post-treatments such as doping and cross-linking to

display conductivities in the 10^5 S/m range [63]. The limited performances of CNT conductive networks are attributed to the contact resistance between individual particles [135, 181] and tunneling resistance in the composite [133]. Graphene nanocomposites have similarly low percolation thresholds [182], but still struggle to achieve high conductivities, with the highest achieved so far remaining at 3000 S/m [97]. Graphene has the additional disadvantage of losing its electrical properties upon oxygen functionalization through the Hummer's method and its derivatives. Restoring the electrical properties requires aggressive reduction methods [90, 97].

Therefore, silver metal fillers are still the solution for achieving conductivity values of 10^5 S/m and higher in applications such as isotropic conductive adhesives [138]. It was shown that the conductivity of a silver nanoparticle network can be enhanced by sintering at temperatures far below the melting point [136] or under pressure [99] and that exposing Ag nanowires to broadband visible light could induce welding by localized heating [137]. Metallic fillers typically have high percolation thresholds because of their low aspect ratio whereas metallic nanowires remain prohibitively priced for large-scale applications because of the relatively low yield associated with the polyol process [139-141]. Hybrid particles combining the high aspect ratio of CNTs or CNFs and the aforementioned properties of silver nanoparticles are therefore promising candidates for high conductivity applications.

Electroless deposition of silver has been used thoroughly in the last century to produce mirrors [142, 143]. Lately, the topic has been revived by the scientific interest in microstructures and nanoparticles where geometry forbids other processes. Electroless deposition was shown to be an efficient process for uniform metallic coating on microstructures [144, 145], fabrication of surface-enhanced Raman scattering substrates [147, 148, 183] and surface plasmon resonance sensors [146]. Silver plating of graphite powders was shown to increase conductivity in conductive adhesives by up to 2 orders of magnitude [149, 150]. Deposition on carbonaceous nanoparticles was attempted with varying success. An uniform coating was obtained on carbon spheres [151, 152], but deposition on nanotubes produced mere decoration [113, 153], discontinuous coatings [154-157] or loss of aspect ratio [158, 159]. We sought to fabricate carbon nanofiber based silver coated hybrid nanoparticles that would combine 1) a continuous and uniform coating, 2) a consistent coating over the bulk of the sample and 3) the preservation of a high aspect ratio.

6.3 Results and Discussion

CNFs are highly similar to CNTs in surface chemistry and shape [158], but were preferred to nanotubes because of their larger mean diameter (~100 nm) which remains the dominant dimension under initial Ag nanoparticle deposition (see Figure 6.1c and Figure 6.7). Here, the silver-coated carbon nanofibers (Ag-CNFs) were fabricated by adapting the Brashear and Crossley mirroring processes [143] to suspended particles. Figure 6.1 shows the deposition process at different stages. First, pristine vapor-grown carbon nanofibers were acid functionalized with a 1:3 mixture of $AgNO_3$ and H_2SO_4 in an ultrasonic bath. The acid mixture was kept at a temperature below 60 °C to preserve the particles' integrity [78]. X-ray photoelectron spectroscopy (XPS) measurements on functionalized particles showed an oxygen concentration of 11 at. %, compared to an all carbon signal for pristine nanofibers.

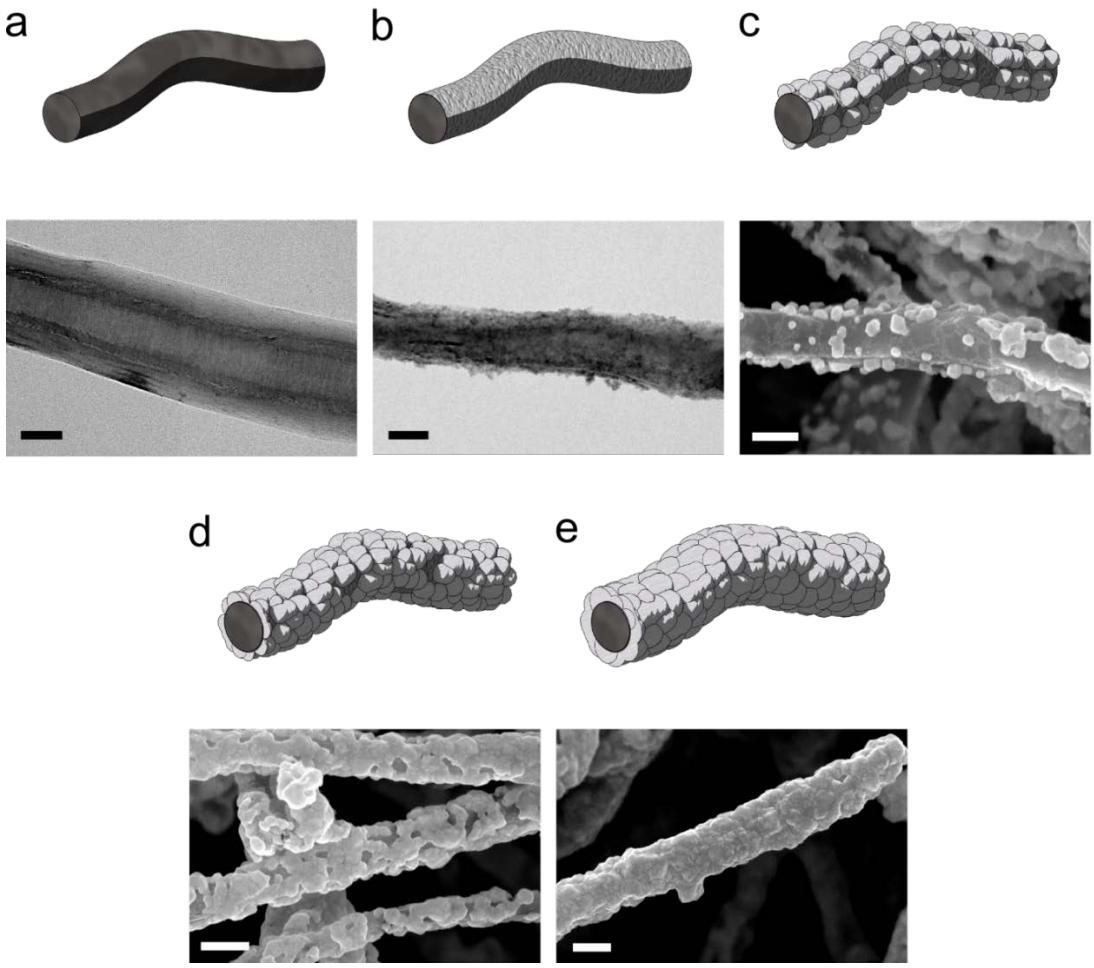

Figure 6.1: Steps in the Ag deposition process. The top images are conceptual representations of the CNF status at each step. a) Pristine CNF as imaged with TEM. The CNFs consist of a stacked cones graphitic structure core and a concentric cylindrical structured exterior surface (scale bar 20 nm). b) Sn covered CNF. Small nanocrystals 3-5 nm in size cover the whole surface of the CNF. The core structure is shadowed (scale bar 100 nm). c) Initial Ag deposits after 70 seconds reaction time. Small Ag nanoparticles are initiated on the surface of the CNF. Most of the carbon is still exposed. The thickness of the deposits is approximately 50 nm (scale bar 200 nm). d) Percolation of the Ag deposits after 170 seconds. An interconnected Ag islands path starts to develop along most CNFs. Deposits thickness is still approximately 50 nm (scale bar 300 nm). e) After 580 seconds deposition. The whole CNF surface is covered with silver (scale bar 300 nm)

The next step in the deposition process is referred to as the sensitization step (Figure 6.1-b). A thin layer of Sn is deposited on the surface of the CNF by immersing the particles in an acidic tin

solution. Parameters influencing the Sn layer quality include $SnCl_2$ concentration, HCl concentration, solution aging time, addition of $SnCl_4$ and solution temperature [165, 167, 170, 184], The nanoparticles dispersion was sonicated for 45 minutes, left to dwell for 90 minutes and sonicated for 45 more minutes, keeping the temperature under 45 °C before thorough rinsing. Initial silver seeding mimics the adsorbed Sn^{2+} coating by the reduction of Ag^{+} by Sn^{2+} [152, 167], Therefore, a uniform layer of tin is crucial to the subsequent Ag film uniformity. In Figure 6.1-b and Figure 6.2, the TEM images of sensitized CNFs reveal that most of the CNFs' surface is covered with a very thin and uniform layer of tin nanoparticles. Figure 6.2-b shows that the individual Sn nanoparticles' diameters range from 3 to 5 nm through measurement of regions displaying uniform orientation of crystal planes.

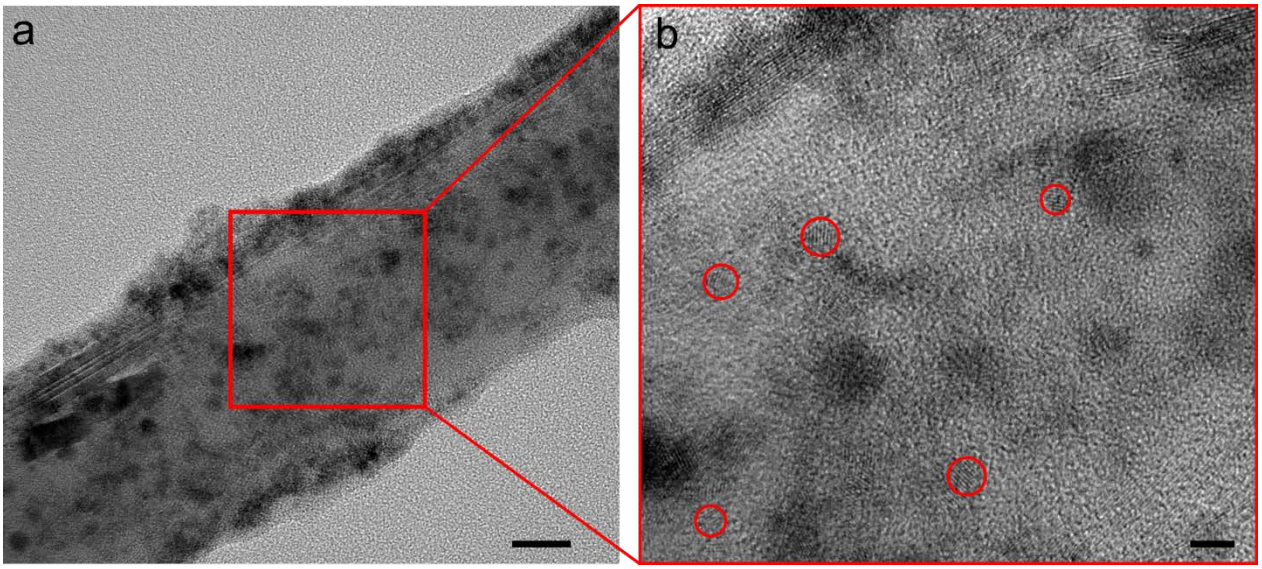

Figure 6.2: Detailed view of a representative Sn layer. a) Overall TEM view of the side of a CNF after Sn sensitization treatment. Most of the CNF structure is shadowed by Sn deposits. Some areas remain where the graphitic planes of the CNF can be seen (scale bar 20 nm). b) Close up of the same CNF. The imaged zone is framed in red in a). The size of individual crystals can be estimated by measuring the diameter of zones exhibiting parallel planes (red circles). Sizes are 3-5 nm (scale bar 5 nm)

After rinsing, the sensitized CNFs were dispersed in 175 ml water and were added to the reducing solution (solution A). The complexed Ag solution (solution B) was then added to the dispersion and the mixture was agitated in a closed vessel while the reaction proceeded. The glass reaction vessel acquires a yellow transparent tint which slowly turns to a brownish red in the first minutes

of reaction, which is indicative of Ag nanoparticles formation and growth. After 10 minutes, the glass become fully opaque and reflective (Figure 6.8). The reaction rate was investigated by removing 40 ml of the homogeneous solution at different reaction times. The removed solution was immediately filtered and rinsed with 200 ml DI water. The resulting nanoparticle films were dried under vacuum overnight and weighed. Figure 6.3-a shows the weight of the samples with reaction time. We assumed a depletion-type time dependence of the reaction rate for silver deposition yielding time dependence in the form of the equation:

$$m = A + B(1 - e^{-\lambda t}) \tag{14}$$

for the mass m of individual samples, where A, B and λ are variables to be fitted (further explanations in supporting information). The model was fitted to the experimental data points and plotted in Figure 6.3-a. Deriving Equation (1) yields the deposition rate for the total sample surface. Adjusting for the manufacturer claimed 24 m^2/g surface area of the CNFs yields the deposition rate per unit area. The maximum and average deposition rates were found to be 1.2 mg/m^2s and 0.48 mg/m^2s respectively, which is consistent with the reported 1.7 mg/m^2s value found for deposition on nanotubes by Feng and Yuan. This supports with the authors' observation that a lower value favors a uniform deposition [176].

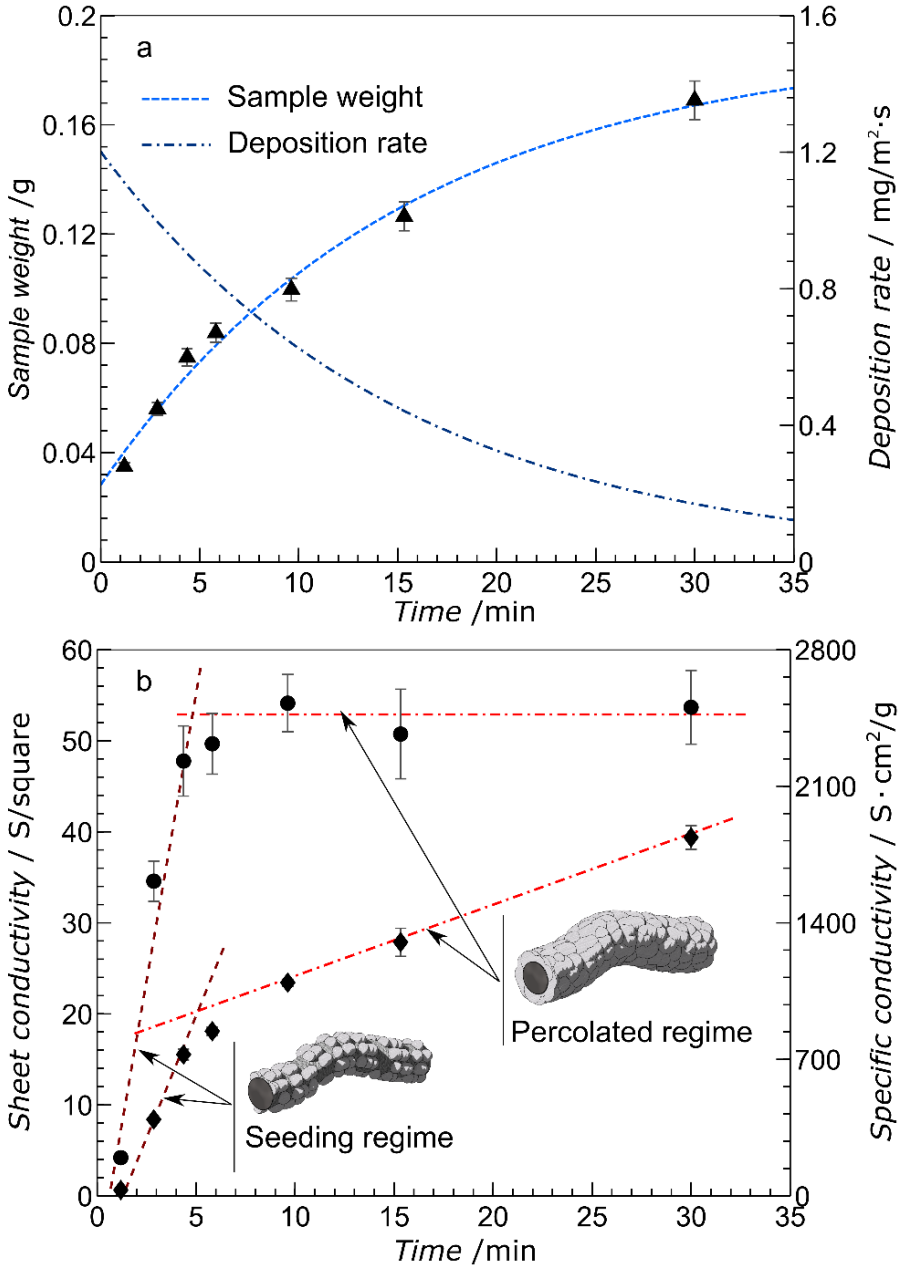

Figure 6.3: Ag coating evolution during time. a) Sample weight evolution during deposition time. Error bars represent the standard deviation of a set of volume measurements performed with the equipment used in the experiment. A good fit is obtained with the behaviour postulated in equation (1). The deposition rate evolution is computed from the fit. b) Electrical conductivity (♦) and specific conductivity (●) of samples. The error bars on the conductivity values represent the standard deviation on the set of 15 measurements performed on each sample. The conductivity evolution suggests two different regimes which are confirmed by the specific conductivity behaviour

To take advantage of silver's high conductivity, a continuously connected network of particles is desirable. As it can be seen from the progression of the deposited layer in Figure 6.1, Ag does not immediately form a continuous layer, but rather deposits in nanoparticles approximately 50 nm in diameter on the CNF surface. SEM images (Figure 6.1-c, d, e) indicate that the voids in the coating are filled by formation of new seeds rather than lateral growth of existing seeds, as distance between individual seeds is reduced by a greater amount than the increase in Ag island thickness.

In this respect, the formation of a connected network on the 2-dimensional surface of CNFs is comparable to a percolation mechanism. As deposition proceeds, the concentration of conductive metal seeds on the surface increases until the onset of a conductive network. For the analogy to be complete, one is to expect a sharp increase in the electrical conductivity of the material as percolation occurs. Figure 6.3-b shows the electrical conductivity of the hybrid particles films obtained as described previously. The first five minutes of deposition give rise to a sharp increase in conductivity of ~3.2 S/(square·min.). During minutes 5 to 10, the increase in conductivity slows down until it reaches approximately 1.5 S/(square·min.). Also shown in Figure 6.3-b is the specific conductivity, defined as the sheet conductivity divided by the areal density, which reflects the ability to transport current per unit mass. Specific conductivity is a constant for a given material. Left aside thin film effects, we are therefore to expect near-constant specific conductivity upon complete coverage of the whole sample as the fractional mass of C in the sample becomes negligible. Consistently with the conductivity behavior, the specific conductivity rises during the seeding phase of the deposition process, slows down after 5 minutes and reaches a plateau after 10 minutes as was predicted upon reaching a continuous coating. Maximum conductivity can therefore be achieved only with uniform coating. The maximum measured specific conductivity is comparable to that of pure silver as it reaches 4.2% of its value, which is more than the maximum value for packed nanoparticles found by Untereker et al. [99]. Noticeably, no compaction pressure was applied to the particles in our experiment. Figure 6.4 shows SEM images of the detail of a particle and of the bulk of a sample. The images clearly underline that all three desired criteria listed earlier were met.

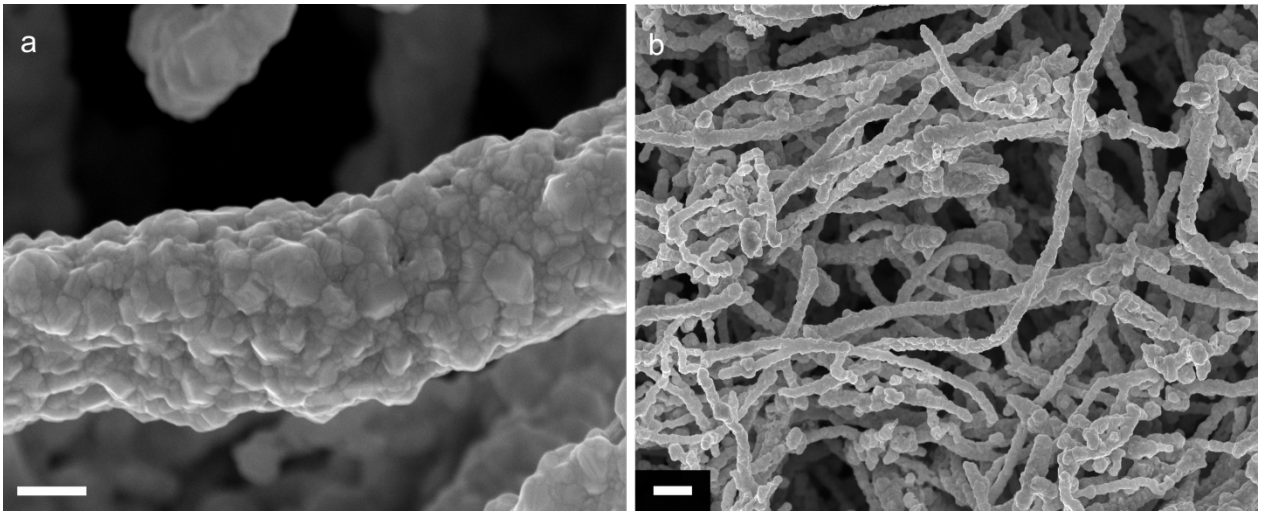

Figure 6.4: Ag-CNFs morphology. a) Close-up view of an Ag-CNF after 30 min deposition. Tightly packed individual crystallites are visible (scale bar =300 nm). b) View of bulk Ag-CNFs after 15 min deposition. The individual particles maintained a length of the order of 10 μm (scale bar = 1 μm)

Among possible applications for highly conductive polymer composites, lightning strike protection is perhaps the most demanding. This application calls for the highest possible conductivity, so we sought a high filler fraction for the CFRP panels coating. We therefore chose to proceed in a two-step fashion, illustrated in Figure 6.5, which is inspired from vacuum assisted infusion of carbon fibers. First, Ag coated hybrid nanoparticles were prepared with a 12 minutes reaction time. The particles were filtered out of the reaction vessel and rinsed with copious amounts of water. Particles were then dispersed in 500 ml H_2O and a film was obtained through vacuum filtration with a custom-made square filtration apparatus of 257 mm side dimension equipped with a polycarbonate filter membrane (Figure 6.5-a,b). The polycarbonate membrane was then carefully removed from the filter apparatus along with the filtered cake, and the particles were left to dry (Figure 6.5-c). The dried nanoparticles mat did not display any void or cracking due to solvent withdrawal.

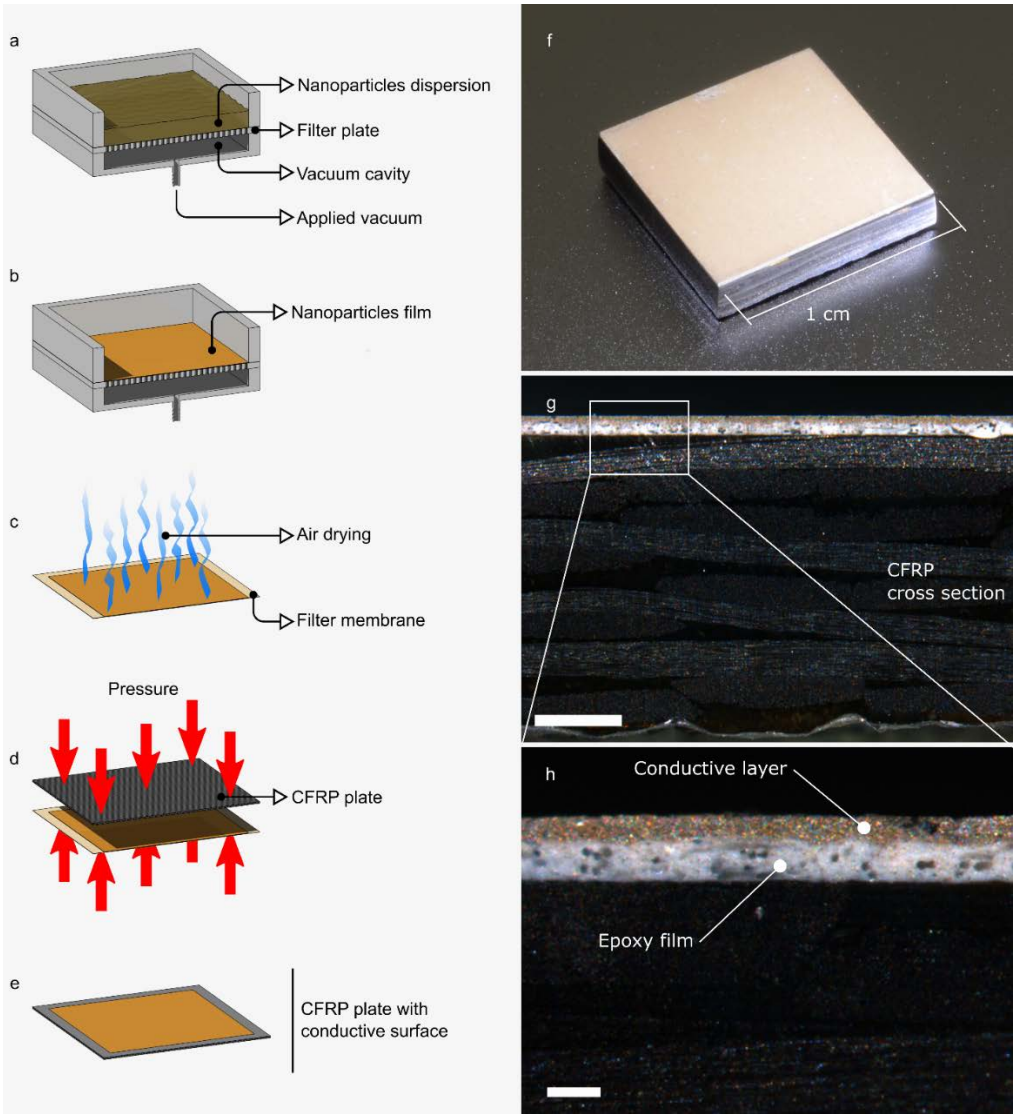

Figure 6.5: Coating fabrication process schematic. a) The nanoparticles dispersion is poured in the filter apparatus. b) After vacuum is applied, particles form a uniform layer on the filter membrane. c) The filter membrane is removed from the apparatus and left to dry. d) The filter membrane bearing the dried particles is pressed against a b-staged epoxy film fitted on a CFRP plate. The particles are transferred to the epoxy film. e) After vacuum assisted resin infusion and curing at 150 °C, the nanoparticles are embedded on the CFRP plate surface. f) Photograph of a cut-out from a panel prepared as described above. The sample thickness is 1.8 mm. g) Cross-sectional view of the same sample as in f) showing the conductive layer compared to the panel thickness. The hybrid nanofiber layer shows in a yellowish silver color (Scale bar = 500 µm). g) A close-up of the cross section that was used to measure the nanofibers-filled region thickness. The gray region is the surfacing film without conductive fillers (Scale bar = 100µm)

During the Ag-CNF drying step, a commercial B-staged surfacing epoxy film was added to the surface of a CFRP plate. The dried nanoparticle films were then transferred to the epoxy film by sandwiching the nanoparticle layer between the polycarbonate filter membrane and the epoxy film. Since the Ag-CNFs do not adhere to the filter but do adhere to the high-tack epoxy film, the continuous nanoparticle layer can be easily transferred to the resin film (Figure 6.5-d). The CFRP plate was placed conductive face down against an aluminium tool and wrapped in vacuum bagging. The sample was then cured under vacuum, suddenly bringing the tool to the highest allowed curing temperature in order to lower the epoxy viscosity. Figure 6.5-f shows a photograph of a piece of sample obtained by this method. Figure 6.5-g and h show the cross section of the same sample. As the thickness of the film remains unchanged, we know that the entire nanoparticle layer is infused with epoxy. The surface of the sample is then expected to exhibit properties very close to that of the cured surfacing film. It was not prone to scratching or delamination. Moreover, since the epoxy film used is meant for use with aerospace composites, the properties of the underlying laminate are not expected to change. The areal weight of hybrid nanoparticles was measured at 2.8 mg/cm^2 and the sheet conductivity was 10.7 S·square for a specific conductivity of 3820 S·cm^2/g, which is more than 50% higher than the as-filtered particles. Extracting the mean value from multiple thickness measurements on Figure 6.5-h) yields a value of 43 µm, which allows for the calculation of the composite volume conductivity, found to be of 2.5×10^5 S/m, comparable to the value obtained with Ag nanoparticles at a loading of 60 vol. % [99]. In contrast, our loading is 10 times lower at 6.3 vol. % as computed from the density value. This finding opens up exciting perspectives for new, low cost, formulations of isotropic conductive adhesives and new lightning strike protection systems.

We tested the latter by subjecting CFRP panels with hybrid nanofiber coating of areal density of 2.8 mg/cm^2 to simulated lightning strikes. Figure 6.6-a shows the current waveform recorded during the simulated strike. The waveform emulates the double exponential function prescribed in aerospace standards [19] and while the peak current doesn't reach the 200 kA value required for severe lightning events, the 15 kA peak current value does cover the lesser 35% of lightning strikes to ground [185], which are known to be more severe and less frequent than intracloud strikes to aircraft [19]. Figure 6.6-b and c show the surface of the nanoparticles protected panel after being subjected to the current waveform depicted in Figure 6.6-a. Although the coating has been burned away on a circular region of approximately 2.3 cm^2, there is no apparent damage to the underlying

composite. In sharp contrast, Figure 6.6-d shows an unprotected panel exposed to the same simulated strike which displays lifted plies and vaporized resin. Confirming the visual inspection, Figure 6.6-e and f show ultrasonic C-scans performed on the samples. Damage to the plies is detected on the unprotected panel along with slight swelling of the region surrounding the attachment point. No damage is detected within the nanoparticle protected sample.

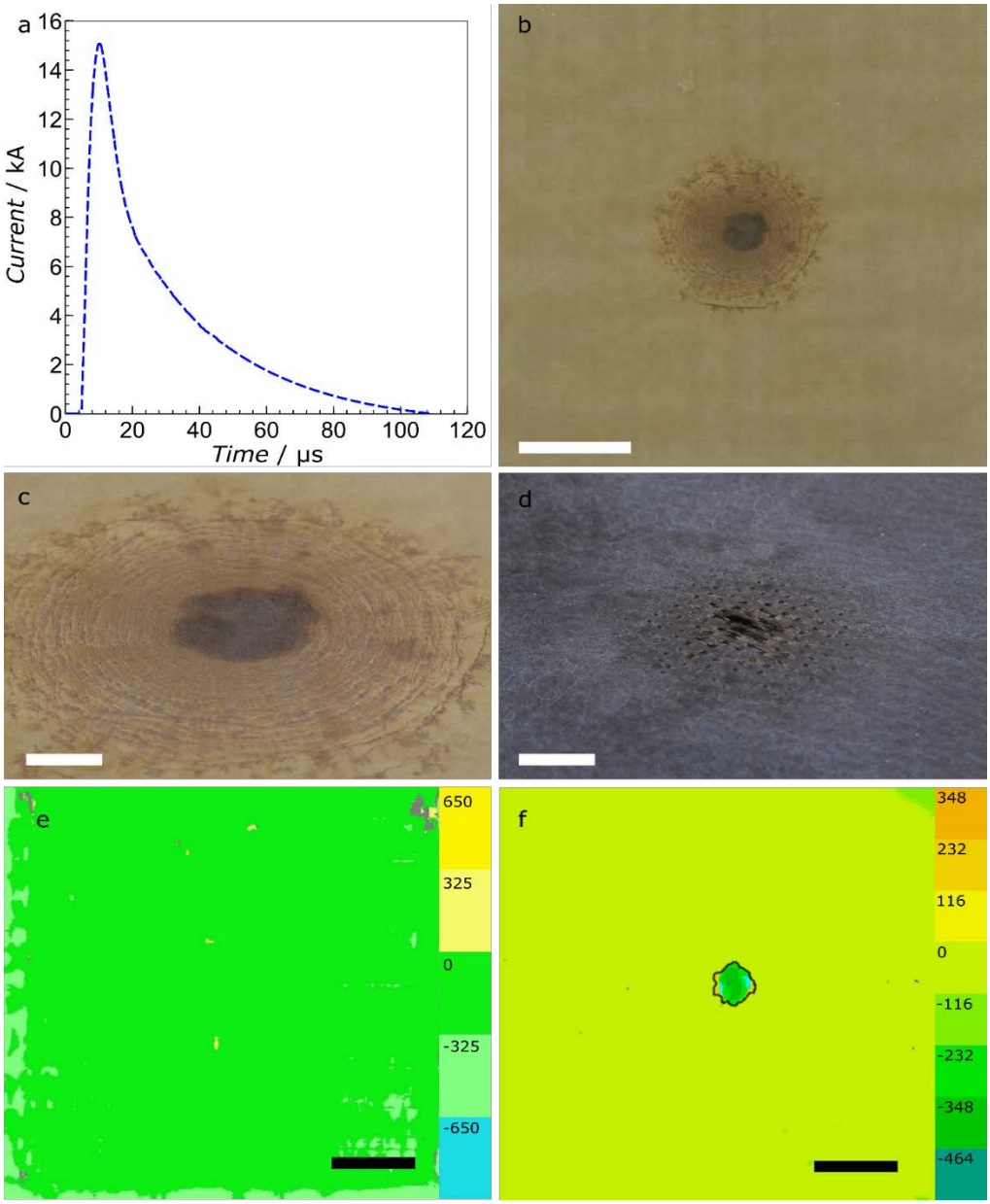

Figure 6.6: Lightning strike simulation. a) The current waveform generated by the simulator, with a peak current of 15 kA and an action integral of 2650 A^2s b) A photograph showing the whole surface of the nanocomposite protected CFRP panel. Scale bar = 5 cm. c) An angled photograph of the surface showing the absence of lifted plies. Scale bar = 1 cm. d) A photograph of an unprotected CFRP panel subjected to the same current discharge as in a). Scale bar = 1 cm. e) C-scan of the nanocomposite protected CFRP panel surface showing no damage. Scale bar = 50 mm. The color scale units are µm. f) C-scan of the unprotected CFRP panel surface showing significant damage. The area around the leader attachment point is slightly swelled and the strike zone shows damage to the composite. Scale bar = 50 mm. The color scale units are µm

6.3.1 Conclusion

The achievement of near metallic conductivities in polymer-based materials remains a challenge, with the available solutions having considerable downsides such as a high cost, an important weight penalty, a negative impact on mechanical properties and an insufficient conductivity. We tackled this problem by developing a new class of conductive fillers that take advantage of the high aspect ratio and low weight of carbonaceous fibrous fillers and of the high conductivity and low contact resistance of silver metal. We successfully performed electroless coating of carbon nanofibers with silver metal resulting in a smooth, uninterrupted coating of silver on the nanofibers' surface. The nanoparticles were then successfully integrated in a conventional aerospace-grade epoxy surfacing film to provide a conductive coating for carbon fiber-epoxy composite panels. The conductivity reached was of 2.5×10^5 S/m, as high as the conventional, class-leading, silver filled adhesives though with a ten-fold decrease in volume fraction which allows for considerable improvements in noble metal costs and weight. We subjected the panels to simulated lightning strikes equivalent to the lesser 35% of the most severe lightning environment to which aircrafts are subjected. The coating was proved to protect the underlying composites efficiently with no detectable damage on ultrasonic scans. The technology might very well in a near future replace conventional metallic fillers in isotropic conductive adhesives and was proven to provide a near metallic surface conductivity at a very low weight penalty of 2.8 mg/cm^2, enough even to divert lightning energy. Although the manufacturing process is simple, it was found to be highly sensitive to manipulation errors. If the technology were to be scaled up, important work on the definition of process parameters would have to be undertaken. We nevertheless think that this works represents a big step forward in the field, and a valuable addition to bottom-up synthesis of nanomaterials.

6.4 Experimental Section

6.4.1 Functionalisation :

Pyrograf Carbon nanofibers PR-25-XT-HHT were obtained from Sigma-Aldrich. Acid functionalization was performed by immersion dry nanofibers (2 g) in a 3:1 vol. H_2SO_4 (Anachemia ACS 95-98%):HNO_3(Anachemia ACS 68-70%) mixture (140 ml) and sonicating in a 42 kHz Cole-Parmer 08891-11 ultrasonic cleaner. The mixture was rinsed several times with deionized H_2O

until the pH is neutral. The obtained nanofibers were then dispersed into deionized water for storage.

6.4.2 Sensitization :

A 1 vol.% $SnCl_2$ solution (160 ml) was prepared to which was added HCl (0.6 ml) (Anachemia, 36.5-38 %, ACS reagent). Functionalised CNFs (100 mg) were removed from deionized water by vacuum filtration and dispersed in the solution. The mixture was ultrasonicated for 45 minutes, left to dwell for 90 minutes at room temperature and then sonicated again for 45 minutes, keeping the mixture temperature below 45 °C at all times. The nanoparticles dispersion was then immediately rinsed several times until pH is neutral and no Cl^- ions are detected in the filtrate by Ag^+ precipitation. Never in the process are the CNFs allowed to dry. The CNFs were dispersed into H_2O (350 ml) for storage.

6.4.3 Solutions preparation :

Solution A: A 20 wt.% dextrose (Sigma Aldrich, ACS) solution (90g) was prepared to which denatured ethanol (15 ml, Macron, ACS) was added. Functionalized and sensitized CNF dispersion (175 ml) was added to the dextrose solution. **Solution B:** A 0.5 M $AgNO_3$ (60 ml, Alfa Aesar, ACS) solution was prepared to which was added 6×10^{-2} M KOH (1 ml, Anachemia, ACS) solution dropwise. At this point, the solution was of a cloudy yellowish brown color. Ammonium hydroxide (4 ml, Alfa Aesar, 28% NH_3) was added dropwise to the solution or until it just turned clear again (a few extra drops may be needed).

6.4.4 Silver deposition :

A 500 ml glass bottle was cleaned by swirling HNO_3 on the inside and rinsing with plenty of deionised water until pH is neutral. Solution A was then poured into the bottle, followed by solution B. The bottle was then closed with a cap and vigorously agitated. 12 minutes after the cap was closed, the nanoparticles dispersion was poured in a vacuum filtration apparatus. The particles were then rinsed with plenty of water without allowing them to dry. Particles were stored by completely immersing in deionized water.

6.4.5 Conductivity measurements :

Electrical conductivity was measured using a 4 point probe (Jandel 100µm tip, 1 mm spacing, linear array) hooked to a current source (Keithley 220) and multimeter (Hewlett Packard 34401A). Correction factors for the sample geometry were applied where applicable. Three sets of five voltage vs. current measurements were obtained on three different zones of the sample and a two parameter linear fit was performed to determine the conductivity value.

6.4.6 Imaging :

SEM images were obtained using a JEOL JSM7600F field emission scanning electron microscope in secondary electron imaging mode. The acceleration tension was set at 10.0 kV with a working distance of approximately 8 mm. TEM images were obtained on a JEOL JEM-2100F microscope equipped with a field emission electron gun. Acceleration voltage was 200 kV.

6.4.7 Coating fabrication :

2 g hybrid nanoparticles were dispersed in 500 ml DI water by stirring and mechanical agitation in a closed vessel. The dispersion was then quickly poured into a home-made filtration apparatus consisting of a 30 cm by 30 cm filter plate holding a polycarbonate filter membrane (Sterlitech, hydrophilic, 0.4 µm porosity, 300x3000 mm). The clamped area of the filter, which is exposed to the dispersion, is a square with a side dimension of 257 mm. The as-obtained nanoparticles layer was then left to dry overnight. The film was then transferred to an 12.7 mm thick aluminum plate and a carbon fiber-epoxy coupon with an uncured film of aerospace grade surfacing film (Cytec Surface Master 905, 0.035 psf) was placed with the tacky surface against the nanoparticles. A vacuum bagging was then used to press the film and the coupon against the nanoparticles with uniform pressure. Release agent (Loctite Frekote 770-NC) was then applied to the aluminum plate and the assembly was placed with the nanoparticles face down on the aluminum tool A heat probe was attached to the backside of the carbon fiber coupon with aluminum tape. A vacuum bagging was then prepared and vacuum was pulled from the assembly. The aluminum tool along

with the assembly were then placed on a hot plate pre-heated to 170 °C, at which point the temperature acquisition was transferred to the probe attached to the sample. When the temperature reading indicated 160 °C, the temperature setpoint was brought back to 130 °C. The film was then cured at 130°C for 90 minutes.

6.4.8 Lightning strike emulation :

The emulator was built in École Polytechnique de Montréal and is based on capacitive storage. The test sample was clamped in a copper frame which acts as a negative electrode. The positive electrode, from which the arc originated, consists of a pointed striker located 6.4 mm over the plane of the sample.

6.4.9 Ultrasonic inspection :

The panels were immersed in a water bath and subject ted to 5 MHz ultrasonic energy from 64 elements scanning probe (LM-5MHz, Zetec). The signal acquisition was performed by a topaz 32/128 PR (Zetec) unit. The sample distance was held constant at 110 mm.

6.5 Supporting Information

6.5.1 Choice of template particles

Figure 6.7 shows the initial silver deposits on a CNF surface. The smallest silver nanoparticle measurable dimension is of 22 nm, which remains small compared to the CNF diameter. CNTs, on the other hand, typically have a diameter in the 10 nm order of magnitude, which is equal or smaller to the initial deposits. Therefore, if one would require uniform deposition of silver on a CNT sample, it would be expected that the thickness of the silver layer would completely dominate the carbon particle diameter, resulting in a greatly diminished aspect ratio and a mechanically weakened particle.

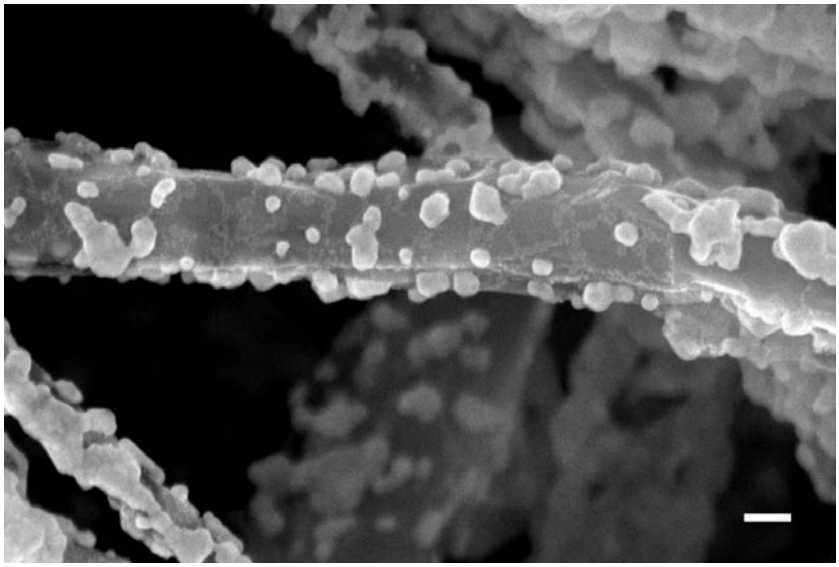

Figure 6.7: SEM image of crystallite size upon initial silver deposition after 72 s reaction time. The smallest measurable silver particle dimension is ~22 nm. The scale bar = 100 nm

6.5.2 Deposition rate

The time dependence of the sample mass was found by postulating that the deposition rate was proportional to species concentration in solution, and that it consumed some of these species during the reaction. The deposition rate is then postulated to be given by:

$$r = Ce^{-\lambda t}, \tag{15}$$

where C is a proportionality constant and λ drives the depletion dynamics. The mass of the sample is then given by:

$$m = m_0 + \int_0^{t'} Ce^{-\lambda t} dt' = m_0 + \frac{C}{\lambda}(1 - e^{-\lambda t'}), \tag{16}$$

which is of the form given by Equation (141414).

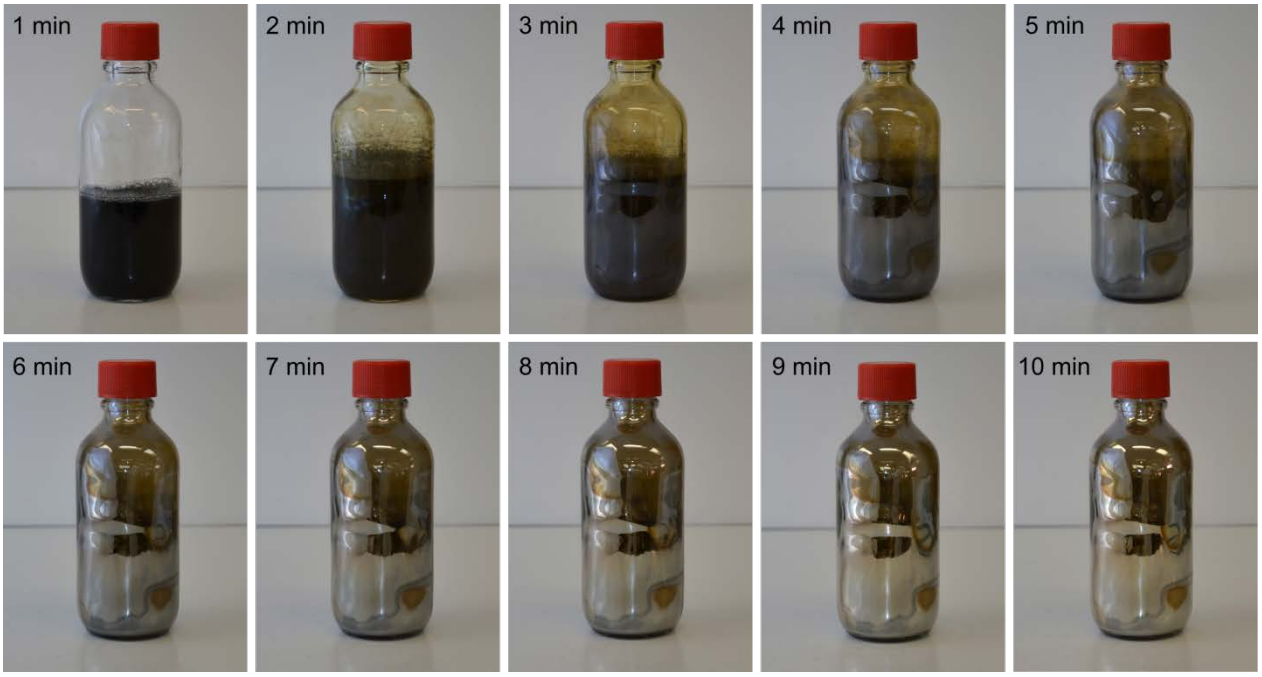

Figure 6.8: Reaction vessel color evolution. In the first minute of reaction, the glass takes a yellow tint that slowly turns to a reddish brown. The glassware becomes opaque to the naked eye at the 10^{th} minute

CHAPTER 7 DISCUSSION

The wide-scale usage of electrical power in industry and housing has driven economic incentives to research and develop conductors with improved efficiency. Yet, copper conductors still overwhelmingly dominate electrical installations around the globe. The omnipresence of copper conductors is attributable to the very large span of values taken by the electrical conductivity of different materials. For copper and glass, for example, it differs by more than 20 orders of magnitude. The other properties for solids very seldom display such a difference, be it in density, stiffness or thermal conductivity. Therefore, when a material's performance for a specific application is measured by a figure of merit combining properties including conductivity, the latter generally dominates.

Among good conductors, copper competes with silver, gold and aluminum. While silver and gold are usually prohibitively expensive for large-scale applications, aluminum, although almost twice as resistive as copper, has interesting properties which justifies replacing copper in certain applications.

Nowhere, perhaps, is the mindful management of mass more paramount than in aerospace. The sector historically has made wide usage of aluminum, both for structural and wiring purposes. The very same reason that motivated using aluminum in aircrafts has now pushed the industry towards more and more carbon fiber composites in structural areas, thus creating a new problem by removing the excellent conductivity of the aluminum fuselage. The need for an increased electrical conductivity in the fuselage calls for creative solutions. In the meantime, engineers resorted once more to copper in the form of an interconnected mesh bonded to the craft's skin which diminishes the specific stiffness gain achieved by introducing composites. Here, the combination of the need for a high electrical conductivity and the high economic incentive to weight reduction justifies research into new strategies to provide enhanced electrical conductivity to composite materials.

Carbon materials and nanomaterials are very interesting for this purpose as they have low density and a high conductivity. The potential of these materials however remains mostly untapped because of the major hindrance of contact resistivity. As carbon particles are brought together to form a network, the current must flow in the out-of-plane direction, as the contact region is generally tangential to the graphitic plane curvature. Electron transport in this direction does not display the performance of in-plane directions and the contact resistance, even in full intimate contact between

the particles, will be significant. Carbon materials are also very thermally stable which prevents sintering of adjacent particles. The issue of contact resistance is then a major challenge that prevents the realization of the full potential the material.

We devised a strategy to mitigate the effects of contact resistance. Our approach was to attach a silver coating to the surface of carbon nanoparticles so that the contact resistance between particles is that of silver. Achieving an uniform silver layer is important for two reasons:

- To provide a continuous silver connection pathway.
- To increase the contact area between carbon and silver thus minimize the effect of contact resistance between the materials.

We did succeed in synthesizing high aspect ratio carbon nanoparticles with a continuous coating. However, it is not clear to which extent we did succeed in using the carbon material itself to its full potential. If there had been a synergistic effect, one would have expected the specific conductivity to reach a maximum as enough silver is added to ease contact resistance but not enough to completely dominate the transport properties. The specific resistivity plot of Figure 6.3 would then have reached a maximum value before decreasing asymptotically to the characteristic value of silver since the fractional volume of carbon diminishes with time. It does however evolve straight to a flat profile which suggests that carbon does not contribute positively to the specific conductivity. We do not however have direct measurements allowing to discriminate each material's contribution to the conductivity.

The challenge of replacing the standard copper material is a difficult one: copper is the preferred conductor among all metals, and in its expanded mesh form it is perfectly connected with no contact resistance. Since materials' densities normally differ by less than an order of magnitude but the conductivities scale by tens of orders of magnitude, the gain in weight achieved by changing materials is easily obscured by the change in conductivity. We did however present an alternative that displayed a specific resistivity similar to that of commercial systems with added benefits such as the potential to be formulated as paints or incorporated into resins.

The cost of the technology can also be worrisome as silver compounds are not cheap. The mass of silver used in the experiments is of the order of 30 g/m^2. If we assume as a worst-case scenario the mass of fillers to be 100% silver and a 50% silver loss in the deposition process – which is very

unlikely in an optimized process – using a bulk cost of silver nitrate of 400$ per kg yields a total silver cost of 37.8 $/m^2. Note here that this is analogous to the mirror fabrication process: even genuine silver mirrors manufactured with a process similar to ours are very affordable, the weight of metal being thinly spread over a very large area. The cost of carbon nanoparticles do not add much to the total: Approximately 2% of the mass of the particles is attributable to the carbon core and we expect bulk prices on the order of 1$/g, considering the current retail price for small quantities. The additional cost then amounts to approximately 0.6 $/m^2.

While this raw materials cost represents a hindrance to the large-scale adoption of the technology, it is not completely prohibitive and might justify targeted applications where geometry or compatibility factors limit the use of metallic meshes. Additionally , and maybe more importantly, the technology developed here provides a new tool in the design of conductive composite materials and polymer-based electronics with a marked potential as a filler for 3D printing polymers. These technology segments are constantly facing new challenges and finding new applications. We believe this addition to the nanocomposites body of knowledge could be of great impact in a near future.

CHAPTER 8 CONCLUSION AND RECOMMENDATIONS

8.1 Conclusion

Different strategies to provide a near-metallic electrical conductivity to carbon fiber reinforced epoxy composite panels were explored. The main body of work was shared between two strategies:

- The in-situ formation of metallic fillers in an epoxy matrix with phase-driven segregation
- High aspect ratio carbon-silver nanofillers.

The first strategy was studied using a two-part water-based epoxy emulsion and a water-based silver precursor ink. Amongst curing, the silver precursor reduced to atomic silver preferentially within the aqueous host phase which formed a connected network in the emulsion. This stimulated percolation mechanism allowed to attain a percolation threshold as low as 0.27% which is remarkably low for metallic fillers, two orders of magnitude below the value for spherical fillers and a 40-fold decrease when compared to conventional conductive adhesives.

The highest conductivity achieved was of 5.4×10^3 S/cm for a 12.3 vol.% silver loading which amounts to a specific conductivity of 2.5×10^3 $S\cdot cm^2/g$ is comparable to existing commercial LSP systems. The drawbacks of this method however quickly became apparent. First, the large amount of solvent required for the fabrication of the particle-less silver ink needed to be evaporated during the curing of the material. The gases produced during this step needed a way out of the polymer, which means that only a very thin layer could be applied at a time. The process thus required several curing steps in which the surface would be heated to a temperature of at least 200 °C, which is not compatible with the resin systems used the composite fuselage panels. This requisite did also make the process very time-consuming and difficult to control. Also, higher silver contents could have been realized, although at this point issues started to appear relating to the stability of the colloidal solution. A focused research might find a solution to these drawbacks, but it would require in-depth research into polymer chemistry which was beyond the scope of the current work.

The work then shifted towards solving the problem of contact resistance of nanofillers in polymeric matrices. The approach identified was to deposit a metallic coating on high aspect ratio carbonaceous nanoparticles to benefit from both the metal's low contact resistance and the carbon particles' morphology. Carbon nanofibers were chosen as the core particles for their high aspect

ratio and because their diameter allow for a metal coating to develop without completely dominating the dimensions of the particle. The metal chosen was silver for its high conductivity and its unique ability to sinter at a low temperature.

The deposition of silver metal on the nanoparticles was divided into three steps:

- Functionalization and cleaning of carbon core particles
- Sensitization of carbon core particles surface
- Silver deposition

Functionalization was achieved by immersing the nanoparticles in a mixture of sulfuric and nitric acid in the proportions 3:1. It was found that refluxing time and process temperature had an influence on the oxygen content of the functionalized nanoparticles at the expense of the process yield. Subjecting the mixture to ultrasonic agitation proved to be a more efficient process by allowing a lower process temperature for an equivalent oxygen content and a higher yield. Functionalized nanoparticles displayed an 11.7 at. % content without supplying heat to the process other than that generated by the bath itself. SEM images showed minimal damage to the particles' structure.

The next step in the process is historically called sensitization. It consists in the adsorption in acidic solution of tin-containing species at the surface of the substrate to be coated. A rather large body of work was consecrated to the phenomenon with comparatively little gain in the understanding of the root chemical reactions involved. We chose to investigate the effect of the acid contents in solution as it was previously reported with reasonable evidence to affect the underlying mechanisms governing the efficiency of the manipulation. We showed that an acid concentration range existed for a chosen $SnCl_2$ concentration where the stability of the sensitized carbon nanoparticles dispersion would be maximized. We hypothesized that this optimized solution would translate to a uniform coating of tin species on the particles and therefore would yield a more uniform silver coating upon initiation of the silver nanoparticles nucleation at the reactive sites. TEM images of sensitized carbon nanofibers revealed a very high density of tin dioxide crystallites, an order of magnitude higher than the value reported for an optimized solution in literature. XPS measurement confirmed that the crystallites observed were indeed composed of tetravalent tin in a stoichiometry corresponding to tin dioxide.

Silver deposition itself was studied through three separate parameters with the conductivity of the bulk nanoparticles as the value of interest. First, the concentration of the silver reactive species was varied with a fixed concentration of reducing agent. An optimal region was identified which served as a starting point for the next experiment where the concentration of the reducing agent was varied. The latter was found to have little effect on the observable except for the region where the reducing agent is a limiting factor for the reaction.

In a different publication, we investigated the effect of deposition time on the electrical conductivity of the bulk and on the morphology of the silver coating. The experiment showed that the coating developed through two simultaneous processes:

- The growth of silver seeds and
- The nucleation of new seeds,

as opposed to our initial thoughts that the timescale of the nucleation processes had to be much shorter than seed growth and that both processes should therefore be consecutive. A sharp increase in the specific electrical conductivity develops initially in the process and levels off quickly at a maximum value which is maintained from then on. The morphology shows an analogy with a percolation scheme explaining this observation: A conduction network is first established as individual seeds are connected through growth and the addition of new seeds. Once the network is established, the additional metal contributes to the conductivity only proportionally to the incremental mass added, hence the constant specific conductivity value.

When in the shape of a loose powder uniformly spread out as a film, the specific conductivity of the nanoparticles reached a value as high as 2500 $S \cdot cm^2/g$, which is about 4.2% of the value of bulk silver. This result trumps earlier observations to the effect that nanoparticles, upon compaction, would only reach 1% of the conductivity of the bulk. We attribute this increase in performance to the morphology of the particles, which allows each particle to make more contacts with its neighbors and allows the charges to be transported further without having to hop from one particle to the other.

Having tailor-made particles to enhance conductivities in polymeric nanocomposites, the challenge of integrating the technology into a functional coating remained. As literature showed, the percolation phenomenon, although it provides a dramatic increase in conductivity, does not provide

a sufficiently dense network of conductors to yield the quasi-metallic behavior which is required for our target application. The coating therefore had to incorporate a very large volume fraction of fillers. To achieve such a volume fraction, the resin infusion scheme was preferred to the liquid state mixing of resin and fillers. We prepared a layer of nanoparticles through a papermaking process with a sub-micron polycarbonate membrane. Simply tacking the solids allowed to transfer the conductive particle to a B-staged epoxy resin film which could then be applied to a CFRP substrate. Atmospheric pressure was sufficient to infuse the solids layer through a vacuum-assisted resin infusion scheme. As an added benefit, the pressure resulting from the applied vacuum helped in compacting the particles further, thus creating new compact points and strengthening existing contacts. Resin shrinkage would also contribute to the strengthening of the contact points, although it is expected to be marginal in the system used.

We witnessed a 50% increase in the specific conductivity of the conductive layer upon incorporation in the resin, bringing the value up to 3820 $S \cdot cm^2/g$. The panels showed a uniform, smooth surface with a nanoparticles volume density of 6.3% and a volume conductivity of 2.5×10^5 S/m, comparable to that of conductive adhesives with 10 times more fillers. When subjected to a simulated lightning strike of the lesser 35% severity, the protective coating succeeded in protecting the carbon fiber laminate at the expense of a minimal incremental weight of 2.8 mg/cm^2 whereas the lightest copper mesh is 7.3 mg/cm^2.

8.2 Recommendations

In deciding on the focus of the investigations, one of the influential hypothesis was that the carbon nanoparticle network would contribute to the specific conductivity in a non-negligible fashion. We've however seen that this does not seem to be the case. It would be very informative to investigate this subject in further work. An interesting experiment to perform in this regard would be to work out the temperature dependence of the electrical conductivity of nanoparticles samples with different silver loadings. We know that silver and carbon have very different behaviors upon temperature variations: silver behaves as would be expected in the Drude model of electron transport while graphitic carbon sees its conductivity increase with an increase in temperature. Knowing each solid's behavior, one can deconvolute the cumulative effect of both elements in the measured curve and extract a coefficient that will yield information on the importance of each contribution to the composite electrical conductivity.

If it arises that, as we suspect, the carbon core has a very limited effect on the conductivity, the causes should be identified. Knowing these could steer the research towards a solution to the problem and lead to improvements in the technology. Among possible culprits is the intermediate layer of tin that was deposited on the carbon substrate. It is a known fact that establishing an ohmic contact with carbon nanotubes is a challenge. Mann *et al* showed that palladium was performing exceptionally in this respect. [186]

Although carbon nanofibers are different from carbon nanotubes in many regards, it is not unreasonable to expect some results from the CNT literature to be transferable to nanofibers. Interestingly, palladium is often used in electroless plating in the "activation" step, immediately after tin sensitization to provide a good silver coating. We sought to achieve a Pd-less process since the metal is very expensive, but in the light of our results, it would be of interest to investigate the performance difference between Pd-activated and Pd-free carbon-silver nanofibers. Other metals for plating might also be of interest. Among these, zinc is known to be efficient in electroless plating, although it does not display the very high sinterability of silver metal

It is a known fact that nanofillers impart different properties to their polymer composites depending on the dispersion state they achieve in the process. Although in this work we've detailed the dispersion state of precursor particles, we did not conduct thorough work on the dispersion state of the hybrid particles in water. We did however provide in Chapter 5 hints that point to the role of

poly(acrylic acid) (PAA) as a capping agent, and further manipulations confirmed that PAA did inhibit the change in color observed in Figure 5.13. Moreover, capping the nanoparticles with PAA facilitated the dispersion of the nanoparticles in water which allowed to avoid the use of ultrasounds and therefore to preserve the particles' integrity. The initial strategy was to avoid all capping agents to facilitate an intimate contact between adjacent particles. However, in the light of late observations, this strategy is probably not optimal. We would recommend running experiments with different dispersants to evaluate the electrical performance of nanoparticle mats obtained through our method.

Some interesting applications may arise from the work done herein. Among these, we think that conductive adhesives hold promise. One of the advantages that our fillers might impart to this class of materials is resilience to thermal cycling. It was shown that the shear strength of the adhesive is negatively affected by higher filler loadings [138]. To maintain the strength of the joint, Kotthaus *et al*. developed fillers consisting of sintered silver nanoparticles. The porous particles were expected to have less impact on the mechanical properties of the resin. They observed a two-fold improvement of the properties of the joint [187]. The very low filler volume fraction achieved here might therefore translate into significant advantages in the field. Moreover, preliminary results indicate that such adhesives might also achieve interesting thermal conductivity at low volume fractions. Using the modulated dynamic scanning calorimetry method described in [188], we obtained a value of 4.2 W/m°C for a sample of 1.7 g/cm^3 density, which translates to a filler volume fraction of 7.4%, an order of magnitude lower than commercial alternatives.

For these applications, research work should be accomplished regarding the incorporation of the nanoparticles into polymers. Owing to their size, which sits at the upper frontier of the "nano" domain, the Van der Walls forces acting on the hybrid particles are easier to overcome than they are in *e.g.* carbon nanotubes. Accordingly, less energy is required to separate the aggregates. Unfortunately, the particles are also sensitive to ultrasonic energy and degrade easily into lower aspect ratio particles. We found that a moderate shear applied to the polymer dispersion was efficient in dispersing the particles. Systematic research on the topic could help in providing guidelines to expand the application of the nanoparticles to different polymer matrices.

Finally, we observed that the plating solution could be reactivated by adjusting the pH during the reaction. In one of such experiments, we measured a weight increase in the end product

corresponding to all the silver in solution. This hints that the process can be tailored to allow all silver to react and therefore minimize the post processing that would be required in an economically viable process to recuperate unreacted silver. If an application is to be developed, more work on this topic will undoubtedly make the technology more appealing to the industry.

BIBLIOGRAPHY

[1] A. Larsson, "The interaction between a lightning flash and an aircraft in flight," *Comptes Rendus Physique,* vol. 3, no. 10, pp. 1423-1444, 2002.

[2] M. A. Uman and V. A. Rakov, "The interaction of lightning with airborne vehicles," *Progress in Aerospace Sciences,* vol. 39, no. 1, pp. 61-81, 2003.

[3] F. A. Fisher *et al.*, *Lightning protection of aircraft*. National Aeronautics and Space Administration, Scientific and Technical Information Office ; for sale by the Supt. of Docs., U.S.Govt.Print.Off., 1977.

[4] K. S. Toohey, N. R. Sottos, J. A. Lewis, J. S. Moore, and S. R. White, "Self-healing materials with microvascular networks," *Nat Mater,* vol. 6, no. 8, pp. 581-5, Aug 2007.

[5] V. P. Veedu *et al.*, "Multifunctional composites using reinforced laminae with carbon-nanotube forests," (in eng), *Nature Materials,* vol. 5, no. 6, pp. 457-62, Jun 2006.

[6] D. R. Rolison *et al.*, "Multifunctional 3D nanoarchitectures for energy storage and conversion," *Chem Soc Rev,* vol. 38, no. 1, pp. 226-52, Jan 2009.

[7] W. Bauhofer and J. Z. Kovacs, "A review and analysis of electrical percolation in carbon nanotube polymer composites," *Composites Science and Technology,* vol. 69, no. 10, pp. 1486-1498, 2009.

[8] M. Gagné and D. Therriault, "Lightning strike protection of composites," *Progress in Aerospace Sciences,* 2013.

[9] H. Kawakami and P. Feraboli, "Lightning strike damage resistance and tolerance of scarf-repaired mesh-protected carbon fiber composites," *Composites Part A: Applied Science and Manufacturing,* vol. 42, no. 9, pp. 1247-1262, 2011.

[10] Y. Hirano, S. Katsumata, Y. Iwahori, and A. Todoroki, "Artificial lightning testing on graphite/epoxy composite laminate," (in English), *Composites Part a-Applied Science and Manufacturing,* vol. 41, no. 10, pp. 1461-1470, Oct 2010.

[11] P. Feraboli and H. Kawakami, "Damage of Carbon/Epoxy Composite Plates Subjected to Mechanical Impact and Simulated Lightning," *Journal of Aircraft,* vol. 47, no. 3, pp. 999-1012, 2010.

[12] P. Feraboli and M. Miller, "Damage resistance and tolerance of carbon/epoxy composite coupons subjected to simulated lightning strike," *Composites Part A: Applied Science and Manufacturing*, vol. 40, no. 6-7, pp. 954-967, 2009.

[13] N. I. Petrov, A. Haddad, G. N. Petrova, H. Griffiths, and R. T. Waters, "Study of Effects of Lightning Strikes to an Aircraft," 2012.

[14] J. B. O'Loughlin and S. R. Skinner, "General Aviation Lightning Strike Report and Protection Level Study," 2004.

[15] L. Chemartin, "Modélisation des arcs électriques dans le contexte du foudroiement des aéronefs," Ph.D., Université de Rouen, 2008.

[16] J. A. Plumer, "Laboratory test results and natural lightning strike effects: How well do they compare," in *Lightning Protection (ICLP), 2012 International Conference on*, 2012, pp. 1-17.

[17] *ARP5414: "Aircraft Lightning Zoning" Rev. A*, 2005.

[18] L. Chemartin *et al.*, "Direct Effects of Lightning on Aircraft Structure: Analysis of the Thermal, Electrical and Mechanical Constraints," *Aerospace Lab*, no. 05, p. 15, 2012.

[19] *ARP5412: "Aircraft Lightning Environment and Related Test Waveforms" Rev. A*, 2005.

[20] M. Meyer, F. Flourens, J. A. Rouquette, and A. Delnevo, "Modeling of lightning indirect effects in CFRP Aircraft," pp. 1-5, 2008.

[21] G. B. Sweers, B. Gocken, J., "Lightning strikes: Protection, Inspection, and Repair," *Aero*, vol. 48, no. 4, p. 9, 19.

[22] S. Black, "Lightning strike protection stategies for composite aircraft," *High Performance Composites*, 5/1/2013. Accessed on: 8/9/2013Available: http://www.compositesworld.com/articles/lightning-strike-protection-strategies-for-composite-aircraft

[23] G. Gardiner, "Lightning Strike Protection For Composite Structures," *High-Performance Composites*, Accessed on: 9/8/2013Available: http://www.compositesworld.com/articles/lightning-strike-protection-for-composite-structures

[24] Henkel Corporation. *Lightning Strike Products*. Available: http://ableaero.com/tds/Henkel_Lightning_Strike_Products.pdf

[25] Dexmet Corporation. (2013-09-04). *Microgrid precision expanded metals*. Available: http://www.dexmet.com/Expanded-Metals.html

[26] L. Corporation, "LORD® UltraConductive Film and Coatings for Lightning Strike Protection," ed.

[27] APCM. *Specialty Products*. Available: http://www.prepregs.com/products.html

[28] J. Morgan, "Thermal Simulation and Testing of Expanded Metal Foils Used for Lightning Protection of Composite Aircraft Structures," *SAE Int. J. Aerosp.*, vol. 6, no. 2, pp. 371-377, 2013.

[29]

[30] S. Black, "After lightning strikes: Repair considerations," *High Performance Composites*, Available: http://www.compositesworld.com/articles/after-lightning-strikes-repair-considerations

[31] Hexcel Corporation. (2013-09-16). *Thorstrand™ product data*. Available: http://www.hexcel.com/Resources/DataSheets/Prepreg-Data-Sheets/Thorstrand_us.pdf

[32] T. D. Fornes, S. B. Carruthers, and N. D. Huffman, "Method for protecting a substrate from lightning strikes," Patent US 2011/0014356 A1, 2011.

[33] T. D. Fornes and N. D. Huffman, "Method for producing heterogeneous composites," US Patent US 2010/0001237 A1, 2010.

[34] Conductive Composites. (2012, 2013-09-16). *Metal CVD Coated Nonwovens for Electrical Conductivity and Electromagnetic Shielding*. Available: http://www.conductivecomposites.com/pdf/NiShield%20CVD%20Nonwoven%20Data%20Sheet.pdf

[35] J.-h. Han *et al.*, "The combination of carbon nanotube buckypaper and insulating adhesive for lightning strike protection of the carbon fiber/epoxy laminates," *Carbon*, vol. 94, pp. 101-113, 2015.

[36] K. K. Fu, L. Ye, L. Chang, C. H. Yang, and Z. Zhang, "Modelling of lightning strike damage to CFRP composites with an advanced protection system. Part I: Thermal-electrical transition," (in English), *Composite Structures*, vol. 165, pp. 83-90, Apr 1 2017.

[37] Q. Zhang, *Pan Stanford Series on Carbon-Based Nanomaterials : Carbon Nanotubes and Their Applications*. Boca Raton, FL, USA: Pan Stanford Publishing, 2012, p. 601.

[38] N. W. Ashcroft and N. D. Mermin, *Solid state physics*. Saunders College, 1976.

[39] J.-C. Charlier and S. Roche, "Electronic and transport properties of nanotubes," *Reviews of Modern Physics*, vol. 79, no. 2, pp. 677-732, 2007.

[40] T. Ando, "The electronic properties of graphene and carbon nanotubes," *NPG Asia Materials*, vol. 1, no. 1, pp. 17-21, 2009.

[41] O. Breuer and U. Sundararaj, "Big returns from small fibers: A review of polymer/carbon nanotube composites," *Polymer Composites*, vol. 25, no. 6, pp. 630-645, 2004.

[42] Z. Yao, C. Kane, and C. Dekker, "High-Field Electrical Transport in Single-Wall Carbon Nanotubes," *Physical Review Letters*, vol. 84, no. 13, pp. 2941-2944, 2000.

[43] Z. Zhang, J. Peng, and H. Zhang, "Low-temperature resistance of individual single-walled carbon nanotubes: A theoretical estimation," *Applied Physics Letters*, vol. 79, no. 21, pp. 3515-3517, 2001.

[44] V. Skákalová, A. Kaiser, Y. S. Woo, and S. Roth, "Electronic transport in carbon nanotubes: From individual nanotubes to thin and thick networks," *Physical Review B*, vol. 74, no. 8, 2006.

[45] B. Bourlon, C. Miko, L. Forró, D. Glattli, and A. Bachtold, "Determination of the Intershell Conductance in Multiwalled Carbon Nanotubes," *Physical Review Letters*, vol. 93, no. 17, 2004.

[46] H. Li, W. Lu, J. Li, X. Bai, and C. Gu, "Multichannel Ballistic Transport in Multiwall Carbon Nanotubes," *Physical Review Letters*, vol. 95, no. 8, 2005.

[47] A. Stetter, "Conductivity of multiwall carbon nanotubes: role of multiple shells and defects," vol. 21, ed, 2011.

[48] T. W. Ebbesen, H. J. Lezec, H. Hiura, J. W. Bennett, H. F. Ghaemi, and T. Thio, "Electrical conductivity of individual carbon nanotubes," *Nature,* vol. 382, no. 6586, pp. 54-56, 1996.

[49] M. J. Kim *et al.*, "Nanoscopically flat open-ended single-walled carbon nanotube substrates for continued growth," *Nano Lett,* vol. 7, no. 1, pp. 15-21, Jan 2007.

[50] S. Ramesh *et al.*, "Dissolution of Pristine Single Walled Carbon Nanotubes in Superacids by Direct Protonation," *The Journal of Physical Chemistry B,* vol. 108, no. 26, pp. 8794-8798, 2004.

[51] A. N. Parra-Vasquez *et al.*, "Spontaneous dissolution of ultralong single- and multiwalled carbon nanotubes," (in eng), *ACS Nano,* vol. 4, no. 7, pp. 3969-78, Jul 27 2010.

[52] L. Vaisman, H. D. Wagner, and G. Marom, "The role of surfactants in dispersion of carbon nanotubes," (in eng), *Adv Colloid Interface Sci,* vol. 128-130, pp. 37-46, Dec 21 2006.

[53] R. Rastogi, R. Kaushal, S. K. Tripathi, A. L. Sharma, I. Kaur, and L. M. Bharadwaj, "Comparative study of carbon nanotube dispersion using surfactants," (in English), *J Colloid Interface Sci,* vol. 328, no. 2, pp. 421-428, Dec 15 2008.

[54] P.-C. Ma, N. A. Siddiqui, G. Marom, and J.-K. Kim, "Dispersion and functionalization of carbon nanotubes for polymer-based nanocomposites: A review," *Composites Part A: Applied Science and Manufacturing,* vol. 41, no. 10, pp. 1345-1367, 2010.

[55] S. U. Khan and J.-K. Kim, "Improved interlaminar shear properties of multiscale carbon fiber composites with bucky paper interleaves made from carbon nanofibers," *Carbon,* vol. 50, no. 14, pp. 5265-5277, 2012.

[56] S. Movva, X. Ouyang, J. Castro, and L. J. Lee, "Carbon nanofiber paper and its effect on cure kinetics of low temperature epoxy resin," *Journal of Applied Polymer Science,* vol. 125, no. 3, pp. 2223-2230, 2012.

[57] J. Yunguang, L. Yueh-Jaw, and J. S. C. Wong, "Buckypaper's Fabrication and Application to Passive Vibration Control," in *Nano/Micro Engineered and Molecular Systems, 2006. NEMS '06. 1st IEEE International Conference on,* 2006, pp. 725-729.

[58] A. Ansón-Casaos, J. M. González-Domínguez, E. Terrado, and M. T. Martínez, "Surfactant-free assembling of functionalized single-walled carbon nanotube buckypapers," *Carbon*, vol. 48, no. 5, pp. 1480-1488, 2010.

[59] S. Wang, D. Haldane, R. Liang, J. Smithyman, C. Zhang, and B. Wang, "Nanoscale infiltration behaviour and through-thickness permeability of carbon nanotube buckypapers," (in eng), *Nanotechnology*, Research Support, U.S. Gov't, Non-P.H.S. vol. 24, no. 1, p. 015704, Jan 11 2013.

[60] S. Li, J. G. Park, R. Liang, C. Zhang, and B. Wang, "Effects of solvent immersion and evaporation on the electrical conductance of pre-stressed carbon nanotube buckypapers," (in eng), *Nanotechnology*, vol. 22, no. 36, p. 365706, Sep 7 2011.

[61] J. G. Park, S. Li, R. Liang, X. Fan, C. Zhang, and B. Wang, "The high current-carrying capacity of various carbon nanotube-based buckypapers," (in eng), *Nanotechnology*, vol. 19, no. 18, p. 185710, May 7 2008.

[62] G. Mechrez, R. Y. Suckeveriene, R. Tchoudakov, A. Kigly, E. Segal, and M. Narkis, "Structure and properties of multi-walled carbon nanotube porous sheets with enhanced elongation," *Journal of Materials Science*, vol. 47, no. 16, pp. 6131-6140, 2012.

[63] I. W. Chen, R. Liang, H. Zhao, B. Wang, and C. Zhang, "Highly conductive carbon nanotube buckypapers with improved doping stability via conjugational cross-linking," (in eng), *Nanotechnology*, Research Support, Non-U.S. Gov't vol. 22, no. 48, p. 485708, Dec 2 2011.

[64] R. Jackson, B. Domercq, R. Jain, B. Kippelen, and S. Graham, "Stability of Doped Transparent Carbon Nanotube Electrodes," *Advanced Functional Materials*, vol. 18, no. 17, pp. 2548-2554, 2008.

[65] J. G. Park *et al.*, "Electromagnetic interference shielding properties of carbon nanotube buckypaper composites," (in eng), *Nanotechnology*, Research Support, U.S. Gov't, Non-P.H.S. vol. 20, no. 41, p. 415702, Oct 14 2009.

[66] R. C. Tenent *et al.*, "Ultrasmooth, Large-Area, High-Uniformity, Conductive Transparent Single-Walled-Carbon-Nanotube Films for Photovoltaics Produced by Ultrasonic Spraying," *Advanced Materials*, vol. 21, no. 31, pp. 3210-3216, 2009.

[67] J.-H. Han, H. Zhang, M.-J. Chen, G.-R. Wang, and Z. Zhang, "CNT buckypaper/thermoplastic polyurethane composites with enhanced stiffness, strength and toughness," *Composites Science and Technology,* vol. 103, pp. 63-71, 2014.

[68] J. Li, P. C. Ma, W. S. Chow, C. K. To, B. Z. Tang, and J. K. Kim, "Correlations between Percolation Threshold, Dispersion State, and Aspect Ratio of Carbon Nanotubes," *Advanced Functional Materials,* vol. 17, no. 16, pp. 3207-3215, 2007.

[69] F. M. Du, J. E. Fischer, and K. I. Winey, "Effect of nanotube alignment on percolation conductivity in carbon nanotube/polymer composites," (in English), *Physical Review B,* vol. 72, no. 12, Sep 2005.

[70] I. Balberg and N. Binenbaum, "Computer study of the percolation threshold in a two-dimensional anisotropic system of conducting sticks," *Physical Review B,* vol. 28, no. 7, pp. 3799-3812, 1983.

[71] C. A. Martin *et al.*, "Formation of percolating networks in multi-wall carbon-nanotube–epoxy composites," *Composites Science and Technology,* vol. 64, no. 15, pp. 2309-2316, 2004.

[72] M. H. Al-Saleh and U. Sundararaj, "A review of vapor grown carbon nanofiber/polymer conductive composites," *Carbon,* vol. 47, no. 1, pp. 2-22, 2009.

[73] Y. L. Li, I. A. Kinloch, and A. H. Windle, "Direct spinning of carbon nanotube fibers from chemical vapor deposition synthesis," (in eng), *Science,* vol. 304, no. 5668, pp. 276-8, Apr 9 2004.

[74] M. Zhang, K. R. Atkinson, and R. H. Baughman, "Multifunctional carbon nanotube yarns by downsizing an ancient technology," *Science,* vol. 306, no. 5700, pp. 1358-1361, 2004.

[75] Q. W. Li *et al.*, "Structure-Dependent Electrical Properties of Carbon Nanotube Fibers," *Advanced Materials,* vol. 19, no. 20, pp. 3358-3363, 2007.

[76] S. Zhang *et al.*, "Solid-state spun fibers and yarns from 1-mm long carbon nanotube forests synthesized by water-assisted chemical vapor deposition," *Journal of Materials Science,* vol. 43, no. 13, pp. 4356-4362, 2008.

[77] N. Behabtu *et al.*, "Strong, light, multifunctional fibers of carbon nanotubes with ultrahigh conductivity," (in eng), *Science,* vol. 339, no. 6116, pp. 182-6, Jan 11 2013.

[78] N. T. Hung, N. M. Tuong, and E. G. Rakov, "Acid functionalization of carbon nanofibers," *Inorganic Materials*, vol. 46, no. 10, pp. 1077-1083, 2010.

[79] R. J. Kuriger, M. K. Alam, D. P. Anderson, and R. L. Jacobsen, "Processing and characterization of aligned vapor grown carbon fiber reinforced polypropylene," *Composites Part A: Applied Science and Manufacturing*, vol. 33, no. 1, pp. 53-62, 2002.

[80] M. H. Al-Saleh, W. H. Saadeh, and U. Sundararaj, "EMI shielding effectiveness of carbon based nanostructured polymeric materials: A comparative study," (in English), *Carbon,* vol. 60, pp. 146-156, Aug 2013.

[81] G. Tibbetts, M. Lake, K. Strong, and B. Rice, "A review of the fabrication and properties of vapor-grown carbon nanofiber/polymer composites," *Composites Science and Technology*, vol. 67, no. 7-8, pp. 1709-1718, 2007.

[82] J. Gou, Y. Tang, F. Liang, Z. Zhao, D. Firsich, and J. Fielding, "Carbon nanofiber paper for lightning strike protection of composite materials," *Composites Part B: Engineering*, vol. 41, no. 2, pp. 192-198, 2010.

[83] A. K. Geim and K. S. Novoselov, "The rise of graphene," *Nat Mater,* vol. 6, no. 3, pp. 183-91, Mar 2007.

[84] K. S. Novoselov *et al.*, "Electric field effect in atomically thin carbon films," *Science,* vol. 306, no. 5696, pp. 666-9, Oct 22 2004.

[85] E. P. Randviir, D. A. C. Brownson, and C. E. Banks, "A decade of graphene research: production, applications and outlook," *Materials Today,* vol. 17, no. 9, pp. 426-432, 2014.

[86] O. C. Compton and S. T. Nguyen, "Graphene oxide, highly reduced graphene oxide, and graphene: versatile building blocks for carbon-based materials," *Small,* vol. 6, no. 6, pp. 711-23, Mar 22 2010.

[87] D. R. Dreyer, S. Park, C. W. Bielawski, and R. S. Ruoff, "The chemistry of graphene oxide," *Chem Soc Rev*, vol. 39, no. 1, pp. 228-40, Jan 2010.

[88] I. K. Moon, J. Lee, R. S. Ruoff, and H. Lee, "Reduced graphene oxide by chemical graphitization," *Nat Commun*, vol. 1, p. 73, Sep 21 2010.

[89] S. Pei and H.-M. Cheng, "The reduction of graphene oxide," *Carbon*, vol. 50, no. 9, pp. 3210-3228, 2012.

[90] S. Pei, J. Zhao, J. Du, W. Ren, and H.-M. Cheng, "Direct reduction of graphene oxide films into highly conductive and flexible graphene films by hydrohalic acids," *Carbon*, vol. 48, no. 15, pp. 4466-4474, 2010.

[91] W. Chen, L. Yan, and P. R. Bangal, "Preparation of graphene by the rapid and mild thermal reduction of graphene oxide induced by microwaves," *Carbon*, vol. 48, no. 4, pp. 1146-1152, 2010.

[92] W. Gao *et al.*, "Direct laser writing of micro-supercapacitors on hydrated graphite oxide films," *Nat Nanotechnol*, vol. 6, no. 8, pp. 496-500, Jul 31 2011.

[93] D. Voiry *et al.*, "High-quality graphene via microwave reduction of solution-exfoliated graphene oxide," *Science*, vol. 353, no. 6306, pp. 1413-1416, Sep 23 2016.

[94] D. A. Dikin *et al.*, "Preparation and characterization of graphene oxide paper," *Nature*, vol. 448, no. 7152, pp. 457-60, Jul 26 2007.

[95] S. J. An *et al.*, "Thin Film Fabrication and Simultaneous Anodic Reduction of Deposited Graphene Oxide Platelets by Electrophoretic Deposition," *The Journal of Physical Chemistry Letters*, vol. 1, no. 8, pp. 1259-1263, 2010.

[96] C. Zhao *et al.*, "Formation of uniform reduced graphene oxide films on modified PET substrates using drop-casting method," *Particuology*, vol. 17, pp. 66-73, 2014.

[97] P. Kumar, S. Yu, F. Shahzad, S. M. Hong, Y. H. Kim, and C. M. Koo, "Ultrahigh electrically and thermally conductive self-aligned graphene/polymer composites using large-area reduced graphene oxides," (in English), *Carbon*, vol. 101, pp. 120-128, May 2016.

[98] C. J. Capozzi and R. A. Gerhardt, "Novel Percolation Mechanism in PMMA Matrix Composites Containing Segregated ITO Nanowire Networks," *Advanced Functional Materials*, vol. 17, no. 14, pp. 2515-2521, 2007.

[99] D. Untereker, S. Lyu, J. Schley, G. Martinez, and L. Lohstreter, "Maximum conductivity of packed nanoparticles and their polymer composites," (in eng), *ACS Appl Mater Interfaces,* vol. 1, no. 1, pp. 97-101, Jan 2009.

[100] R. Castro and K. Benthem, *Sintering: Mechanisms of Convention Nanodensification and Field Assisted Processes*. 2013.

[101] K.-S. Moon *et al.*, "Thermal behavior of silver nanoparticles for low-temperature interconnect applications," *Journal of Electronic Materials,* vol. 34, no. 2, pp. 168-175, 2005.

[102] M. Allen, A. Alastalo, M. Suhonen, T. Mattila, J. Leppaniemi, and H. Seppa, "Contactless Electrical Sintering of Silver Nanoparticles on Flexible Substrates," *IEEE Transactions on Microwave Theory and Techniques,* vol. 59, no. 5, pp. 1419-1429, 2011.

[103] S. Magdassi, M. Grouchko, O. Berezin, and A. Kamyshny, "Triggering the sintering of silver nanoparticles at room temperature," (in eng), *ACS Nano,* Research Support, Non-U.S. Gov't vol. 4, no. 4, pp. 1943-8, Apr 27 2010.

[104] P. Buffat and J. P. Borel, "Size effect on the melting temperature of gold particles," *Physical Review A,* vol. 13, no. 6, pp. 2287-2298, 1976.

[105] G. Bai, "Low-Temperature Sintering of Nanoscale Silver Paste for Semiconductor Device Interconnection," Ph.D., Materials Science and Engineering, Virginia Tech, 2005.

[106] H.-S. Kim, S. R. Dhage, D.-E. Shim, and H. T. Hahn, "Intense pulsed light sintering of copper nanoink for printed electronics," *Applied Physics A,* vol. 97, no. 4, pp. 791-798, 2009.

[107] V. K. Kumikov and K. B. Khokonov, "On the measurement of surface free energy and surface tension of solid metals," *Journal of Applied Physics,* vol. 54, no. 3, pp. 1346-1350, 1983.

[108] J. Perelaer, M. Klokkenburg, C. E. Hendriks, and U. S. Schubert, "Microwave flash sintering of inkjet-printed silver tracks on polymer substrates," (in eng), *Adv Mater,* vol. 21, no. 47, pp. 4830-4, Dec 18 2009.

[109] K. I. Rybakov, V. E. Semenov, S. V. Egorov, A. G. Eremeev, I. V. Plotnikov, and Y. V. Bykov, "Microwave heating of conductive powder materials," *Journal of Applied Physics,* vol. 99, no. 2, p. 023506, 2006.

[110] J. Ryu, H.-S. Kim, and H. T. Hahn, "Reactive Sintering of Copper Nanoparticles Using Intense Pulsed Light for Printed Electronics," *Journal of Electronic Materials,* vol. 40, no. 1, pp. 42-50, 2010.

[111] E. C. Garnett *et al.*, "Self-limited plasmonic welding of silver nanowire junctions," *Nat Mater,* vol. 11, no. 3, pp. 241-9, Feb 5 2012.

[112] S. B. Walker and J. A. Lewis, "Reactive silver inks for patterning high-conductivity features at mild temperatures," (in eng), *J Am Chem Soc,* vol. 134, no. 3, pp. 1419-21, Jan 25 2012.

[113] D. K. Chakravarthi *et al.*, "Carbon Fiber-Bismaleimide Composites Filled with Nickel-Coated Single-Walled Carbon Nanotubes for Lightning-Strike Protection," *Advanced Functional Materials,* vol. 21, no. 13, pp. 2527-2533, 2011.

[114] H. Wu, X. Wu, M. Ge, G. Zhang, Y. Wang, and J. Jiang, "Properties investigation on isotropical conductive adhesives filled with silver coated carbon nanotubes," *Composites Science and Technology,* vol. 67, no. 6, pp. 1182-1186, 2007.

[115] P. Kumar, S. Yu, F. Shahzad, S. M. Hong, Y.-H. Kim, and C. M. Koo, "Ultrahigh electrically and thermally conductive self-aligned graphene/polymer composites using large-area reduced graphene oxides," *Carbon,* vol. 101, pp. 120-128, 2016.

[116] S. Maiti, S. Suin, N. K. Shrivastava, and B. B. Khatua, "A strategy to achieve high electromagnetic interference shielding and ultra low percolation in multiwall carbon nanotube–polycarbonate composites through selective localization of carbon nanotubes," *RSC Advances,* vol. 4, no. 16, p. 7979, 2014.

[117] N. Li *et al.*, "Electromagnetic interference (EMI) shielding of single-walled carbon nanotube epoxy composites," (in eng), *Nano Lett,* vol. 6, no. 6, pp. 1141-5, Jun 2006.

[118] L. Daoqiang, Q. K. Tong, and C. P. Wong, "Conductivity mechanisms of isotropic conductive adhesives (ICAs)," in *1999 International Symposium on Advanced Packaging Materials,* Georgia, 1999, pp. 2-10.

[119] I. D. Rosca and S. V. Hoa, "Electrically Conductive Adhesives for CFRP Composites Based on Nickel Nanostrands and Carbon Nanotubes," in *19th International Conference on Composite Materials (ICCM19)*, Montreal, 2013, vol. 1, pp. 3899-3906.

[120] J. K. W. Sandler, J. E. Kirk, I. A. Kinloch, M. S. P. Shaffer, and A. H. Windle, "Ultra-low electrical percolation threshold in carbon-nanotube-epoxy composites," *Polymer*, vol. 44, no. 19, pp. 5893-5899, 2003.

[121] G. A. Gelves, B. Lin, U. Sundararaj, and J. A. Haber, "Low electrical percolation threshold of silver and copper nanowires in polystyrene composites," (in English), *Advanced Functional Materials*, vol. 16, no. 18, pp. 2423-2430, Dec 4 2006.

[122] H.-H. Lee, K.-S. Chou, and Z.-W. Shih, "Effect of nano-sized silver particles on the resistivity of polymeric conductive adhesives," *International Journal of Adhesion and Adhesives*, vol. 25, no. 5, pp. 437-441, 2005.

[123] S.-S. Chee and J.-H. Lee, "Reduction synthesis of silver nanoparticles anchored on silver micro-flakes and electrical resistivity of isotropic conductive adhesives at percolation threshold," *Electronic Materials Letters*, vol. 8, no. 3, pp. 315-320, 2012.

[124] H. Wu, X. Wu, M. Ge, G. Zhang, Y. Wang, and J. Jiang, "Effect analysis of filler sizes on percolation threshold of isotropical conductive adhesives," *Composites Science and Technology*, vol. 67, no. 6, pp. 1116-1120, 2007.

[125] F. Gubbels *et al.*, "Selective Localization of Carbon Black in Immiscible Polymer Blends: A Useful Tool To Design Electrical Conductive Composites," *Macromolecules*, vol. 27, no. 7, pp. 1972-1974, 1994.

[126] M. Li, W. Zhang, C. S. Wang, and H. P. Wang, "In situ formation of 2D conductive porous material with ultra low percolation threshold," (in English), *Materials Letters*, vol. 82, pp. 109-111, Sep 1 2012.

[127] S. L. Smitha, K. M. Nissamudeen, D. Philip, and K. G. Gopchandran, "Studies on surface plasmon resonance and photoluminescence of silver nanoparticles," *Spectrochimica Acta Part A: Molecular and Biomolecular Spectroscopy*, vol. 71, no. 1, pp. 186-190, 2008.

[128] V. Cecen *et al.*, "Electrical, mechanical and adhesive properties of ethylene-vinylacetate copolymer (EVA) filled with wollastonite fibers coated by silver," *European Polymer Journal,* vol. 44, no. 11, pp. 3827-3834, 2008.

[129] S. Nam *et al.*, "Effects of silica particles on the electrical percolation threshold and thermomechanical properties of epoxy/silver nanocomposites," *Applied Physics Letters,* vol. 99, no. 4, p. 043104, 2011.

[130] Y. P. Mamunya, V. V. Davydenko, P. Pissis, and E. V. Lebedev, "Electrical and thermal conductivity of polymers filled with metal powders," *European Polymer Journal,* vol. 38, no. 9, pp. 1887-1897, 2002.

[131] L. Ge *et al.*, "Investigation of Gas Permeability in Carbon Nanotube (CNT)−Polymer Matrix Membranes via Modifying CNTs with Functional Groups/Metals and Controlling Modification Location," *The Journal of Physical Chemistry C,* vol. 115, no. 14, pp. 6661-6670, 2011.

[132] Y. Li and C. P. Wong, "Recent advances of conductive adhesives as a lead-free alternative in electronic packaging: Materials, processing, reliability and applications," *Materials Science and Engineering: R: Reports,* vol. 51, no. 1-3, pp. 1-35, 2006.

[133] W. S. Bao, S. A. Meguid, Z. H. Zhu, and G. J. Weng, "Tunneling resistance and its effect on the electrical conductivity of carbon nanotube nanocomposites," (in English), *Journal of Applied Physics,* vol. 111, no. 9, pp. 093726-7, May 1 2012.

[134] T. A. Shastry *et al.*, "Large-area, electronically monodisperse, aligned single-walled carbon nanotube thin films fabricated by evaporation-driven self-assembly," (in eng), *Small,* vol. 9, no. 1, pp. 45-51, Jan 14 2013.

[135] A. Buldum and J. P. Lu, "Contact resistance between carbon nanotubes," (in English), *Physical Review B,* vol. 63, no. 16, Apr 15 2001.

[136] A. Hu *et al.*, "Low temperature sintering of Ag nanoparticles for flexible electronics packaging," *Applied Physics Letters,* vol. 97, no. 15, p. 153117, 2010.

[137] E. C. Garnett *et al.*, "Self-limited plasmonic welding of silver nanowire junctions," (in eng), *Nature Materials,* Research Support, Non-U.S. Gov't vol. 11, no. 3, pp. 241-9, Mar 2012.

[138] H. P. Wu *et al.*, "High conductivity of isotropic conductive adhesives filled with silver nanowires," *International Journal of Adhesion and Adhesives,* vol. 26, no. 8, pp. 617-621, 2006.

[139] X. Tang, M. Tsuji, P. Jiang, M. Nishio, S.-M. Jang, and S.-H. Yoon, "Rapid and high-yield synthesis of silver nanowires using air-assisted polyol method with chloride ions," *Colloids and Surfaces A: Physicochemical and Engineering Aspects,* vol. 338, no. 1-3, pp. 33-39, 2009.

[140] B. Li, S. Ye, I. E. Stewart, S. Alvarez, and B. J. Wiley, "Synthesis and Purification of Silver Nanowires To Make Conducting Films with a Transmittance of 99%," *Nano Lett,* vol. 15, no. 10, pp. 6722-6, Oct 14 2015.

[141] P. Zhang *et al.*, "Silver nanowires: Synthesis technologies, growth mechanism and multifunctional applications," *Materials Science and Engineering B,* vol. 223, pp. 1-23, 2017.

[142] F. L. O. Wadsworth, "Notes on Silvering Solutions and Silvering," *The Astrophysical Journal,* vol. 1, pp. 252-260, 1895.

[143] H. D. Curtis, "Methods of Silvering Mirrors," *Publications of the Astronomical Society of the Pacific,* vol. 23, pp. 13-32, 1911.

[144] R. Malureanu, M. Zalkovskij, A. Andryieuski, and A. V. Lavrinenko, "Controlled Ag Electroless Deposition in Bulk Structures with Complex Three-Dimensional Profiles," *Journal of The Electrochemical Society,* vol. 157, no. 12, p. K284, 2010.

[145] F. Formanek, N. Takeyasu, T. Tanaka, K. Chiyoda, A. Ishikawa, and S. Kawata, "Selective electroless plating to fabricate complex three-dimensional metallic micro/nanostructures," *Applied Physics Letters,* vol. 88, no. 8, p. 083110, 2006.

[146] J. Boehm, A. François, H. Ebendorff-Heidepriem, and T. M. Monro, "Chemical Deposition of Silver for the Fabrication of Surface Plasmon Microstructured Optical Fibre Sensors," *Plasmonics,* vol. 6, no. 1, pp. 133-136, 2010.

[147] M. L. Cheng, B. C. Tsai, and J. Yang, "Silver nanoparticle-treated filter paper as a highly sensitive surface-enhanced Raman scattering (SERS) substrate for detection of tyrosine in

aqueous solution," (in eng), *Anal Chim Acta,* Research Support, Non-U.S. Gov't vol. 708, no. 1-2, pp. 89-96, Dec 5 2011.

[148] H. K. Park, H. B. Lee, and K. Kim, "A facile deposition of silver onto the inner surface of a glass capillary tube for micro-surface-enhanced Raman scattering measurements," (in eng), *Appl Spectrosc,* vol. 61, no. 1, pp. 19-24, Jan 2007.

[149] L. Tongxiang, G. Wenli, Y. Yinghui, and T. Chunhe, "Electroless plating of silver on graphite powders and the study of its conductive adhesive," *International Journal of Adhesion and Adhesives,* vol. 28, no. 1-2, pp. 55-58, 2008.

[150] T. C. Chueh, C. H. Hu, and S. C. Yen, "Electrically Conductive Adhesives with Low Ag Content Prepared by Ag Self-Activated Plating and PEDOT:PSS," (in English), *Journal of The Electrochemical Society,* vol. 162, no. 1, pp. D56-D61, 2015.

[151] J.-w. Zheng *et al.*, "Fabrication of Ag–C composite materials with core–shell structure," *Applied Surface Science,* vol. 313, pp. 346-351, 2014.

[152] S. Shukla, S. Seal, Z. Rahaman, and K. Scammon, "Electroless copper coating of cenospheres using silver nitrate activator," *Materials Letters,* vol. 57, no. 1, pp. 151-156, 2002.

[153] Y. Lin *et al.*, "Rapid, solventless, bulk preparation of metal nanoparticle-decorated carbon nanotubes," (in eng), *ACS Nano,* vol. 3, no. 4, pp. 871-84, Apr 28 2009.

[154] F. Wang, S. Arai, and M. Endo, "Metallization of multi-walled carbon nanotubes with copper by an electroless deposition process," *Electrochemistry Communications,* vol. 6, no. 10, pp. 1042-1044, 2004.

[155] Y. Wang, X. Xu, Z. Tian, Y. Zong, H. Cheng, and C. Lin, "Selective heterogeneous nucleation and growth of size-controlled metal nanoparticles on carbon nanotubes in solution," (in eng), *Chemistry,* Research Support, Non-U.S. Gov't vol. 12, no. 9, pp. 2542-9, Mar 8 2006.

[156] L. M. Ang, T. S. A. Hor, G. Q. Xu, C. H. Tung, S. P. Zhao, and J. L. S. Wang, "Decoration of activated carbon nanotubes with copper and nickel," (in English), *Carbon,* vol. 38, no. 3, pp. 363-372, 2000.

[157] J. M. Córdoba and M. Odén, "Growth and characterization of electroless deposited Cu films on carbon nanofibers," *Surface and Coatings Technology*, vol. 203, no. 22, pp. 3459-3464, 2009.

[158] J. F. Silvain, P. Richard, J. Douin, M. Lahaye, and J. M. Heintz, "Electroless Coating Process of Carbon Nano Fibers by Copper Metal," *Materials Science Forum*, vol. 534-536, pp. 1445-1448, 2007.

[159] J. Tamayo-Ariztondo, J. M. Córdoba, M. Odén, J. M. Molina-Aldareguia, and M. R. Elizalde, "Effect of heat treatment of carbon nanofibres on electroless copper deposition," *Composites Science and Technology*, vol. 70, no. 16, pp. 2269-2275, 2010.

[160] S. Arai, Y. Imoto, Y. Suzuki, and M. Endo, "Fabrication of Ni–B alloy coated vapor-grown carbon nanofibers by electroless deposition," *Carbon*, vol. 49, no. 4, pp. 1484-1490, 2011.

[161] S. Arai, M. Kobayashi, T. Yamamoto, and M. Endo, "Pure-Nickel-Coated Multiwalled Carbon Nanotubes Prepared by Electroless Deposition," *Electrochemical and Solid-State Letters*, vol. 13, no. 12, p. D94, 2010.

[162] S. Arai and J. Fujii, "Electroless Deposition of Silver on Multiwalled Carbon Nanotubes Using Iodide Bath," *Journal of The Electrochemical Society*, vol. 158, no. 8, p. D506, 2011.

[163] T. G. Ros, A. J. van Dillen, J. W. Geus, and D. C. Koningsberger, "Surface Oxidation of Carbon Nanofibres," *Chemistry - A European Journal*, vol. 8, no. 5, p. 1151, 2002.

[164] J. Przyłuski, M. Kasprzak, and J. Bieliński, "Investigations of SnCl2-sensitizing solutions for electroless plating," *Surface and Coatings Technology*, vol. 31, no. 3, pp. 203-211, 1987.

[165] X. Wei and D. K. Roper, "Tin Sensitization for Electroless Plating Review," *Journal of the Electrochemical Society*, vol. 161, no. 5, pp. D235-D242, 2014.

[166] F. T. Tharwat, *Dispersion of Powders in Liquids and Stabilization of Suspensions*. Hoboken, NJ, USA: Wiley-VCH, 2012.

[167] J. F. D'Amico, M. A. De Angelo, J. F. Henrickson, J. T. Kenney, and D. J. Sharp, "Selective Electroless Metal Deposition Using Patterned Photo-Oxidation of Sn(II) Sensitized Substrates," *Journal of The Electrochemical Society*, vol. 118, no. 10, p. 1695, 1971.

[168] R. L. Cohen and K. W. West, "Solution Chemistry and Colloid Formation in the Tin Chloride Sensitizing Process," *Journal of The Electrochemical Society*, vol. 119, no. 4, pp. 433-438, 1972.

[169] R. L. Cohen, J. F. D'Amico, and K. W. West, "Mössbauer Study of Tin(II) Sensitizer Deposits on Kapton," *Journal of The Electrochemical Society*, vol. 118, no. 12, p. 2042, 1971.

[170] N. Feldstein, J. A. Weiner, and G. L. Schnable, "Some Aspects of the Chemistry of Tin Sensitizing Solutions," *Journal of The Electrochemical Society*, vol. 119, no. 11, p. 1486, 1972.

[171] M. Batzill and U. Diebold, "The surface and materials science of tin oxide," *Progress in Surface Science*, vol. 79, no. 2-4, pp. 47-154, 2005.

[172] D. Su, H. J. Ahn, and G. Wang, "SnO2@graphene nanocomposites as anode materials for Na-ion batteries with superior electrochemical performance," *Chem Commun (Camb)*, vol. 49, no. 30, pp. 3131-3, Apr 18 2013.

[173] E. S. King, "Silvering Mirrors, with Plate IX," *Popular Astronomy*, pp. 93-95, 1922.

[174] H. D. Curtis, "METHODS OF SILVERING MIRRORS," *Publications of the Astronomical Society of the Pacific*, vol. 23, no. 135, pp. 13-32, 1911.

[175] A. Antonello *et al.*, "Optimized Electroless Silver Coating for Optical and Plasmonic Applications," *Plasmonics*, vol. 7, no. 4, pp. 633-639, 2012.

[176] Y. Feng and H. Yuan, "Electroless plating of carbon nanotubes with silver," *Journal of Materials Science*, vol. 39, no. 9, pp. 3241-3243, 2004.

[177] M. Schlesinger and M. Paunovic, Modern Electroplating, c. Wiley, ed., Hoboken, NJ, 2010. [Online]. Available.

[178] X. X. Luo, G. A. Gelves, U. Sundararaj, and J. L. Luo, "Silver-coated copper nanowires with improved anti-oxidation property as conductive fillers in low-density polyethylene," (in English), *Canadian Journal of Chemical Engineering*, vol. 91, no. 4, pp. 630-637, Apr 2013.

[179] R. Verdejo, M. M. Bernal, L. J. Romasanta, and M. A. Lopez-Manchado, "Graphene filled polymer nanocomposites," *J. Mater. Chem.,* vol. 21, no. 10, pp. 3301-3310, 2011.

[180] R. Ramasubramaniam, J. Chen, and H. Liu, "Homogeneous carbon nanotube/polymer composites for electrical applications," *Applied Physics Letters,* vol. 83, no. 14, pp. 2928-2930, 2003.

[181] A. Bachtold *et al.*, "Scanned Probe Microscopy of Electronic Transport in Carbon Nanotubes," *Physical Review Letters,* vol. 84, no. 26, pp. 6082-6085, 2000.

[182] J. R. Potts, D. R. Dreyer, C. W. Bielawski, and R. S. Ruoff, "Graphene-based polymer nanocomposites," *Polymer,* vol. 52, no. 1, pp. 5-25, 2011.

[183] Y. Saito, J. J. Wang, D. A. Smith, and D. N. Batchelder, "A Simple Chemical Method for the Preparation of Silver Surfaces for Efficient SERS," *Langmuir,* vol. 18, no. 8, pp. 2959-2961, 2002.

[184] N. Feldstein, S. L. Chow, and M. Schlesinger, "Electron Microscope Studies of art Improved Sensitizer Solution," *Journal of The Electrochemical Society,* vol. 120, no. 7, p. 875, 1973.

[185] N. Cianos and E. T. Pierce, "A Ground-Lightning Environment for Engineering Usage," Stanford Reasearch Institute, Menlo Park, Ca,1972.

[186] D. Mann, A. Javey, J. Kong, Q. Wang, and H. Dai, "Ballistic Transport in Metallic Nanotubes with Reliable Pd Ohmic Contacts," *Nano Letters,* vol. 3, no. 11, pp. 1541-1544, 2003.

[187] Y. Li, K.-s. Moon, and C. P. Wong, *Nano-bio- Electronic, photonic and MEMS packaging*. 2010, pp. 19-45.

[188] S. M. Marcus and R. L. Blaine, "Thermal conductivity of polymers, glasses and ceramics by modulated DSC," *Thermochimica Acta,* vol. 243, no. 2, pp. 231-239, 1994.

[189] M. B. Heaney, "Measurement and interpretation of nonuniversal critical exponents in disordered conductor–insulator composites," *Physical Review B,* vol. 52, no. 17, pp. 12477-12480, 1995.

[190] S.-I. Lee, Y. Song, T. W. Noh, X.-D. Chen, and J. R. Gaines, "Experimental observation of nonuniversal behavior of the conductivity exponent for three-dimensional continuum percolation systems," *Physical Review B,* vol. 34, no. 10, pp. 6719-6724, 1986.

[191] W. Z. Shao, N. Xie, L. Zhen, and L. C. Feng, "Conductivity critical exponents lower than the universal value in continuum percolation systems," *Journal of Physics: Condensed Matter,* vol. 20, no. 39, 2008.

APPENDIX A LOOKUP TABLE FOR COMMERCIAL LSP SYSTEMS

Table A.1: Summary of available LSP systems

manufacturer	Mesh areal weight (g/m^2)	Resin areal weight (g/m^2)	Cumulative areal weight (g/m^2)	Conductive material	Theoretical sheet resistivity[1]. Ohms per square ($\Omega/\square$)	Specific conductivity[2] ($S \cdot cm^2/g$)	Mesh weight percentage
APCM [27]	73	171	244	Cu	2.08×10^{-3}	1.97×10^{4}	30
	142	220	361	Cu	1.08×10^{-3}	2.57×10^{4}	39
	195	220	415	Cu	7.61×10^{-4}	3.09×10^{4}	47
	78	171	249	Al	9.3×10^{-4}	4.3×10^{4}	31
	137	171	307	Al	5.3×10^{-4}	6.1×10^{4}	44
Henkel Corporation [24]	73	97	170	Cu	2.09×10^{-3}	2.82×10^{4}	43
	107	97	204	Cu	1.42×10^{-3}	3.44×10^{4}	52
	142	97	238	Cu	1.08×10^{-3}	3.89×10^{4}	59
	195	97	292	Cu	7.8×10^{-3}	4.38×10^{4}	67
	195	146	341	Cu	7.8×10^{-3}	3.75×10^{4}	57

[1] The calculation of the theoretical sheet resistivity assumes a perfectly isotropic conductivity equivalent to that of a foil of the same areal weight

[2] Specific conductivity refers to the sheet conductivity divided by areal mass, or volume conductivity divided by density.

APPENDIX B ADDITIONAL ABSERVATIONS

Critical exponent in heterogeneous epoxy-silver composites by phase selective in-situ synthesis:

It was shown in section 4.3.3 that the resistivity of the composites obeyed a percolation law with a very low percolation threshold and an unusually high critical exponent of τ=2.47. It is indeed known that in percolation theory, 3-dimensional conduction systems should exhibit a critical exponent in the vicinity of 1.9.

The universality of this value was however questioned by many authors and was measured by some to exceed the theoretical value [189, 190] or to fall behind the value [191]. Lee *et al*. sought to verify the "swiss cheese continuum model" where random spherical regions of insulating media are distributed in a uniform conductive media [190]. They fabricated a composite consisting of silver coated spheres distributed in a teflon matrix and another where nonconductive glass beads were pressed with indium powder. They obtained in the former a critical exponent of 3.1 in the former case, while the latter yielded a 2.0 value, in agreement with theory. The explanation for the increased exponent comes from the existence of narrow, nearly 1 dimensional conducting paths that connect large "blobs" of conducting media.

The similarity with our work is striking. In the idealized model, the epoxy suspension forms spheres of nonconducting media that are embedded into the silver precipitated from the aqueous ink. The same argument therefore holds here as well. In conclusion, although unusual, the deviation from the theoretical critical exponent observed in our work is not without precedent and was previously observed on a very similar system.

Early experiments with electroless deposition:

The initial experiments with electroless deposition on carbon nanofibers were thought in a way to simplify the process to its essential components so as to limit the possible interactions between chemical species. Accordingly, formaldehyde was chosen as the reducing agent since it is the simplest form of aldehyde.

In these experiments, the reaction proceeded very quickly: in a matter of seconds, a silver film would appear, and the glass vessel would become opaque. We never however noticed a significant change in the color of the solution. Figure B.1 shows a micrography of one of these early samples.

It depicts a mixture of very large and very small silver aggregates in a seemingly chaotic organization in the material. Such a distribution of the metal particles is indicative of a rapid, uncontrolled synthesis of the particles where the nucleation dynamics are dominated by the growth dynamics. After a few experiments, it became evident that a systematic, broad-sweeping experiment was needed to identify starting parameters.

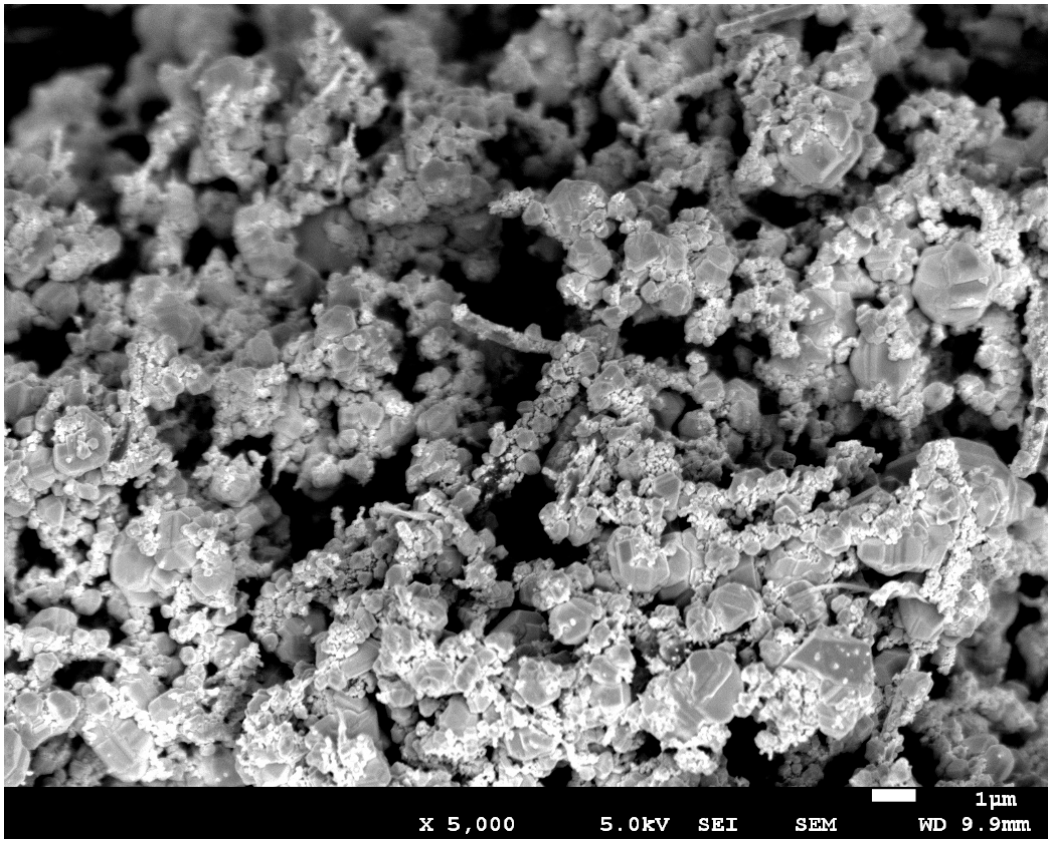

Figure B.1: Early electroless deposition experiment with formaldehyde as a reducing agent

The parameters to vary were identified from the literature and put into a Taguchi matrix. The matrix is shown in Table B.1**.**. From this experiment, it became clear that dextrose yielded a much smoother coating than formaldehyde. The other conclusions that could be made were that the presence of ethanol was beneficial and that the first component to touch the nanofibers should be the reducing agent.

Table B.1: Taguchi matrix for initial experiments

sample number		1	2	3	4	5	6	7	8
sensitization time	0: 1 hour 1: 10 min	0	0	0	0	1	1	1	1
sensitization method	0: sonication 1: magnetic stirrer	0	0	1	1	0	0	1	1
reducing agent	0: formaldehyde 1: dextrose	0	0	1	1	1	1	0	0
KOH/Ag ratio	0: 1/500 1: 1/100	0	1	0	1	0	1	0	1
first plating component	0: reducer 1:Tollen's	0	1	0	1	1	0	1	0
presence of ethanol	0: none 1: v tollens/4	0	1	1	0	0	1	1	0

Figure B.2 shows an SEM image of sample #3 from the matrix. The improvement in the coating was clear at this point, and it was thereon reasonable to think that a continuous coating could be achieved. Subsequent experiments did however show very poor reproducibility. Many experiments were then performed with no clear trend in performance. This lack of reproducibility explains the fact that these manipulations were omitted in the publications.

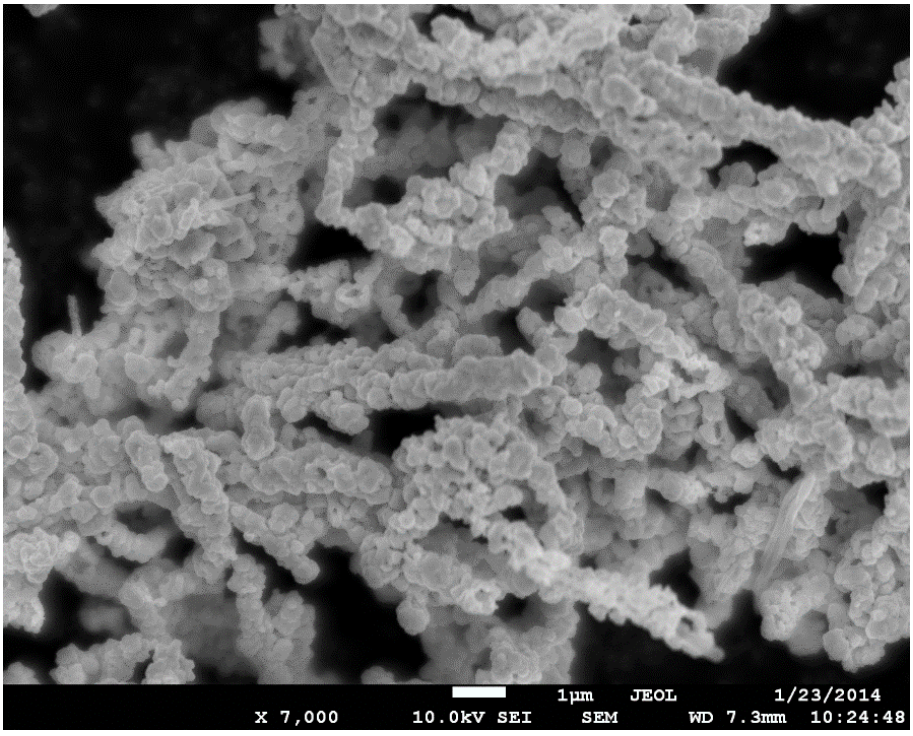

Figure B.2: Sample 3 from the Taguchi matrix

It was not until we decided to test the deionized water from the lab for Cl^- ions that the reason for the lack of reproducibility became clear. We knew from the sensitizing experiments that if the rinsing was not properly performed, the silver deposition would fail. When a silver nitrate test confirmed the presence of Cl^- ions in the water, we knew we had to switch to ultra-pure water if we were to obtain a reproducible process. From this point, the optimisation work could be resumed with good reproducibility.